Distribution Agreement

Signature:

Marika Wieliczko

Date

Innocent and Non-innocent Countercation Interactions in Transition Metal Oxidation Catalysts

By

Marika Wieliczko
Doctor of Philosophy

Chemistry

Craig L. Hill, Ph.D.
Advisor

R. Brian Dyer, Ph.D.
Committee Member

Cora E. MacBeth
Committee Member

Accepted:

Lisa A. Tedesco, Ph.D.
Dean of the James T. Laney School of Graduate Studies

Date

Innocent and Non-innocent Countercation Interactions in Transition Metal Oxidation Catalysts

By

Marika Wieliczko
B.S., Eastern Kentucky University, 2011

Advisor: Craig L. Hill, Ph.D.

An abstract of
A dissertation submitted to the Faculty of the
James T. Laney School of Graduate Studies of Emory University
in partial fulfillment of the requirements for the degree of
Doctor of Philosophy in Chemistry
2017

Abstract

Innocent and Non-innocent Countercation Interactions in Transition Metal Oxidation Catalysts

By

Marika Wieliczko

Oxidation catalysis is ubiquitous in chemical transformations that are critical in modern society, and many industrially-relevant oxidation processes have analogues in biological systems. The effect of redox-inactive ions is essential in various biological processes and though some corollary to artificial systems is known, the effects of non-innocent cation interactions on transition metal oxidation catalysts remain poorly understood. Chapter 1 introduces the reader to the broad field of transition metal-catalyzed oxidation using specific examples of organic substrate oxidation, as in the monooxygenation of aromatic hydrocarbons, and inorganic substrate oxidation as in the conversion of water to dioxygen. These reactions illustrate the complementary ways in which oxidative catalysis is used to both extract energy in a downhill process, as well as capture and store energy in an energetically-uphill process. These reactions, which are catalyzed by transition-metal centers, are the basis for the investigations which follow. Chapter 2 illustrates the influence of redox-inert Ca^{2+} ions on the oxidation state of a cobalt-centered coordination complex and explores its potential application in aromatic hydrocarbon oxidation. In Chapter 3, the specific binding modes of K^+ cations to the active site of a tetraruthenium polyoxometalate water oxidation catalyst are demonstrated to significantly impact both redox and acid-base properties, which are critical aspects of the proton and electron transfer steps in the multi-step mechanism of dioxygen formation and evolution. In Chapter 4, the conversion of cobalt-based polyoxometalate water oxidation catalysts to hydrophobic forms using weakly interacting tetraalkylammonium cations facilitates detailed studies of these catalysts in non-aqueous media, where electrochemical, spectroscopic, stability and reactivity studies are conducted that are uninformative or not possible in bulk water. These studies yield unprecedented insights into the nature of transition metal oxidation catalysts whose reactivity and stability can be controlled by understanding the effects of both innocent and non-innocent cation interactions.

Innocent and Non-innocent Countercation Interactions in Transition Metal Oxidation Catalysts

By

Marika Wieliczko
B.S., Eastern Kentucky University, 2011

Advisor: Craig L. Hill, Ph.D.

A dissertation submitted to the Faculty of the
James T. Laney School of Graduate Studies of Emory University
in partial fulfillment of the requirements for the degree of
Doctor of Philosophy in Chemistry
2017

Acknowledgements

As this long journey comes to a close for me, I am painfully aware that the path to a Ph.D. is one that no individual can accomplish alone. I wish to express my sincerest gratitude to those individuals who have made it possible for me to achieve my greatest dreams thus far. First, I want to thank my parents for making difficult decisions - the right decisions - so that I could have the best possible opportunities to pursue a world-class education. My undergraduate mentors and advisors, Dr. Nathan Tice and Dr. Darrin Smith, were instrumental in giving me the support and encouragement to continue my passion for science in graduate school and deserve accolades for doing this not only for me but for so many other young people. I want to thank my committee, without whom I would not have been able to accomplish my goals. Dr. Cora MacBeth has been an inspirational figure for me since the first time I heard her speak; I was so impressed with her work and her passion for it then, and over the years my appreciation and respect for her has grown and I can only hope to be so tenacious, astute, and objective in my own endeavors. She has been a mentor, a teacher, a role model, and has come through in some of my most difficult moments. I am so grateful for the compassion and humility that Dr. Brian Dyer has always shown, which has bolstered my own self-confidence. I feel lucky that I was able to learn so much from his lectures and to have had his guidance in my research. My advisor, Dr. Craig Hill has been there for me since the beginning, although he may not know that. Ever since I first met Craig, he sparked something in me that motivated me to continue pursuing this path even when it seemed hopeless. He has

been a presence in my life in so many ways and has positively influenced me in so many ways that I cannot begin to describe. Most of all, it is his refusal to give up on me or anyone or anything for which I am infinitely grateful. I express my deepest gratitude to Dr. Chris Scarborough, who started me on the long path and taught me to be fearless, to take on challenges head-first, and to stand up for myself. I will forever appreciate the time I spent in his lab and the experience I gained from it. Dr. John Bacsa has been a mentor and friend and allowed me to pursue my interest in crystallography, which has been one of the most enriching aspects of my time at Emory. Dr. George Painter has played a key role in my professional development and I feel privileged to have had the chance to learn from him and his breadth of experience. The guidance of Dr. Yurii Gueletii has been essential for my progress in the lab and beyond. I wish to express my deepest thanks to my labmates and colleagues and especially those have gone above and beyond. Lastly, as so many of the prior fall into this category as well, I wish to thank all of my friends as these are the people I treasure most above all.

Table of Contents

Chapter 1 1

1.1 Introduction to Oxidation Catalysis 2

    1.1.1 Overview of Oxidation Catalysts 2

    1.1.2 Transition Metal-Oxo Complexes and Selectivity in Oxidation Catalysis 3

1.2 Transition Metal Catalysts for Hydrocarbon Oxidation 6

    1.2.1 Enzymatic Fe-catalyzed Hydrocarbon Oxidation by Cytochrome P450 6

    1.2.2 The Hock Process for Aromatic Hydrocarbon Oxidation in Chemical Industry 7

1.3 Transition Metal Catalysts for Water Oxidation 1

    1.3.1 Mn-catalyzed Water Oxidation in Photosynthesis 1

    1.3.2 Co and Ru Molecular Catalysts for Artificial Water Splitting 3

1.4 Non-innocent Ligands, Anions, and Cations in Oxidation Catalysis 6

1.5 Hypothesis and Scope of this Work 9

1.6 References 12

Chapter 2 20

2.1 Introduction: Activation of Transition Metal Complexes by Redox-inactive Cations 21

    2.1.1 Selective Monooxygenation of Aromatic Hydrocarbons 21

    2.1.2 Ligand Design for Accessing Mid- and Late-metal Oxo Species 25

2.2 Experimental 28

    2.2.1 General Considerations 28

    2.2.2 Ligand and Co(II) Complex Synthesis 29

    2.2.3 Catalytic Oxygenation of Benzene 32

    2.2.4 EPR and Magnetic Circular Dichroism Spectroscopy 34

    2.2.5 Resonance Raman Spectroscopy 35

    2.2.6 X-ray Crystallography 36

2.3 Results and Discussion 36

    2.3.1 Synthesis of Co(II) Complexes 36

    2.3.2 Reactivity of Complexes towards Oxygen Atom Transfer Agents 37

    2.3.3 Characterization of **1-O** 42
    2.3.4 Preliminary Reactivity Studies for Catalytic Monooxygenation of Benzene 49
2.4 Conclusions 53
2.6 References 54
Chapter 3 59
3.1 Introduction to Cations in Water Oxidation 60
    3.1.1 Redox-inactive Cations in Photosynthesis and OEC Models 60
    3.1.2 Transition Metal-substituted Polyoxometalate WOCs 61
    3.1.3 Specific and Non-specific Cation Effects in POMs 63
3.2 Experimental 65
    3.2.1 General Considerations 65
    3.2.2 X-ray crystallography 66
    3.2.3 Electrochemical and Electrocatalytic Behavior 66
    3.2.4 Titrations 67
    3.2.5 Stopped flow kinetics measurements 67
3.3 Results and Discussion 67
    3.3.1 Specific Binding of K^+ in the X-ray crystal structures of **Ru_4POM** 67
    3.3.2 Cation-specific Deviations in Acid-base Properties 72
    3.3.3 Effects of Cations on Kinetics of Oxidation 76
3.4 Conclusions 78
3.5 References 81
Chapter 4 85
4.1 Introduction to Cobalt-catalyzed Water Oxidation 86
    4.1.1 Heterogeneous Cobalt Catalysts for Water Oxidation 86
    4.1.2 Homogeneous Cobalt Catalysts for Water Oxidation 87
    4.1.3 Stability of Homogeneous Catalysts in Aqueous Media 90
4.2 Experimental 92
    4.2.1 General considerations 92
    4.2.2 Synthesis of POMs 93
    4.2.3 Conversion to hydrophobic salts 94
    4.2.4 X-ray crystallography 97

4.2.5 Electrochemistry 99

4.2.6 SEM-EDX Measurements 99

4.3 Results and Discussion 100

4.3.1 Synthesis of Co_4POMs and Conversion to Hydrophobic Forms 100

4.3.2 Solid and Solution State Structures of Co_4POMs 107

4.3.3 Chemical and Electrochemical Oxidations of **$Co_4P_2W_{18}$** in MeCN 113

4.3.4 Dioxygen formation inhibition and pKa modulation in **$Co_4P_2W_{18}$** by MeCN 121

4.3.5 Stability and Reactivity of **$Co_4V_2W_{18}$** in Solution 125

4.3.6 Electrochemical Stability of Co_4POMs in Anhydrous Media 131

4.4 Conclusions 137

4.5 References 139

Table of Figures

Figure 1.1 Radical coupling side reaction and overoxidation examples in the monooxygenation of benzene. 5
Figure 1.2 The NIH shift mechanism of arene monooxygenation in cytochrome P450 6
Figure 1.3 Industrial Hock process for production of phenol from benzene. 8
Figure 1.4 Schematic illustration of the oxygen evolving complex, or OEC, in photosynthesis 2
Figure 1.5 Schematic illustration of transitions from S_o through S_4 in the Kok cycle of the OEC in photosynthesis. 3
Figure 1.6 General structure of Ru_4POM (left) and Co_4POM (right) polyoxometalates (POMs) that are under investigation as homogeneous water oxidation catalysts (WOCs). 6
Figure 2.1 Qualitative MO diagrams depicting the effect of increasing group number on oxo character and electrophilicity 23
Figure 2.2 Qualitative MO diagrams depicting the ordering of MOs for weak and strong donor ligands in TBP geometry. 24
Figure 2.3 Reaction of the Borovik Co(II) system with PhIO in DCM to yield a Co(III) hydroxide.[49] 26
Table 2.1 Calibration curve generation for phenol with $C_{14}H_{30}$ ISTD 33
Figure 2.4 Schematic drawings of complex 1 and 2 and the X-ray crystal structure of 1. Hydrogen atoms are omitted for clarity. Thermal ellipsoids are shown at the 50% probability level. Carbon atoms shown in grey, nitrogen in blue, oxygen in red and sulfur in yellow. 37
Figure 2.5 Comparison of UV-Vis spectra of complex 1 and 2 and the products of reaction with PhIO in benzonitrile. The product from complex 2 matches the spectrum of Co^{III}-aqua complex.[49] 39
Figure 2.6 Reaction of ~0.5 mM 1 (purple) with 2 equivalents PhIO to form 1-O in benzonitrile. The inset shows a comparison of 1-O formed from TBHP (blue) and PhIO (pink). 40
Figure 2.7 Linear fit of the decay of absorbance bands associated with decomposition of 1-O formed from reaction of 1 with PhIO. 40
Figure 2.8 Comparison of half-life of 1-O formed from PhIO in various solvents. The longest $T_{1/2}$ observed for THF was ~10 days. 41
Table 2.2 Half-life of 1-O generated from urea-H_2O_2 in various solvents and C-H bond dissociation energies. 43
Figure 2.9 Comparison of the IR spectra of 1 (purple) and 1-O (green). Full spectrum (top) with inset showing O-H band that appears over extended periods and zoom of the fingerprint region (bottom). 44
Figure 2.10 Reaction of 1 equivalent of 1-O generated from PhIO with DHA yields 1 equivalent of anthracene per Co(II) and regenerates 1. 45
Figure 2.11EPR spectrum and simulation of frozen THF solution (4 K) of 1, left; Simulation 65% gx=gy= 4.45, gz= 2.02 (Az = 9.7 x 10-3Hz) and 35% gx= 4.95, gy= 3.95, gz= 2.02 (Az = 9.5 x 10-

3 Hz), (1-O, right) EPR spectrum of 2 after reaction with excess H2O2 in THF, Simulation 100% gx=gy= 4.45, gz= 2.03 (Az = 9.5 x 10-3Hz) 47
Figure 2.12 Resonance Raman spectra of 1-O generated from TBHP at 514 nm and 633 nm excitation. 48
Figure 2.13 UV-Vis spectrum of 1 + $^tBuO_2H$ in THF to form 1-O (light blue) with exposure to 455 nm LED (900 mA) over 5 h (medium and dark blue lines) and final product after 48 h (purple).. 49
Figure 2.14 Phenol detected by GC from catalytic monooxygenation of benzene with H_2O_2. 51
Figure 2.15 Overoxidation of phenol from $CoCl_2$ detected by GC. Reaction conditions: 0.006μmol catalyst (Co atom), 80°C, 10mL benzene, 1mmol H_2O_2. Catalyst 1 after 24 h (top, blue) and $CoCl_2$ after 4 hours (bottom, red). 51
Figure 2.16 Crystal structure of 1-urea adduct isolated from urea-H_2O_2 solutions of 1 in attempts to isolate 1-O. 52
Figure 3.1 X-ray crystal of $Ru_4POM@K_2$ .The additional K^+ counterions are omitted for clarity and are disordered over interactions with the tungstate ligands. Thermal ellipsoids are shown at the 50% probability level. 69
Figure 3.2 Schematic of the 2-electron and 2-proton change that results in the same net charge upon reduction of Ru_4POM in aqueous EtOH. 69
Figure 3.3 X-ray crystal structure of $Ru_4POM@K_3$. Seven additional K^+ counterions are omitted for clarity. Thermal ellipsoids are shown at the 50% probability level. 70
Figure 3.4 Schematic drawing similarities in the coordination of K^+ ions in Ru_4POM (right) and Ca^{2+} ion in the OEC (left). 71
Figure 3.5 Dimerization of two Ru_4POM in the crystal structure of $Ru_4POM(2^-)$. 72
Figure 3.6 Change in pH of 1 mM solutions of Ru_4POM during titration with 10 mM NaOH with no added electrolyte (blue), 0.5M LiCl (orange), 0.5M NaCl (green) and 0.5M KCl (purple). 73
Figure 3.7 Binding of K^+ and hydronium (H_3O^+) by 18-crown-6 ether chelator. 74
Figure 3.8 Changes in the UV-Vis spectrum of 0.02 mM Ru_4POM in the presence of alkali cations. 75
Figure 3.9 Protonation state changes associated with electronic absorbance spectral features where (a) at low pH all terminal aqua ligands are protonated and (b) increased pH or cation binding leads to proton transfer and loss of the associated 455 nm absorbance band. 75
Figure 3.10 Kinetics of $[Ru(bpy)_3]^{3+}$ consumption in the presence of electrolytes. Conditions: 5μM Ru_4POM, 1mM $[Ru(bpy)_3]^{3+}$, 40 mM Britton-Robinson buffer, pH 7. 77
Figure 3.11 Speciation of Ru_4POM when K^+ ions result in cation-coupled electron transfer and resultant shifts in equilibration. 80
Figure 4.1 Simplified schematic illustrating general composition of some heterogeneous CoWOCs. The purple atoms can represent Co(III) in a Co(II, III) oxide CoO_x material with the green atoms representing tetrahedral Co(II) moieties. In a CoP_i material the purple atoms correspond to Co(II) and the green atoms to PO_4^{3-} moieties. 87
Figure 4.2. Solid-state structure of the Tourné-Weakly ion $[M_4X_2W_{18}O_{68}]^{10-}$ where the central belt is composed of four first-row transition metals. 88

Figure 4.3 Tetracobalt core of $Co_4X_2W_{18}$ POM WOCs shown in (a) side-on~9.5 A across from Co-Co terminal ligands coordinating atom and (b) top-down view, the highlighted area ~6.0 x 9.5 A at its widest........ 89
Figure 4.4 Comparison of the FT-IR spectra from 500-4000 cm^{-1} (top) and zoom of the POM fingerprint region from 500-1200 cm^{-1} (bottom) of hydrophobic TBA derivatives of $Co_4P_2W_{18}$ (blue dashed lines) and $Co_4V_2W_{18}$ (solid brown lines)........ 96
Figure 4.5. The ^{51}V NMR spectra of $Co_4V_2W_{18}$ and $[V_xW_{6-x}]^{(2+x)-}$ POMs (top to bottom); 5 mM $Co_4V_2W_{18}$ as TBA salt in MeCN/CD_3CN (purple) and as Na^+ salt in 10%D_2O/H_2O (green); 5 mM $K_4V_2W_4O_{19}$ (yellow) and 5 mM $TMA_3VW_5O_{19}$ in 10% D_2O/H_2O........ 103
Figure 4.5. The ^{51}V NMR spectrum of $Co_4V_2W_{18}$ taken 30 minutes after dissolution. 5mM $Na_{10}[Co_4V_2W_{18}O_{68}]$•26$H_2O$ in 10% D_2O/H_2O. 600 MHz NMR, 512 scans, relaxation delay = 0.5 s, pulse width = 10 µs, acquisition time = 0.08 s........ 104
Figure 4.6. The ^{51}V NMR spectrum of $Co_4V_2W_{18}$ taken after aging 50 days in the same NMR tube at room temperature. 5mM Na_{10} $[Co_4V_2W_{18}O_{68}]$•26H_2O in 10% D_2O/H_2O. 600 MHz NMR, 512 scans, relaxation delay = 0.5 s, pulse width = 10 µs, acquisition time = 0.08 s........ 105
Figure 4.7. The ^{51}V spectrum of $Co_4V_2W_{18}$ in borate buffer 10 minutes after dissolution. 2.5mM Na_{10} $[Co_4V_2W_{18}O_{68}]$•26H_2O in 240mM sodium borate buffer (pH 8.26) with D_2O in coaxial insert. 600 MHz NMR, 512 scans. Relaxation delay = 0.5 s, pulse width = 10 µs, acquisition time = 0.08 s........ 106
Figure 4.8. The ^{51}V spectrum of $Co_4V_2W_{18}$ in borate buffer 30 minutes after dissolution. 2.5mM $Na_{10}Co_4V_2W_{18}O_{28}$•26$H_2O$ in 240mM sodium borate buffer (pH 8.26) with D_2O in coaxial insert. 600 MHz NMR, 512 scans. Relaxation delay = 0.5 s, pulse width = 10 µs, acquisition time = 0.08 s........ 106
Figure 4.9 X-ray crystal structure of $Co_4P_2W_{18}$ shown as its $[Co_4H_4P_2W_{18}O_{68}]^{6-}$ anion coordinating two MeCN molecules (left) and surrounded by hydrophobic n-Bu_4N^+ counterions. Thermal ellipoids are shown at the 50% probability level........ 108
Figure 4.10 X-ray crystal structure of $Co_4V_2W_{18}$ shown as its $[Co_4H_4V_2W_{18}O_{68}]^{6-}$ anion coordinating two MeCN molecules (a) and surrounded by hydrophobic n-Bu_4N^+ counterions (b). Thermal ellipsoids are shown at the 50% probability level........ 109
Figure 4.11 Solvent-accessible cavities in the X-ray crystal structure of $Co_4M_2W_{18}$, shown here as its $[Co_4H_4V_2W_{18}O_{68}]^{6-}$ anion. Thermal ellipsoids are shown at the 50% probability level........ 110
Figure 4.12 UV-Vis spectra comparison of $Co_4P_4W_{18}$ (dashed blue line) and $Co_4V_4W_{18}$ (solid brown line) in MeCN solvent........ 112
Figure 4.13 UV-Vis spectra comparison of $Co_4P_4W_{18}$ (dashed blue line) and $Co_4V_4W_{18}$ (solid brown line) in 1,2-dichloroethane (DCE) with 0.1 M $TBAPF_6$........ 113
Figure 4.14 UV-Vis spectra comparison of $Co_4P_4W_{18}$ (dashed blue line) and $Co_4V_4W_{18}$ (solid brown line) in tetrahydrofuran (THF) with 0.1 M $TBAPF_6$........ 113
Figure 4.15 Cyclic voltammetry showing single reversible redox couple observed for 500 µM of $Co_4P_2W_{18}$ at a glassy carbon working electrode in MeCN; 0.1 M $TBAPF_6$; scan rate, 25 mV/s (blue dashed line) and 100 mV/s (black solid line)........ 114

Figure 4.16 Cyclic voltammetry showing irreversible oxidation events observed for 2.0 mM $Co_4P_2W_{18}$ in MeCN (solid blue) and resolution of additional features in presence of hydroxide; 0.1 M $TBAPF_6$; scan rate, 50 mV/s. 115

Figure 4.17 Changes in spectra of $Co_4P_2W_{18}$ in the process of bulk electrolysis of $Co_4P_2W_{18}$ in dry MeCN at constant potential, E, in mV, as a function of charge passed through the solution. Conditions: 1 mM $Co_4P_2W_{18}$, 0.1 M $TBAPF_6$, total volume 15 mL, after 0 (pink), 0.4 (orange), 0.56 (red), and 0.8 (black) coulombs were passed. The spectra are recorded in 15-20 min time intervals. 116

Figure 4.18 Spectral changes of the solution after bulk electrolysis of $Co_4P_2W_{18}$ in MeCN. The kinetics of re-reduction is monitored at 560 nm (inset, a solid line is a fitting to an exponential decay with $k_{app} = 5.3 \times 10^{-4}\ s^{-1}$). 117

Figure 4.19 (a) Changes in spectra of 0.25 mM FPIFA and 0.5 mM $Co_4P_2W_{18}$ in MeCN. (b) Dependence of absorbance at 470 nm as a function of time. 118

Figure 4.20. The spectra of intermediates (normalized per absorption at 525 nm) generated electrochemically (red) and in the reaction with FPIFA (blue) 118

Figure 4.21. (a) Changes in spectra of 0.46 mM $[Ru(bpy)_3]^{3+}$ and 0.05 mM $Co_4P_2W_{18}$ in MeCN, total reaction time 100 s. (b) An increase of absorbance at different wavelengths as a function of time: 680 nm (green); 470 (red); and 450 (blue) 119

Figure 4.22. Catalytic consumption of $[Ru(bpy)_3]^{3+}$ in MeCN in 2% H_2O, 0.01 M 2,6-lutidine in the absence of $Co_4P_2W_{18}$ (dotted line) and in the presence of 5 μM $Co_4P_2W_{18}$ (blue line) 120

Figure 4.23. (a) The kinetics of $[Ru(bpy)_3]^{3+}$ consumption measured at 680 nm in 80 mM sodium borate buffer (pH 8.0) in the presence of 2.5 μM $Co_4P_2W_{18}$ at 0 (blue), 1 (green) and 2.5 (red) MeCN (%, v/v). Conditions: 0.36 mM initial $[Ru(bpy)_3](ClO_4)_3$, 25 °C. Black line: no catalyst, no MeCN. (b) The final yield of O_2 per initial $[Ru(bpy)_3](ClO_4)_3$ (in %) as a function of added MeCN. 121

Figure 4.24. Visible spectrum of $Co_4P_2W_{18}$ in MeCN with 0.1 M $TBAPF_6$ during titration with hydroxide (0.1 M TBAOH in MeCN). In MeCN without OH^- (pink, solid line) λ_{max} = 555 nm (ε = 160 L mol^{-1} cm^{-1}); with 2.5 equivalents of OH^- (purple dashed line), λ_{max} = 581 nm (ε = 150 L mol^{-1} cm^{-1}); with 5 equivalents OH^- (solid blue line) λ_{max} = 585 nm (ε = 170 L mol^{-1} cm^{-1}). 123

Figure 4.25 Titrations of $Co_4P_2W_{18}$ with 0.01M NaOH in the presence of 0 (blue) 1 (red) and 3 % MeCN (green) in H_2O 124

Figure 4.26. The dependence of absorbance at 450 nm versus time after mixing 0.25 (blue) or 1.0 (red) mM $Co_4V_2W_{18}$ in water and 1.0 mM DMG in 180 mM NaB buffer (pH 9.0). The dashed line is after mixing of 1.0 M $Co_4V_2W_{18}$ with 180 mM NaB buffer (pH9.0). The dashed line is after mixing of 1.0 M $Co_4V_2W_{18}$ with 180 mM NaB buffer (pH 9.0). 126

Figure 4.27. Light-driven water oxidation oxygen measurements of $Co_4V_2W_{18}$ (blue circles) and $Co_4V_2W_{18}$ mixed with 1 equivalent of bpy per Co atom (a) with 0 minutes of mixing and (b) aging for 1 hour. Conditions: 2 μM $Co_4V_2W_{18}$ 8 μM of bpy, 1.0 mM $[Ru(bpy)_3]Cl_2$, 5.0 mM $Na_2S_2O_8$, 80 mM sodium borate buffer, pH 9.0. 127

Figure 4.28 X-ray Structures of Lindqvist ions (a) VW_5 and (b) V_2W_4 formed as side-products in synthesis and decomposition products of $Co_4V_2W_{18}$. 127

Figure 4.29. Structure of the major product of decomposition of $Co_4V_2W_{18}$ with 2,2′-bipyridine in borate buffer at pH 9. 128

Figure 4.30. Light-driven oxygen measurements for (a) $Co_4V_2W_{18}$ (blue circles) and with aging for 2 hours (red x's) and (b) cis-$[V_2W_4O_{19}]^{4-}$ (magenta stars) and $[VW_5O_{19}]^{3-}$ (black open circles). Inset shows zoomed in oxygen measurements. Conditions: 8 µM POM, 1.0 mM $[Ru(bpy)_3]Cl_2$, 5.0 mM $Na_2S_2O_8$, 80 mM sodium borate buffer, pH 9. 129

Figure 4.31 X-ray crystal structure of the $(DMF)_2Co_4P_2W_{18}$ derivative with N-coordination of DMF solvent molecules. DMF binding was not observed in the vanadium analogue. 130

Figure 4.32. UV-Vis spectra of $Co_4V_2W_{18}$ (solid brown line) and $Co_4P_2W_{18}$ (blue dashed line) in DMF. 131

Figure 4.33 Cyclic voltammetry of $Co_4V_2W_{18}$ in anhydrous DCE. Conditions: 1 mM POM, 0.1 M $TBAPF_6$, scan rate = 50 mV/s 132

Figure 4.34 Cyclic voltammetry of $Co_4V_2W_{18}$ in anhydrous DCE. Conditions: 1 mM POM, 0.1 M $TBAPF_6$, scan rate = 50 mV/s 132

Figure 4.35 Electrochemical film formation on glassy carbon from $Co_4P_2W_{18}$ in anhydrous DCE. Conditions: 1 mM POM, 0.1 M $TBAPF_6$, scan rate = 50 mV/s 133

Figure 4.36 Electrochemical film formation on glassy carbon from $Co_4V_2W_{18}$ in anhydrous DCE. Conditions: 1 mM POM, 0.1 M $TBAPF_6$, scan rate = 50 mV/s 134

Figure 4.37 Scanning electron microscopy image of film formed on glassy carbon from $Co_4P_2W_{18}$ in anhydrous DCE. 135

List of Abbreviations

ATR	attenuated total reflectance
BN	benzonitrile
bpy	2,2’-bipyridine
Co_4P_2	$[Co_4P_2W_{18}O_{68}]^{10-}$
Co_4P_2-H_2O	$[\{Co_4(H_2O)_2\}(PW_9O_{34})_2]^{10-}$
Co_4P_2-MeCN	$[\{Co_4(MeCN)_2\}(PW_9O_{34})_2]^{10-}$
Co_4V_2	$[Co_4V_2W_{18}O_{68}]^{10-}$
Co_9P_5	$[Co_9(H_2O)_6(OH)_3(HPO_4)_2(PW_9O_{34}]^{16-}$
CV	cyclic voltammetry
DCE	1,2-dichloroethane
EDX	energy-dispersive X-ray
EPR	electron paramagnetic resonance
ET	electron transfer
FTIR	Fourier transform infrared
FTO	fluorine-doped tin oxide
MeCN	acetonitrile
MCD	magnetic circular dichroism
NHE	normal hydrogen electrode
NMR	nuclear magnetic resonance
OEC	oxygen-evolving complex
PCET	proton-coupled electron transfer
PFIFA	[Bis(trifluoroacetoxy)iodo]pentafluorobenzene
PhIO	iodosobenzene
PhI	iodobenzene
PhOH	phenol, hydroxybenzene
POM	polyoxometalate
PSII	photosystem II
PT	proton transfer
Ru_4Si_2	$[\{Ru_4O_4(OH)_2(H_2O)_4\}(\gamma\text{-}SiW_{10}O_{36})_2]^{10-}$
SEM	scanning electron microscopy
TBA	tetrabutylammonium
TOF	turnover frequency
TON	turnover number
tren	tris(2-aminoethyl)amine
UV-Vis	ultraviolet-visible
WOC	water oxidation catalyst
WRC	water reduction catalyst
XPS	X-ray photoelectron spectroscopy
XRD	X-ray diffraction

Chapter 1

Background and Introduction to Transition Metal-catalyzed Oxidation

1.1 Introduction to Oxidation Catalysis

1.1.1 Overview of Oxidation Catalysts

Oxidation is the removal of electrons or increase in oxidation state of a substance. This process tends to occur naturally on planet Earth, where the reaction with oxygen is and all things are moving towards oxidation, most often through the thermodynamically favored combination with molecular oxygen, O_2, with a simple uncatalyzed example being the combination of iron with oxygen in the presence of water to form iron oxide, or rust. In most cases, where despite being favorable the process is usually quite slow, the presence of a catalyst greatly accelerates the reaction. Transition metals such as Fe, fellow Group 8 member Ru, and its neighbors Mn and Co are found in some of the most active oxidation catalysts (OCs) in energy-demanding oxidation reactions, such as alkane hydroxylation and water oxidation. When reactivity is optimized and employed in a controlled fashion, effective OCs facilitate degradative processes to decompose and eliminate waste products, work to capture and store energy from the sun in chemical bonds, to functionalize feedstock molecules build complex molecular machinery, to regulate biological functions, and to extract the energy stored in chemical bonds. For modern human life, controlling oxidation reactions through catalysis has been essential and transformative technology. OCs are ubiquitous in Nature, occurring in metallocofactor active sites of transition metal-containing biological catalysts (enzymes) and in chemical industry, typically taking place in high-temperature and/or high-pressure reactors over heterogeneous, solid-state OCs.

Effective oxidation catalysis is especially important now and in the imminent future due to increasing global energy demands, which mandate more efficient chemical industry processes and replacement of environmentally detrimental processes with improved methods based on clean, accessible, and renewable technologies. Metalloenzymes typically operate at ambient temperatures and pressures, using earth-abundant elements. Their metallocofactors may serve as templates for bioinspired models in controlled catalyst design and development. Synthetic models of these active sites can similarly prove valuable to understanding analogous biological processes. Heterogeneous systems that are common in industry can often be modeled by homogeneous molecules which can be more easily adapted, thoroughly characterized, and better studied mechanistically at the molecular level. Examples of molecular OCs in Nature can also often be related to bulk counterparts in industrial and energy applications. Valuable information can be learned from each type of catalytic system that may be relevant to any of the others, and a deeper understanding of molecular OCs remains a rich field of scientific interest. Several themes that commonly appear in scientific pursuits of more effective OCs will be described in more detail in the following sections.

1.1.2 Transition Metal-Oxo Complexes and Selectivity in Oxidation Catalysis

One of the greatest challenges that arises in oxidation catalysis is achieving selectivity, wherein a lack thereof manifests in both catalyst degradation and substrate overoxidation. The oxidation of strong bonds, such as unactivated C-H bonds, requires a potent oxidant, and the supporting ligand scaffold in homogeneous catalysts must be oxidatively stable to avoid self-decomposition.[1] Oxidation is often a multi-electron process that can be coupled to the transfer of protons. In this case, a supporting ligand scaffold must facilitate proton movement and be simultaneously robust hydrolytically.[1]

Most metallocofactors utilize dioxygen in their functions in some capacity. While dioxygen, O_2, is an ideal terminal oxidant, activation of O_2 into more reactive species that can facilitate O transfer often results in radical chemistry which is difficult to control outside of protein environments. When targeting oxygenation or O-atom insertion, a 2-electron process, radical reactions can lead to undesirable side products. Furthermore, substrate oxidation yields activated products which can be more easily oxidized than substrates. As illustrated in Figure 1.1, the monooxygenation of benzene to produce phenol, PhOH, can be hampered by undesired 1-e^- radical coupling reactions to yield biphenyl (and higher) side-products; the 2-e^- oxygenation introduces -OH, a strong electron-donating group (EDG) which activates the arene for further oxidation at the$^-$ *ortho*- and *para*-positions yielding catechol and hydroquinone, which can be further oxidized to *ortho*- and *para*-benzoquinone.

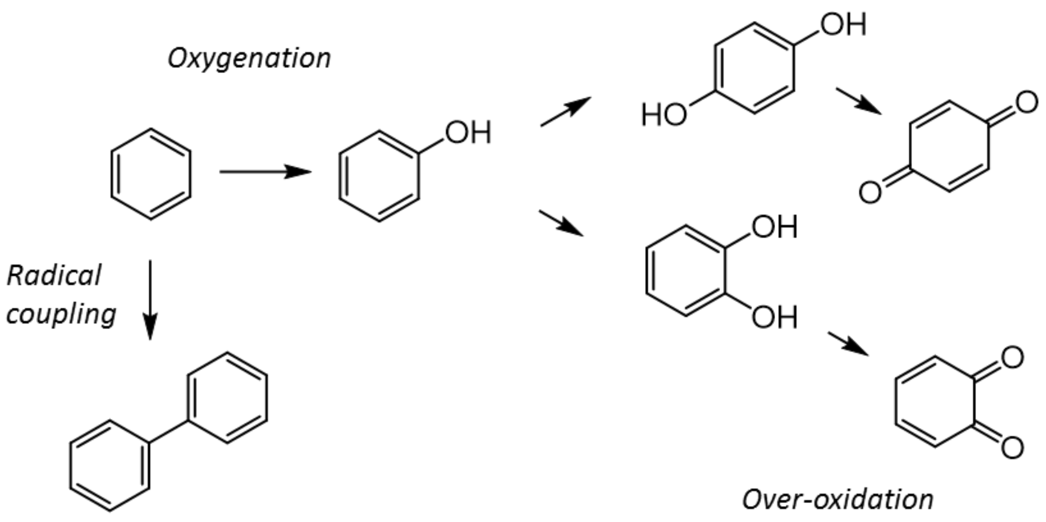

Figure 1.1 Radical coupling side reaction and overoxidation examples in the monooxygenation of benzene.

Many important chemical transformations involving oxygen atoms are mediated by transition metals featuring oxo ligands (O^{2-}), wherein single oxygen atoms are bound to metal centers as either bridging or more rarely, as terminal ligands. Both binding modes may be relevant to mechanisms of oxygen mediation reactions. First-row metal-oxo complexes are recognized as intermediates in a wide variety of important biological processes. The efficacy of these processes in living organisms may be attributed to the controlled formation of highly reactive metal-oxo intermediates, making the most difficult of oxidations feasible; the oxidation of methane to form methanol, for instance, is achieved by the $Fe^{IV}{}_2O_2$ diamond core of methane monooxygenase (MMO).[2] The high degree of selectivity with which the cytochrome P450 (CYP) enzymes operate in the monooxygenation of unactivated hydrocarbons can be attributed to the formation of an Fe^{IV} terminal oxo intermediate. The CYP class of enzymes function through an intermediate Compound I (Cpd I) which has been identified as an $Fe^{IV}=O$ with an additional redox equivalent stored in a π-cation radical on the porphyrin ring.[3] The preference for 2-e^- oxo transfer is a desirable trait in a catalyst where mid- to late-metal-oxo complexes supported by oxidatively stable ligands may impart high selectivity.

1.2 Transition Metal Catalysts for Hydrocarbon Oxidation

1.2.1 Enzymatic Fe-catalyzed Hydrocarbon Oxidation by Cytochrome P450

One of the most important classes of enzymes are the ubiquitous iron-centered CYPs, which are found in all lifeforms.[3] The Fe center is supported by a porphyrin, planar N-heterocyclic ligand commonly referred to as *heme*. CYPs most commonly catalyze monooxygenase reactions, i.e. the insertion of a single oxygen atom into the C-H bond of a hydrocarbon substrate. The CYPs catalyze the hydroxylation of hydrocarbons and the epoxidation of alkenes, and are highly selective in the oxidation of aromatic hydrocarbons, undergoing two-electron oxidation of the substrate, as the aforementioned presence of the non-innocent porphyrin ligand facilitates the formation of the key Fe^{IV}=O intermediate, CpdI.

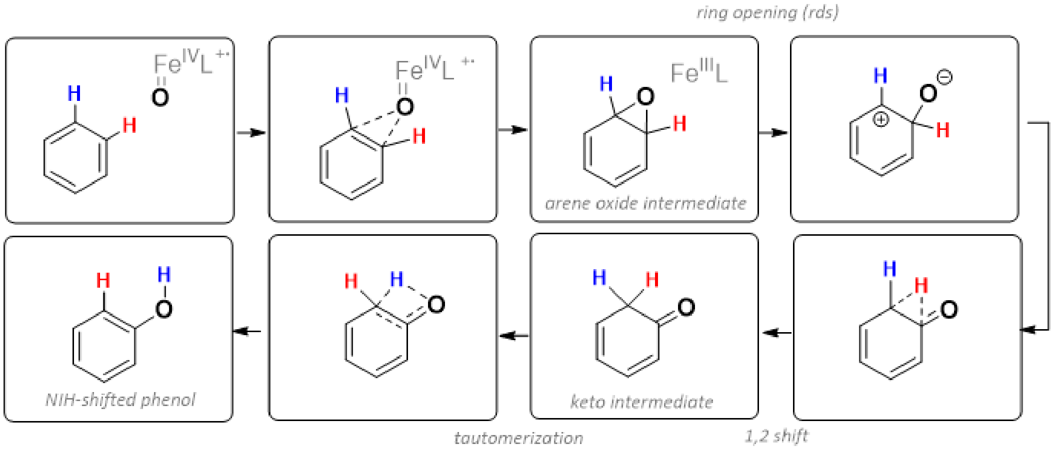

Figure 1.2 The NIH shift mechanism of arene monooxygenation in cytochrome P450

The mechanism of arene oxidation, illustrated in Figure 1.2, then proceeds through an arene oxide intermediate upon oxo-transfer. The rate determining ring-opening step is followed by a 1,2-hydride shift ("NIH shift") with tautomerization of the keto intermediate giving the phenol product.[4] Though outside of enzymes, Fe(III) species are much more likely to undergo a series of linked and self-perpetuating radical reactions, collectively referred to as Fenton chemistry.[5]

1.2.2 The Hock Process for Aromatic Hydrocarbon Oxidation in Chemical Industry

The problem of selectivity in oxidation is well-illustrated by the industrial method for phenol, PhOH, production. PhOH is an important industrial commodity that is produced on an ~7 billion kg scale each year to serve as a precursor for polymers such as phenolic resins, polyamides, polycarbonates, the most important PhOH derivative being bisphenol A. Rather than proceeding through a direct route as in biological systems, industrial-scale oxidation of benzene to produce phenol is accomplished through an indirect three-step route known as the Hock process, or sometimes the "cumene process" due to the isopropylbenzene intermediate that is formed.

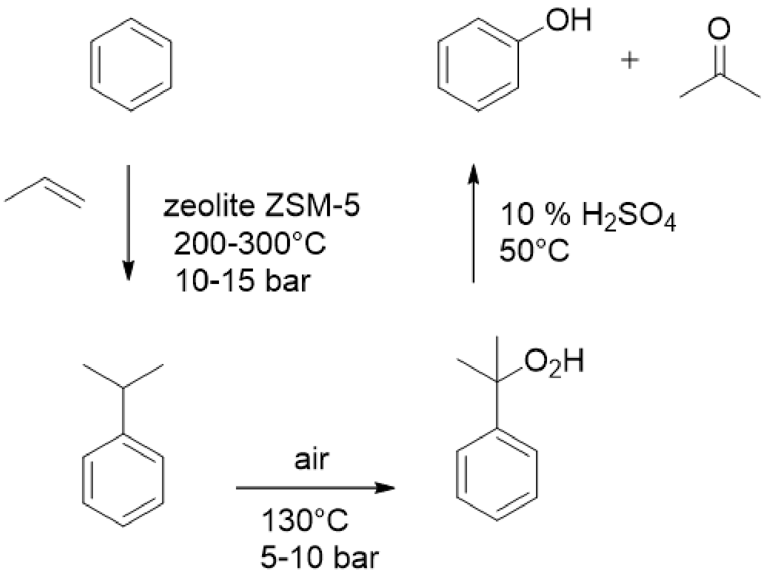

Figure 1.3 Industrial Hock process for production of phenol from benzene.

The first stage is the Friedel-Crafts alkylation of benzene with propylene to yield the cumene intermediate. The cumene is oxidized in air to generate the potentially explosive cumene hydroperoxide. Finally, acid-catalyzed hydrolysis produces the desired phenol product along with one equivalent of acetone. Thus, the currently-employed method for benzene oxygenation suffers not only from inefficiency due to multiple steps involved but also from high energy demand, safety hazards, and the economic challenges of manufacturing two products in set proportions. In this context, a direct route that operates under milder conditions in a selective manner is highly attractive.

1.3 Transition Metal Catalysts for Water Oxidation

1.3.1 Mn-catalyzed Water Oxidation in Photosynthesis

Virtually all life on Earth relies on photosynthesis as a source of energy, whether directly as in plants, cyanobacteria, and some protistans which convert light energy into chemical energy by producing carbohydrates, or indirectly when organisms convert the energy into chemical bonds (as fuel). The capture and conversion of this light energy occurs in Photosystem II (PSII) with photoexcitation of chlorophyll dimers; this pigment with maximum absorption at 680 nm in the red part of the visible spectrum is aptly named P680. Excitation of P680 generates a strong reductant, P680*, which rapidly transfers an electron to a neighboring pheophytin molecule that begins the transfer of electrons through the electron-transport chain. The resultant $P680^+$ is the strongest biological oxidizing agent known, with an estimated redox potential of ~1.3 V.[6] The ground state P680 is regenerated when the electron hole is replenished by the oxidation of water in the neighboring oxygen-evolving complex or OEC.[7] The OEC is a small inorganic cluster of four manganese ions and one calcium ion linked through bridging oxo and hydroxo ligands as well as carboxylate moieties of the protein amino acid residues.[8]

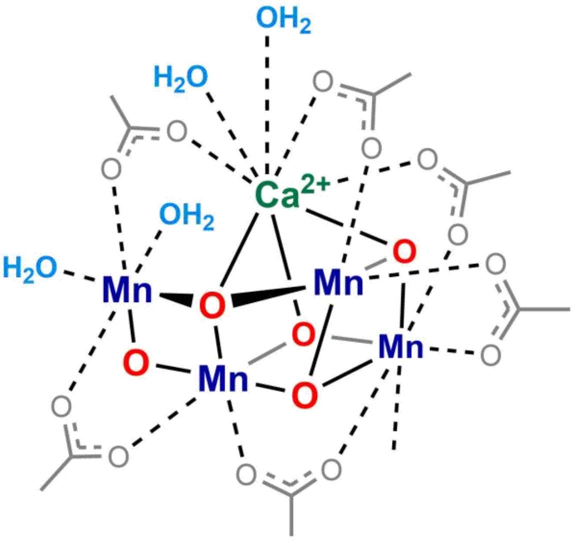

Figure 1.4 Schematic illustration of the oxygen evolving complex, or OEC, in photosynthesis.

While there are roles for other cations in Photosystem II, there is a very specific requirement for Ca^{2+}in the OEC, wherein the depletion of Ca^{2+} arrests the evolution of O_2. Although other cations are known to competitively bind the Ca^{2+} site in the OEC, limited oxygen evolution has been observed with only Sr^{2+}, suggesting that the well-defined protein environment is highly specific for Ca^{2+}. The OEC undergoes four visible light-induced transitions to split water molecules into protons and electrons in steps, and the oxidized intermediates in the catalytic cycle are denoted by their S-states, beginning with S_0 in the resting state and ending with S_4 which releases the dioxygen waste product upon concomitant re-reduction to S_0. As illustrated in Figure 1.5, this is a 4-electron, 4-proton, 4-photon process overall. The Ca^{2+} ion is essential for advancement of the S_2 state and the S_4 state is responsible for the elusive O-O bond forming step.

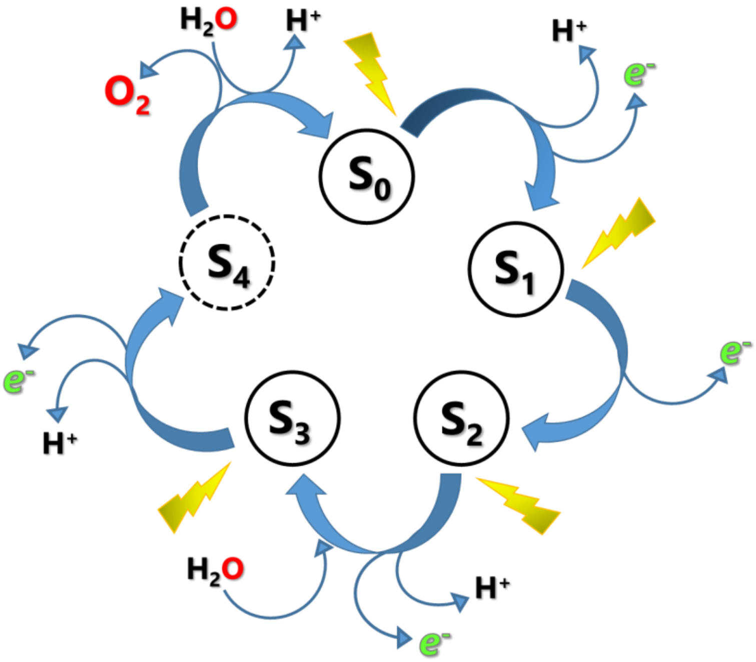

Figure 1.5 Schematic illustration of transitions from S_o through S_4 in the Kok cycle of the OEC in photosynthesis.

1.3.2 Co and Ru Molecular Catalysts for Artificial Water Splitting

The quest for clean and renewable energy is arguably the most important scientific challenge of the 21st century. Solar-powered water splitting is one of the most promising routes to clean and renewable energy, which can be stored in energy-dense fuels such as H_2 or for producing liquid fuels from CO_2. Coupling of a WOC and a photosensitizer at the photoanode and a water-reduction catalyst (WRC) to make H_2 at the cathode produces a photoelectrochemical cell (PEC).

Transition metal oxides based on Ru and Ir are the most well-established and extensively studied heterogeneous WOCs, where the cubane-like metal-oxygen structural motif and high oxidation states are common features in these systems.[9] Of these, iridium-based materials are the most active and stable catalysts.[10] Due to the prohibitive cost of precious metals, materials based on abundant elements have attracted attention, with Co, Ni, and Ni/Fe oxides[11] and amorphous phosphate-containing Co materials[12] emerging as promising catalysts for light-driven water oxidation. Deciphering the mechanism of water oxidation in heterogeneous systems is not straightforward due to the difficulty of identifying surface-adsorbed intermediates, and thus molecular analogues of these metal-oxide surfaces are highly sought for mechanistic studies. The first artificial homogeneous WOC, reported in 1982, the "Blue Dimer," or BD, $[(bpy)_2Ru(H_2O)(\mathit{m}\text{-}O)Ru(H_2O)(bpy)_2]^{4+}$, was used to probe the mechanism of O-O bond formation.[13] Two main pathways were identified using isotopic labeling; the primary route involves nucleophilic attack of unbound water on a high-valent Ru-oxo in the water nucleophilic attack (WNA) mechanism. A second pathway involving ligand oxidation and hydration is less clearly-defined, but the studies ruled out the direct oxo coupling pathway (OCP) of adjacent Ru^V=O to form O_2. In contrast, related Hbpp-Ru dimers (Hbpp = 3,5-bis(2-pyridyl)pyrazole) were shown to undergo OCP rather than NWA.[14]

The highly oxidizing environment generally required to split water is typically sufficient to oxidize all organic functions. This defines an intrinsic limit to the utility of such molecular species as homogeneous WOCs.[15] The BD loses activity due to degradation of the organic ligands. The Hbbp-Ru catalysts evolve both O_2 and CO_2, where the CO_2 is believed to result from ligand oxidation.[16] A mononuclear Ru catalyst with an [ONO]-pincer ligand achieves up to 4000 turnovers but is rapidly deactivated within 15 minutes, presumably due to facile oxidation of the phenol group in the ligand scaffold.[17] The Dismukes tetramanganese Mn_4O_4 was shown to decompose to manganese oxide materials under electrochemical oxidation.[18] Analogous tetranuclear Co_4O_4 cubane compounds have been reported as molecular WOCs[19] but it subsequent studies revealed the catalytic activity emanates from a Co(II) impurity.[20] Mononuclear cobalt porphyrins have been established as homogeneous WOCs but oxidation of the porphyrin ligand occurs after a few turnovers.[21]

Polyoxometalates (POMs) are soluble clusters of metal oxides (e.g. WO_4^{2-}) that have emerged as an extensive class of compounds that are stable over a wide range of pH, temperature, and potentials.[22] In their lacunary forms, they can also be used as oxidatively stable ligand scaffolds for transition metal-oxide fragment clusters. The resulting multi-metal complexes exhibit a wide range of nuclearities, geometries, and chemical properties that resemble their heterogeneous counterparts. These highly charged species are capable of multiple electron transfers and thus have been explored as homogeneous catalysts for a variety of chemical transformations, particularly in the realm of water oxidation and the production of green fuels.[23] Due to this combination of desirable traits, POMs have emerged as perhaps the most promising molecular class of WOCs. Among the most well-studied of these are the $[\{Ru_4O_4(\gamma\text{-}XW_{10}O_{36})_2]^{10-}$, **$Ru_4$POM**s (X=Si or P, show in Figure 1.6, left panel) which is stable over a wide pH range and operates with turnover frequencies of ~1 mol O_2 s^{-1} at pH 7.[24] Studies of specific cation effects for the for the Si-analogue, $[\{Ru_4O_4(\gamma\text{-}SiW_{10}O_{36})_2]^{10-}$, of this WOC are presented in Chapter 3. More recently the $[Co_4(\alpha\text{-}XW_9O_{34})_2]$10- **$Co_4$POM**s, shown at right in Figure 1.6, where X=P[25] or V[26], have been reported. These WOCs are more appealing due to both their facile self-assembly from abundant elements and catalytic speeds of up to ~6 s^{-1} and ~1,000 s^{-1}, respectively, but also suffer from electrochemical and hydrolytic instability.[27] Studies on the electrochemical properties and solution stability of the **Co_4POM**s are presented in Chapter 4.

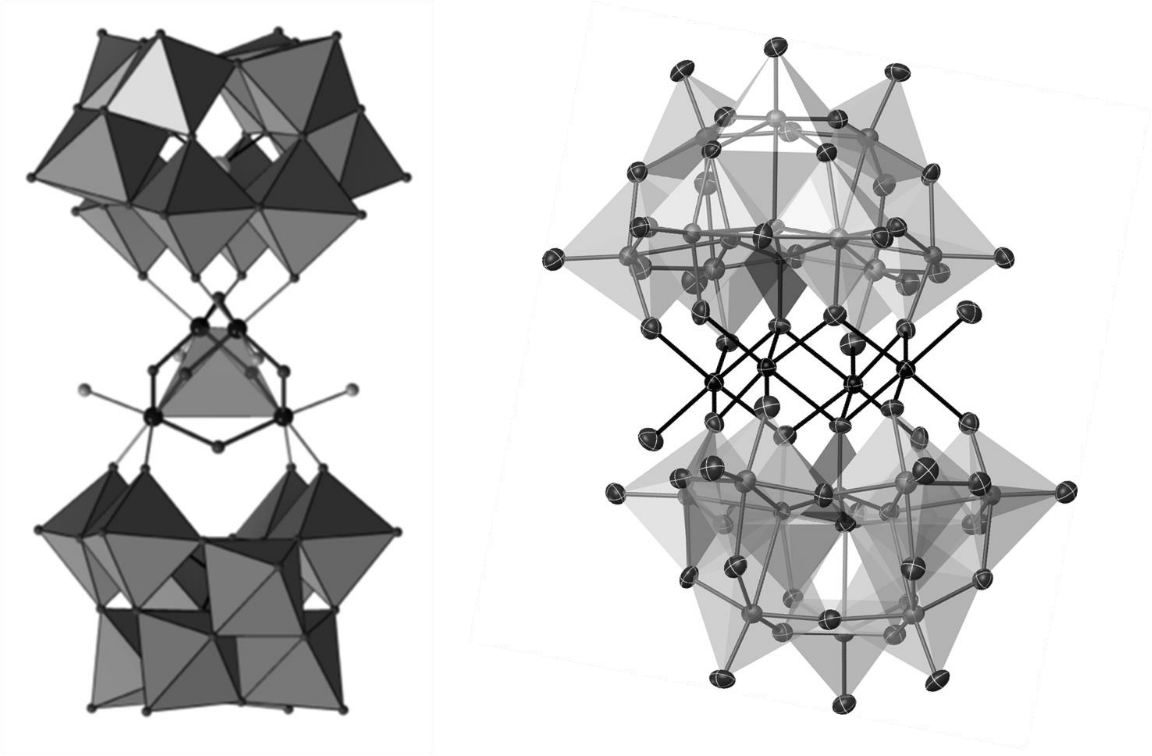

Figure 1.6 General structure of Ru_4POM (left) and Co_4POM (right) polyoxometalates (POMs) that are under investigation as homogeneous water oxidation catalysts (WOCs).

1.4 Non-innocent Ligands, Anions, and Cations in Oxidation Catalysis

Redox non-innocent ligands, such as the porphyrin in cytochrome P450 can act as temporary stores for redox equivalents. In cobalt-porphyrin WOCs, ligand oxidation leads to catalyst degradation. In contrast, a Ru quaterpyridine catalyst does not lose water oxidation activity upon oxidation of the pyridyl groups because the ligand is converted to *bis*-N-oxide. [28] Thus, ligand modification under reaction conditions may be important in dictating mechanisms of catalytic oxidation.[28]

Anions have also been shown to play non-innocent roles in oxidation catalysis. Interestingly, nitrate from cerium(IV) ammonium nitrate, CAN, was found to be non-innocent in the dynamics of O_2 evolution by the BD. Chloride was also more recently found to participate in electrochemical water oxidation by a mononuclear Ru catalyst by forming HOCl, which is further oxidized to O2.[29] Buffer base anions were shown to enhance water oxidation rates with carboxylate-bipyridine Ru(II) WOCs by direct involvement in atom-proton transfer (APT) or proton coupled electron transfer (PCET).[30]

Specific alkali cation effects have been observed to have important activating properties in both heterogeneous catalysts and molecular complexes capable of reducing dinitrogen.[31] While some non-innocent effects of ligands and anions have been well-established in oxidation, and specific cation effects are notable in nitrogen reduction catalysis, the countercations have largely been disregarded as spectator ions in transition metal oxidation catalysts. Redox-inert cations have recently begun to emerge as potential stabilizers of high-valent metal-oxo species. In photosynthesis, both the OEC and the enzyme that catalyzes the first step in CO_2 fixation, Ribulose-1,5-bisphosphate carboxylase/oxygenase, commonly known as RuBisCO, require redox-inert ions in order to operate. The addition of CO_2 to a lysine residue in the active site to form a carbamate is facilitated by proper positioning of Mg^{2+} ions.[32] On the other hand, the question regarding the role of Ca^{2+} in the OEC has been of major interest since the structure was first determined in 2001 and remains without a clear answer.[33] Although other cations are known to competitively bind the Ca^{2+} site in the OEC, limited oxygen evolution has been observed with only Sr^{2+}, suggesting that the well-defined protein environment is highly specific for Ca^{2+}. Substitution of cadmium has facilitated ^{113}Cd-NMR studies that suggest the Ca^{2+} site is close enough to be affected by the Mn_4 cluster spin state.[34] X-ray Absorption Spectroscopy (XAS) studies[35] and EPR studies[36] of calcium- and strontium-containing PSII have provided some insights into this requirement for calcium in the OEC.

In artificial WOCs, it was shown that high surface area $CaMn_2O_4$ materials are more active for water oxidation than manganese(III) oxide materials without calcium.[37] Model complexes that strongly resemble the manganese-oxido cluster of the OEC have recently elucidated some redox properties that may illuminate S-state transitions in the OEC.[38] Other models supported by organic ligands have been synthesized and the substitution of various cations has allowed extrapolation of a linear relationship between the redox potential of the manganese cluster and the Lewis-acidity of the ion.[39] A similar linear correlation between Lewis-acidity and redox potential was observed in a mononuclear Fe^{III}-peroxo complex that bind redox-inactive metal ions; dioxygen release was induced by 1-e^- oxidation only in the case of Ca^{2+} and Sr^{2+} whereas more Lewis-acidic ions rendered the complexes inert to this reaction.[38] Thus it has been suggested that Ca^{2+} is not only involved in O-O bond formation, but also facilitates catalytic turnover, wherein a more Lewis-acidic ion (e.g. Zn^{2+}) may interfere with dioxygen release. The strong indications that specific cations play important roles in enzymatic processes which are not fully understood, may lead to the formation of otherwise-unstable metal-oxo species, and can modulate electron transfer in POMs. In short, counteraction interactions offer very substantial potential for advances in selective, efficient catalytic oxidation and our mechanistic understanding of these processes.

1.5 Hypothesis and Scope of this Work

Catalytic oxidation is of utmost importance to numerous chemical transformations that are essential to life on earth, whether accomplished enzymatically in Nature or artificially through industrial processes. Selectivity and stability of OCs still suffers from several deficiencies but a strong and steady flow of significant developments, intermittent controversy, and numerous unanswered questions maintain this as a scientifically lively research area. One phenomenon which has been studied to lesser extent is the role of cations in oxidation catalysis. Examples from natural and artificial OCs show promise that cations may be more important than previously realized. This work spans three interrelated parts exploring the central hypothesis:

> *Specific interactions of redox-inert alkali metal cations impact electron, proton- and oxo-transfer mechanisms of transition metal-catalyzed oxidation processes.*

In the case of *non-innocent countercation interactions*, secondary sphere coordination of redox-inactive alkali metal cations in anionic Co and Ru oxidation catalysts dictate specific effects on the mechanism of action, kinetics, and selectivity in both catalytic arene oxygenation and water oxidation. In contrast, weakly-interacting, hydrophobic countercations in these systems dramatically limit reactivity in oxygen mediation reactions, i.e. both arene and water oxidation. These *innocent counteraction interactions* facilitate studies of the stability, redox and acid-base properties of the anions, which proves to be especially valuable for comparing systems such as isostructural POMs in different (aqueous and non-aqueous) media.

In the first chapter to follow, the effect of Ca^{2+} counterions in anionic, tripodal Co(II) complexes on the formation of isolable Co^{IV}-oxo species is described. This bioinspired catalyst features a rationally-designed ligand scaffold based on molecular orbital theory and additional design considerations aimed to impart stability and catalyst-controlled selectivity in the monooxygenation of benzene to yield phenol. The results show that Ca^{2+} activates the Co(II) center for predominantly 2-electron oxo-transfer reactivity towards benzene. Spectroscopic evidence suggests the formation of a transient Co^{IV}-oxo species, and X-ray crystallography points to not only activation of Co(II) by Ca^{2+}, but also participation of the sulfonamide ligand scaffold in generating a Co(II)-peroxysulfonimidate that may be the sole isolable precursor to the transient terminal-oxo species.

In the following chapter, the search for an analogous counteraction effect continues in the ever-important water oxidation reaction, where it is known to be crucial in Nature, and is demonstrated with K^+ in the **Ru_4POM**s, an important and well-established class of homogeneous WOCs. Surprisingly, the K^+ effects, which include cation-coupled electron transfer (CCET), are not collectively beneficial for light-driven water oxidation catalysis and introduce mechanistic branching by changing the speciation of equilibrated species in solution. In contrast, K^+ ions stabilize reduced forms of the **Ru_4POM**s and these ions (as well as possibly Ba^{2+} and NH_4^+) may be beneficial for accessing reductive catalysis in these POMs.

After demonstrating both beneficial (Ca^{2+} with Co) and potentially detrimental (K^+ with Ru) effects of specific alkali cations that are important for oxidation catalysis, the alternative case is explored with Co-based POMs where weakly-interacting countercations minimally impact catalytic activity, but are essential for stabilization of these hydrolytically sensitive compounds in non-aqueous media. Surrounding the highly anionic **Co_4POM** complexes with alkylammonium counterions mimics the hydrophobic environment of a protein. By limiting the reactivity with substrate water, reactive properties of the anion that have remained elusive in aqueous media can be probed and more thoroughly studied in organic solvents. These studies reveal several important insights into the stability and mechanism of water oxidation in the two isostructural **Co_4POM**s.

In the final chapter, some additional preliminary investigations into the roles of the smallest of cation – proton, are presented, with studies into protonation state changes in water oxidation catalysts and implications for proton movement dynamics in solution. An outlook and proposals for continued research pathways and promising future directions based on the investigations presented is provided. Countercations can facilitate, modulate, and tune the redox and acid-base properties of the transition-metal active site to various extents. In cases where the cation is innocent, the anion can be studied in greater detail. Countercations can act as more than just spectator ions and may induce catalysis that is not accessible in their absence. in some cases, they may hinder reactivity, which can be useful in many molecular studies. Therefore, the careful studies of the innocent and non-innocent countercation interactions are insightful for catalyst design and development.

1.6 References

1. Crabtree, R. H., Deactivation in Homogeneous Transition Metal Catalysis: Causes, Avoidance, and Cure. *Chem. Rev.* **2015,** *115* (1), 127-150.

2. Shu, L.; Nesheim, J. C.; Kauffmann, K.; Münck, E.; Lipscomb, J. D.; Que, L., An Fe2IVO2 Diamond Core Structure for the Key Intermediate Q of Methane Monooxygenase. *Science* **1997,** *275* (5299), 515-518.

3. Denisov, I. G.; Makris, T. M.; Sligar, S. G.; Schlichting, I., Structure and Chemistry of Cytochrome P450. *Chem. Rev.* **2005,** *105* (6), 2253-2278.

4. Jerina, D. M.; Kaubisch, N.; Daly, J. W., Arene Oxides as Intermediates in the Metabolism of Aromatic Substrates: Alkyl and Oxygen Migrations during Isomerization of Alkylated Arene Oxides. *Proc. Natl. Acad. Sci. U. S. A.* **1971,** *68* (10), 2545-2548.

5. Winterbourn, C. C., Toxicity of iron and hydrogen peroxide: the Fenton reaction. *Toxicol. Lett.* **1995,** *82*, 969-974.

6. Rappaport, F.; Guergova-Kuras, M.; Nixon, P. J.; Diner, B. A.; Lavergne, J., Kinetics and Pathways of Charge Recombination in Photosystem II. *Biochemistry* **2002,** *41* (26), 8518-8527.

7. Yano, J.; Yachandra, V., Mn(4)Ca Cluster in Photosynthesis: Where and How Water is Oxidized to Dioxygen. *Chem. Rev.* **2014,** *114* (8), 4175-4205.

8. Suga, M.; Akita, F.; Hirata, K.; Ueno, G.; Murakami, H.; Nakajima, Y.; Shimizu, T.; Yamashita, K.; Yamamoto, M.; Ago, H.; Shen, J.-R., Native structure of photosystem II at 1.95 A resolution viewed by femtosecond X-ray pulses. *Nature* **2015,** *517* (7532), 99-103.

9. (a) Harriman, A.; Pickering, I. J.; Thomas, J. M.; Christensen, P. A., Metal Oxides as Heterogeneous Catalysts for Oxygen Evolution under Photochemical Conditions. *J. Chem. Soc.,*

Faraday Trans. 1 F **1988,** *84* (8), 2795-2806; (b) Harriman, A.; Richoux, M.-C.; Christensen, P. A.; Mosseri, S.; Neta, P., Redox Reactions with Colloidal Metal Oxides: Comparison of Radiation-generated and Chemically generated RuO_2•$2H_2O$ and MnO_2 Colloids. *J. Chem. Soc., Faraday Trans. 1 F* **1987,** *83* (9), 3001-3014.

10. Chen, X.; Chen, G.; Yue, P. L., Stable Ti/IrOx−Sb2O5−SnO2 Anode for O2 Evolution with Low Ir Content. *J. Phys. Chem. B* **2001,** *105* (20), 4623-4628.

11. (a) McCrory, C. C. L.; Jung, S.; Ferrer, I. M.; Chatman, S. M.; Peters, J. C.; Jaramillo, T. F., Benchmarking Hydrogen Evolving Reaction and Oxygen Evolving Reaction Electrocatalysts for Solar Water Splitting Devices. *J. Am. Chem. Soc* **2015,** *137*, 4347-4357; (b) Gerken, J. B.; McAlpin, J. G.; Chen, J. Y. C.; Rigsby, M. L.; Casey, W. H.; Britt, R. D.; Stahl, S. S., Electrochemical Water Oxidation with Cobalt-Based Electrocatalysts from pH 014: The Thermodynamic Basis for Catalyst Structure, Stability, and Activity. *J. Am. Chem. Soc.* **2011,** *133*, 14431-14442; (c) Blakemore, J. D.; Gray, H. B.; Winkler, J. R.; Müller, A. M., Co3O4 Nanoparticle Water-Oxidation Catalysts Made by Pulsed-Laser Ablation in Liquids. *ACS Catal.* **2013,** *3* (11), 2497-2500; (d) Hunter, B. M.; Blakemore, J. D.; Deimund, M.; Gray, H. B.; Winkler, J. R.; Müller, A. M., Highly Active Mixed-Metal Nanosheet Water Oxidation Catalysts Made by Pulsed-Laser Ablation in Liquids. *J. Am. Chem. Soc.* **2014,** *136* (38), 13118-13121.

12. (a) Surendranath, Y.; Lutterman, D. A.; Liu, Y.; Nocera, D. G., Nucleation, Growth, and Repair of a Cobalt-Based Oxygen Evolving Catalyst. *J. Am. Chem. Soc.* **2012,** *134* (14), 6326-6336; (b) Nocera, D. G., The Artificial Leaf. *Acc. Chem. Res.* **2012,** *45* (5), 767-776; (c) Surendranath, Y.; Kanan, M. W.; Nocera, D. G., Mechanistic Studies of the Oxygen Evolution Reaction by a Cobalt-Phosphate Catalyst at Neutral pH. *J. Am. Chem. Soc.* **2010,** *132*, 16501-16509; (d) Surendranath,

Y.; Dincă, M.; Nocera, D. G., Electrolyte-Dependent Electrosynthesis and Activity of Cobalt-Based Water Oxidation Catalysts

J. Am. Chem. Soc. **2009,** *131*, 2615-2620; (e) Lutterman, D. A.; Surendranath, Y.; Nocera, D. G., A Self-Healing Oxygen-Evolving Catalyst. *J. Am. Chem. Soc.* **2009,** *131*, 3838-3839; (f) Kanan, M. W.; Surendranath, Y.; Nocera, D. G., Cobalt–phosphate oxygen-evolving compound. *Chem. Soc. Rev.* **2009,** *38*, 109-114.

13. (a) Gersten, S. W.; Samuels, G. J.; Meyer, T. J., Catalytic Oxidation of Water by an Oxo-Bridged Ruthenium Dimer. *J. Am. Chem. Soc.* **1982,** *104*, 4029-4030; (b) Gilbert, J. A.; Eggleston, D. S.; Wyatt R. Murphy, J.; Geselowitz, D. A.; Gersten, S. W.; Hodgson, D. J.; Meyer, T. J., Structure and Redox Properties of the Water-Oxidation Catalyst $[(bpy)_2(OH_2)RuORu(OH_2)(bpy)_2]^{4+}$. *J. Am. Chem. Soc.* **1985,** *107* (13), 3855-3864; (c) Clark, A. E.; Hurst, J. K., Mechanisms of Water Oxidation Catalyzed by Ruthenium Coordination Complexes. In *Prog. Inorg. Chem.*, John Wiley & Sons, Inc.: 2011; pp 1-54.

14. Romain, S.; Bozoglian, F.; Sala, X.; Llobet, A., Oxygen—Oxygen Bond Formation by the Ru-Hbpp Water Oxidation Catalyst Occurs Solely via an Intramolecular Reaction Pathway. *J. Am. Chem. Soc.* **2009,** *131*, 2768-2769.

15. Limburg, B.; Bouwman, E.; Bonnet, S., Molecular water oxidation catalysts based on transition metals and their decomposition pathways. *Coord. Chem. Rev.* **2012,** *256* (15–16), 1451-1467.

16. Francàs, L.; Sala, X.; Escudero-Adán, E.; Benet-Buchholz, J.; Escriche, L.; Llobet, A., Synthesis, Structure, and Reactivity of New Tetranuclear Ru-Hbpp-Based Water-Oxidation Catalysts. *Chem. Commun.* **2011,** *50*, 2771-2781.

17. Kärkäs, M. D.; Åkermark, T.; Johnston, E. V.; Karim, S. R.; Laine, T. M.; Lee, B.-L.; Åkermark, T.; Privalov, T.; Åkermark, B., Water Oxidation by Single-Site Ruthenium Complexes: Using Ligands as Redox and Proton Transfer Mediators. *Angew. Chem. Int. Ed.* **2012,** *51* (46), 11589-11593.

18. (a) McCool, N. S.; Robinson, D. M.; Sheats, J. E.; Dismukes, G. C., A Co_4O_4 "Cubane" Water Oxidation Catalyst Inspired by Photosynthesis. *J. Am. Chem. Soc.* **2011,** *133*, 11446-11449; (b) Berardi, S.; Ganga, G. L.; Natali, M.; Bazzan, I.; Puntoriero, F.; Sartorel, A.; Scandola, F.; Campagna, S.; Bonchio, M., Photocatalytic Water Oxidation: Tuning Light-Induced Electron Transfer by Molecular Co_4O_4 Cores. *J. Am. Chem. Soc.* **2012,** *134*, 11104-11107; (c) Genoni, A.; La Ganga, G.; Volpe, A.; Puntoriero, F.; Di Valentin, M.; Bonchio, M.; Natali, M.; Sartorel, A., Water oxidation catalysis upon evolution of molecular Co(III) cubanes in aqueous media *Faraday Discuss.* **2015**, Published online 10 June 2015.

19. Ullman, A. M.; Liu, Y.; Huynh, M.; Bediako, D. K.; Wang, H.; Anderson, B. L.; Powers, D. C.; Breen, J. J.; Abruña, H. D.; Nocera, D. G., Water Oxidation Catalysis by Co(II) Impurities in $Co(III)_4O_4$ Cubanes. *J. Am. Chem. Soc.* **2014,** *136*, 17681-17688.

20. (a) Nakazono, T.; Parent, A. R.; Sakai, K., Cobalt porphyrins as homogeneous catalysts for water oxidation. *Chem. Commun.* **2013,** *49* (56), 6325-6327; (b) Wang, D.; Groves, J. T., Efficient water oxidation catalyzed by homogeneous cationic cobalt porphyrins with critical roles for the buffer base. *Proc. Natl. Acad. Sci.* **2013,** *110* (39), 15579-15584.

21. Pope, M. T., Polyoxo Anions: Synthesis and Structure. In *Comprehensive Coordination Chemistry II: From Biology to Nanotechnology*, Wedd, A. G., Ed. Elsevier Ltd.: Oxford, UK, 2004; Vol. 4, pp 635-678.`

22. (a) Lv, H.; Hill, C. L., Polyoxometalate-Based Multi-Electron-Transfer Catalysts in Solar Fuel Chemistry. *Acc. Chem. Res.* **2015** submitted Aug 18, 2015; (b) Lv, H.; Geletii, Y. V.; Zhao, C.; Vickers, J. W.; Zhu, G.; Luo, Z.; Song, J.; Lian, T.; Musaev, D. G.; Hill, C. L., Polyoxometalate water oxidation catalysts and the production of green fuel. *Chem. Soc. Rev.* **2012,** *41*, 7572-7589.

23. (a) Sartorel, A.; Carraro, M.; Scorrano, G.; Zorzi, R. D.; Geremia, S.; McDaniel, N. D.; Bernhard, S.; Bonchio, M., Polyoxometalate Embedding of a Tetraruthenium(IV)-oxo-core by Template-Directed Metalation of $[\gamma\text{-SiW}_{10}O_{36}]^{8-}$: A Totally Inorganic Oxygen-Evolving Catalyst. *J. Am. Chem. Soc.* **2008,** *130* (15), 5006-5007; (b) Geletii, Y. V.; Botar, B.; Kögerler, P.; Hillesheim, D. A.; Musaev, D. G.; Hill, C. L., An All-Inorganic, Stable, and Highly Active Tetraruthenium Homogeneous Catalyst for Water Oxidation. Selected as the VIP Article by the reviewers and editor. *Angew. Chem. Int. Ed.* **2008,** *47*, 3896-3899.

24. Yin, Q.; Tan, J. M.; Besson, C.; Geletii, Y. V.; Musaev, D. G.; Kuznetsov, A. E.; Luo, Z.; Hardcastle, K. I.; Hill, C. L., A fast soluble carbon-free molecular water oxidation catalyst based on abundant metals. *Science* **2010,** *328*, 342-345.

25. Lv, H.; Song, J.; Geletii, Y. V.; Vickers, J. W.; Sumliner, J. M.; Musaev, D. G.; Kögerler, P.; Zhuk, P. F.; Bacsa, J.; Zhu, G.; Hill, C. L., An Exceptionally Fast Homogeneous Carbon-free Cobalt-based Water Oxidation Catalyst. *J. Am. Chem. Soc.* **2014,** *136* (26), 9268-9271.

26. (a) Folkman, S. J.; Finke, R. G., Electrochemical Water Oxidation Catalysis Beginning with Co(II) Polyoxometalates: The Case of the Precatalyst $Co_4V_2W_{18}O_{68}^{10-}$. *ACS Catal.* **ASAP November 23, 2016,** *7*, 7-17; (b) Folkman, S. J.; Kirner, J. T.; Finke, R. G., Cobalt Polyoxometalate $Co_4V_2W_{18}O_{68}^{10-}$: A Critical Investigation of Its Synthesis, Purity, and Observed ^{51}V Quadrupolar NMR. *Inorg. Chem.* **2016,** *55* (11), 5343-5355; (c) Stracke, J. J.; Finke, R. G., Water Oxidation

Catalysis Beginning with $Co_4(H_2O)_2(PW_9O_{34})_2^{10-}$ When Driven by the Chemical Oxidant Ruthenium(III)tris(2,2′-bipyridine): Stoichiometry, Kinetic, and Mechanistic Studies en Route to Identifying the True Catalyst. *ACS Catal.* **2014,** *4*, 79-89; (d) Stracke, J. J.; Finke, R. G., Water Oxidation Catalysis Beginning with 2.5 µM [Co4(H2O)2(PW9O34)2]10–: Investigation of the True Electrochemically Driven Catalyst at ≥600 mV Overpotential at a Glassy Carbon Electrode. *ACS Catal.* **2013,** *3* (6), 1209-1219; (e) Stracke, J. J.; Finke, R. G., Electrocatalytic Water Oxidation Beginning with the Cobalt Polyoxometalate $[Co_4(H_2O)_2(PW_9O_{34})_2]^{10-}$: Identification of Heterogeneous CoO_x as the Dominant Catalyst. *J. Am. Chem. Soc.* **2011,** *133*, 14872-14875.

27. Liu, Y.; Ng, S.-M.; Yiu, S.-M.; Lam, W. W. Y.; Wei, X.-G.; Lau, K.-C.; Lau, T.-C., Catalytic Water Oxidation by Ruthenium(II) Quaterpyridine (qpy) Complexes: Evidence for Ruthenium(III) qpy-N,N′′′-dioxide as the Real Catalysts. *Angew. Chem. Int. Ed.* **2014,** *53* (52), 14468-14471.

28. Chen, Z.; Concepcion, J. J.; Song, N.; Meyer, T. J., Chloride-assisted catalytic water oxidation. *Chem. Commun.* **2014,** *50*, 8053-8056.

29. Song, N.; Concepcion, J. J.; Binstead, R. A.; Rudd, J. A.; Vannucci, A. K.; Dares, C.; Coggins, M. K.; Meyer, T. J., Base Enhanced Catalytic Water Oxidation by a Carboxylate-Bipyridine Ru(II) Complex. *Proc. Natl. Acad. Sci.* **2015,** *112* (16), 4935-4940.

30. Connor, G. P.; Holland, P. L., Coordination chemistry insights into the role of alkali metal promoters in dinitrogen reduction. *Catal. Today* **2017,** *286*, 21-40.

31. Andersson, I., Catalysis and regulation in Rubisco. *J. Exp. Bot.* **2008,** *59* (7), 1555-1568.

32. Paul, S.; Neese, F.; Pantazis, D. A., Structural models of the biological oxygen-evolving complex: achievements, insights, and challenges for biomimicry. *Green Chem.* **2017**.

33. Matysik, J.; Alia; Nachtegaal, G.; van Gorkom, H. J.; Hoff, A. J.; de Groot, H. J. M., Exploring the Calcium-Binding Site in Photosystem II Membranes by Solid-State 113Cd NMR. *Biochemistry* **2000,** *39* (23), 6751-6755.

34. Yachandra, V. K.; Yano, J., Calcium in the Oxygen-Evolving Complex: Structural and Mechanistic Role Determined by X-ray Spectroscopy. *Journal of photochemistry and photobiology. B, Biology* **2011,** *104* (1-2), 51-59.

35. (a) Pushkar, Y.; Yano, J.; Sauer, K.; Boussac, A.; Yachandra, V. K., Structural changes in the Mn(4)Ca cluster and the mechanism of photosynthetic water splitting. *Proc. Natl. Acad. Sci. U. S. A.* **2008,** *105* (6), 1879-1884; (b) Cinco, R. M.; Holman, K. L. M.; Robblee, J. H.; Yano, J.; Pizarro, S. A.; Bellacchio, E.; Sauer, K.; Yachandra, V. K., Calcium EXAFS Establishes the Mn-Ca Cluster in the Oxygen-Evolving Complex of Photosystem II(). *Biochemistry* **2002,** *41* (43), 12928-12933; (c) Cinco, R. M.; Robblee, J. H.; Rompel, A.; Fernandez, C.; Yachandra, V. K.; Sauer, K.; Klein, M. P., Strontium EXAFS Reveals the Proximity of Calcium to the Manganese Cluster of Oxygen-Evolving Photosystem II. *The journal of physical chemistry. B* **1998,** *102* (42), 8248-8256; (d) Kim, S. H.; Gregor, W.; Peloquin, J. M.; Brynda, M.; Britt, R. D., Investigation of the Calcium-Binding Site of the Oxygen Evolving Complex of Photosystem II Using 87Sr ESEEM Spectroscopy. *J. Am. Chem. Soc.* **2004,** *126* (23), 7228-7237.

36. Najafpour, M. M.; Ehrenberg, T.; Wiechen, M.; Kurz, P., Calcium Manganese(III) Oxides (CaMn2O4·x H2O) as Biomimetic Oxygen-Evolving Catalysts. *Angew. Chem. Int. Ed.* **2010,** *49* (12), 2233-2237.

37. Bang, S.; Lee, Y.-M.; Hong, S.; Cho, K.-B.; Nishida, Y.; Seo, M. S.; Sarangi, R.; Fukuzumi, S.; Nam, W., Redox-inactive metal ions modulate the reactivity and oxygen release of mononuclear non-haem iron(III)–peroxo complexes. *Nat Chem* **2014,** *6* (10), 934-940.

38. (a) Tsui, E. Y.; Agapie, T., Reduction potentials of heterometallic manganese–oxido cubane complexes modulated by redox-inactive metals. *Proc. Natl. Acad. Sci.* **2013,** *110* (25), 10084-10088; (b) Kanady, J. S.; Tsui, E. Y.; Day, M. W.; Agapie, T., A Synthetic Model of the Mn_3Ca Subsite of the Oxygen-Evolving Complex in Photosystem II. *Science* **2011,** *333*, 733-736; (c) Tsui, E. Y.; Agapie, T., Reduction potentials of heterometallic manganese–oxido cubane complexes modulated by redox-inactive metals. *Proc. Natl. Acad. Sci. U. S. A.* **2013,** *110* (25), 10084-10088.

Chapter 2

Cobalt-Catalyzed Monooxygenation of Benzene Activated by Non-innocent Ca^{2+} Countercations

With Christopher C. Scarborough, Christian M. Wallen, Bryant Chica, John Bacsa, Stephanie Daifuku, and Michael Neidig.

Partially published in Christopher C. Scarborough & Marika Wieliczko, 'Catalysis in the production of phenols from aromatics' US Patent No. WO2015142828, September 24 2015.

Partially published in C. M. Wallen, M. Wielizcko, J. Bacsa and C. C. Scarborough, "Heterotrimetallic sandwich complexes supported by sulfonamido ligands", *Inorg. Chem. Front.*, 2016, **3**, 142;
DOI: 10.1039/C5QI00233H. Adapted by permission of the Royal Society of Chemistry.

2.1 Introduction: Activation of Transition Metal Complexes by Redox-inactive Cations

2.1.1 Selective Monooxygenation of Aromatic Hydrocarbons

Direct oxidation of aromatic hydrocarbons, e.g. the oxygenation of benzene to phenol (PhOH), is challenging due to the necessity for a highly potent oxidant capable of activating aromatic C-H bonds and the resultant challenge in achieving selectivity that is both catalyst-controlled and averts over-oxidation of the more reactive product relative to substrate. Although direct benzene oxidation using hydrogen peroxide (H_2O_2) and solid-state molecular sieve catalysts has attracted a great deal of interest in recent decades, reflecting recognition of shortcomings of the multistep Hock (cumene) process, which is nonetheless employed in >90% of global phenol production, such heterogeneous systems are poorly understood and more thorough investigations of catalytically relevant species are needed to elucidate mechanisms and allow the systematic development of more effective catalysts.

In biological systems, direct and highly selective conversion of aromatics to phenols is catalyzed by CYP enzymes through 2-electron, oxo-transfer from the Fe^{IV}-oxo intermediate of CpdI to the ring *via* the NIH-shift mechanism.[40] However, in synthetic systems Fe species with H_2O_2 are typically associated with unselective, radical (Fenton) reactivity and have been shown to exhibit undesired over-oxidation. Molecular Ru and Fe complexes that are capable of catalyzing this conversion but exhibit rapid over-oxidation to quinones and subsequent deactivation.

Two means of accessing selectivity in hydrocarbon oxidation are through catalyst and kinetic control. Favoring 2-electron oxo-transfer processes over unselective 1-electron radical mechanisms would impart catalyst-controlled selectivity, and the kinetic suppression of over-oxidation could be achieved through incorporation of functional groups capable of deactivating PhOH for carbon-centered reactivity. The first element of a catalyst design would target a high-valent metal oxo of the late transition metals as the O-transfer species. Beyond manganese and iron, cobalt has shown capabilities for alkane hydroxylation[41] and for electrocatalytic[42] and light-driven, solution-phase water oxidation.[43] The efficacy of cobalt in effecting demanding oxidation reactions is exemplified by molecular and electrocatalytic water oxidation, and the cobalt complexes have been shown to react with oxygen sources to generate reactive species, namely when supported by anionic ligand fields and in the presence of secondary, redox inactive ions.

The synthesis and full characterization of a terminal cobalt-oxo complex is a challenge but also an important and pressing benchmark, especially if it is developed in a manner that is applicable to other metal-oxo complexes. It is evident that later metals provide a key element of instability that allows these energetically difficult reactions to take place. The origin of this instability and the scarcity of middle and late metal-oxo complexes is reasoned as a consequence of bond order and accessible oxidation state[44]. If metal-oxo stability is ascribed to multiple-bonding, then population of metal-oxygen antibonding orbitals is destabilizing up to a point beyond which oxo complexes are not attainable (the "oxo wall" origin).[45] This approach however, may underestimate electrophilicity, as the prevalence and reactive propensities of known oxos are not readily described as only functions of bond order.

If metal-oxo bond order is considered a parameter that is complemented by the electrophilic character of the oxo, which has a dramatic effect on reactivity, these factors must be considered together to develop a complete picture of a stable cobalt-oxo. Without considering the effects of geometry, a clear direction for coordination number and charge is established. As effective nuclear charge increases, ionization energy rises and approaches that of oxygen in moving across the transition series. As depicted in the qualitative molecular orbital diagrams shown in Figure 2.1, the energy gap between the metal and oxygen fragment orbitals decreases, and consequently the metal-oxo antibonding orbitals take on increasing oxygen character, i.e. the oxo becomes more electrophilic. If this outcome is to be countered, the energy of the d-orbital manifold must be maximized. This principle establishes the first criterion for an effective ligand design: both coordination number and anionicity of the ligand should be maximized to increase this energy gap and decrease oxo electrophilicity.

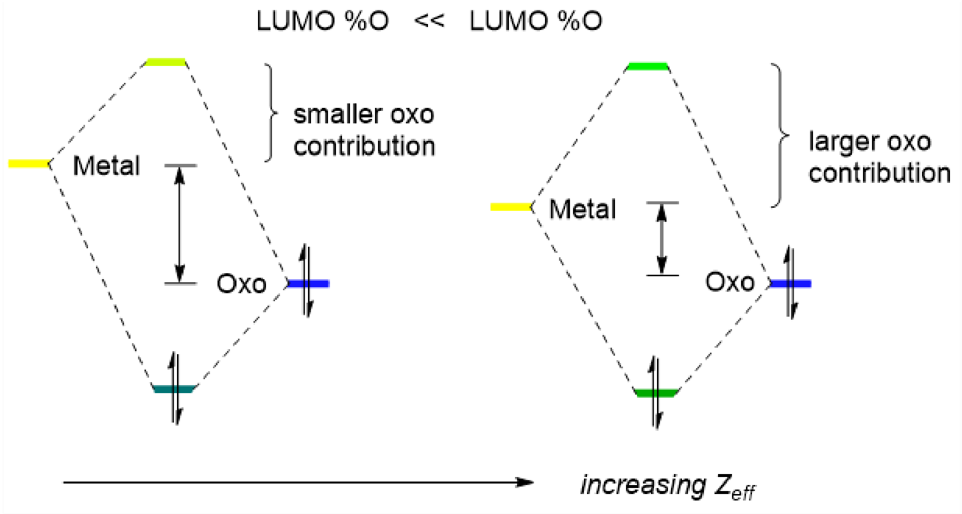

Figure 2.1 Qualitative MO diagrams depicting the effect of increasing group number on oxo character and electrophilicity

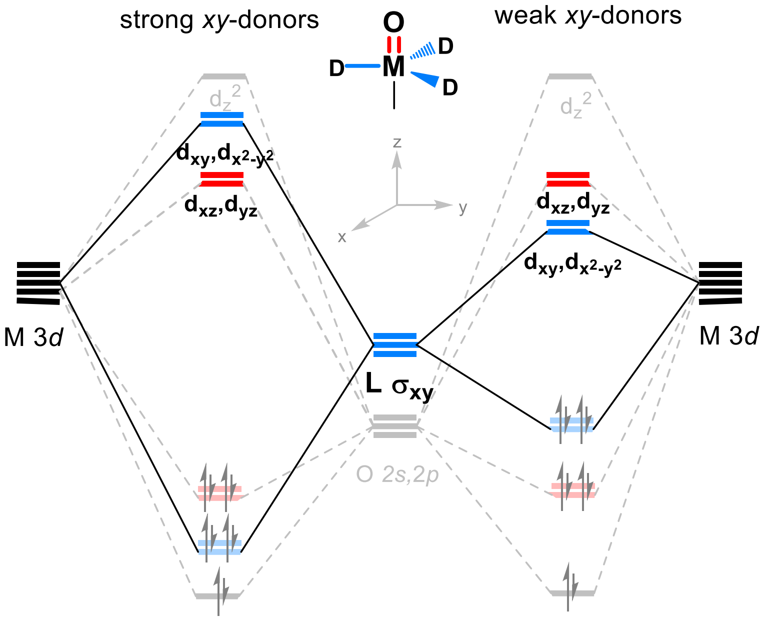

Figure 2.2 Qualitative MO diagrams depicting the ordering of MOs for weak and strong donor ligands in TBP geometry.

The nature of the metal-oxo can then be assessed by evaluating bond order, determined by the electron distribution between bonding, non-bonding and anti-bonding orbitals. Hence, *d*-electron count and coordination geometry largely determine the metal-oxo bond order. With the highest possible coordination number of six, as many as four electrons can be accommodated while maintaining a metal-oxo bond order of two or greater in octahedral geometry. A fifth electron, however, eliminates double bond character, and limited by accessible oxidation states, $\mathrm{Fe}^{\mathrm{IV}}$-oxo arises as the limit in octahedral geometry (the basis for the familiar "oxo wall"). Moving to coordination number five with TBP geometry yields two doubly degenerate *e* sets, one that is predominately sigma-antibonding in the *xy*-plane and one of *pi* symmetry that is metal-oxo antibonding in nature. The ordering of these two sets is highly dependent on their relative energies, as shown in Figure 5, but most literature depicts strong donor ligands, such that metal-oxo antibonding are to be filled first, eliminating TBP as a suitable geometry.[44]

If the weakly metal-ligand antibonding MOs are populated first, however, six *d*- electrons can be accommodated - this ordering is feasible *provided the donors are exceptionally weak*. This observation leads to the second criterion, that the ligand arms in the *xy*-plane be unusually weak sigma donors. Lastly, having considered electronic structure, other characteristics likely to be important for isolation and full characterization can be drawn from reports in the literature. Co-oxo complexes are expected to be reactive species, as transients have been shown to react with nearby alkyl substituents[46] and insert into carbene ligands,[47] and Fe-oxos are known to oxidize nearby mesityl ligands for example[48]. The third and final stipulation therefore, is the use of oxidatively stable functional groups that high solubility to allow reactivity studies to take place in inert solvents such as benzene.

2.1.2 Ligand Design for Accessing Mid- and Late-metal Oxo Species

A survey shows that for anionic ligands, stronger donor ligands tend to be preferred, such as Borovik's ureate system. Of known tripodal ligands, the sulfonamidates recently explored by Borovik[49] are the most acidic systems (pK_a ~ 16) , and as such, we may establish this system as a starting point for a spectrum of weak donor ligands with decreasing pKa (and likewise donor strength). With the target in an ideal case being case being an isolable Co^{IV}-oxo, this ligand system served as the first test of the validity of the presented argument that trianionic, tripodal, weakly donating ligands will stabilize an isolable cobalt-oxo. The introduction of divalent counterions proved to have a pronounced effect in several cases in activating reactivity of first row transition metal oxo species, most notably around the time these studies were began was the mesitylene derivative shown in Figure 2.1, where in the case on Mn(II), reduction of O_2 was greatly accelerated in the presence of Ca^{2+} to yield a Mn^{III}-hydroxo;[50] reaction with O-atom transfer agent iodosobenzene, PhIO, in dichloromethane (DCM) led to formation of a Co^{III} hydroxide.[49] This is strong evidence that a transient Co^{IV}-oxo species may precede this complex which occurs through one of many potential routes for H-atom abstraction to yield the final product. Notably, the mesitylene groups are expected to be especially susceptible.

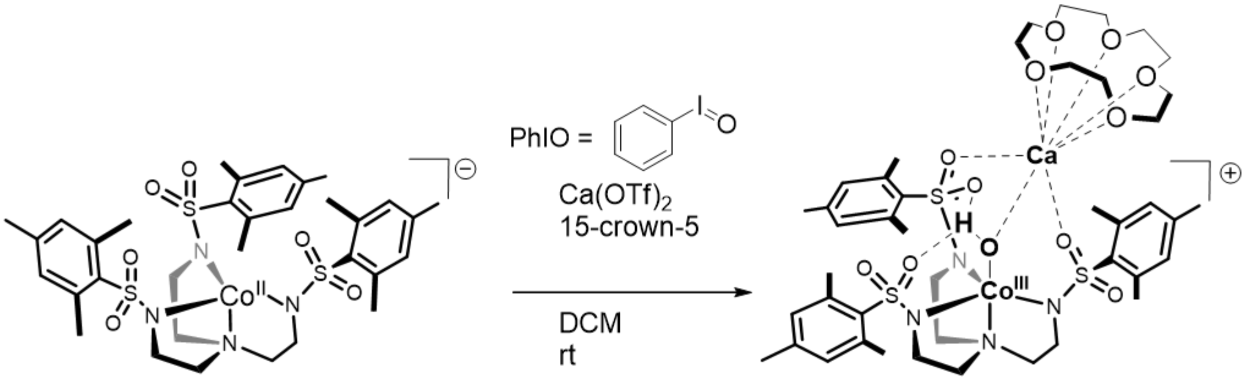

Figure 2.3 Reaction of the Borovik Co(II) system with PhIO in DCM to yield a Co(III) hydroxide.[49]

Isolable synthetic examples of Co terminal-oxo complexes are unknown and this is not surprising that middle and late first-row metal-oxo complexes are rare. A handful of crystallographically characterized Mn[51] have been reported and despite successful isolation of stable Fe complexes[52], are known and to date such Co^{IV}-oxo [53] and related imido[54] complexes are typically only observed transiently. Redox inactive metals such as Sc^{3+} were also shown to activate high-valent metal-oxo species, including Mn^{IV}-oxo [55] and transient Co^{IV}-oxo species, but recently a Sc^{3+}-stabilized Fe^{IV}-oxo was shown to be in fact Fe(III).[56]

Thus the reactivity of cobalt complexes bearing the trianionic sulfonamide Ts_3tren ligand (Ts_3tren = N,N',N''-(nitrilotris(ethane-2,1-diyl))tris(4-methylbenzenesulfonamide)) are ideal for studies of Co(IV) oxos and related species and where the anionic nature of the resultant Co(II) complexes allowed the incorporation of a counterion, both weakly interacting organic ammonium and phosphonium cations or group I and II cations K^+ and Ca^{2+}. By avoiding the mesityl derivative and opting for tosyl, the oxidatively susceptible groups are also discouraged from reaction by steric positioning away from the reaction center. In terms of kinetic suppression of overoxidation, a little-known but potentially valuable observation is that tetramethylene sulfone is known to interact strongly with PhOH and even modify its reactivity against carbon-based reactivity and over-oxidation. Kinetic suppression of PhOH may also be achieved by caging the reactive Co^{IV}-oxo site in an electron-rich pocket. Such caging could be improved by bridging two electron-rich environments with a redox-inert metal ion, which is likely to have the added benefit of electrostatically stabilizing the oxo ligand. These compounds were studied for the catalytic oxygenation of benzene to yield phenol with high selectivity using H_2O_2 as the O-source. A specific, non-innocent effect of Ca^{2+} was discovered which facilitates the formation of a reactive species that results in oxidation of the Co(II) which has been characterized by XRD, MS, EPR, IR, and UV-Vis spectroscopy. The possibility and likelihood of a transient Co^{IV}-oxo forming are discussed. These species are proposed as important catalytic components in the direct oxygenation of benzene to phenol using H_2O_2 for which this compound was found to be especially active with high selectivity.

2.2 Experimental

2.2.1 General Considerations

All reagents were purchased from commercial resources (Sigma Aldrich, Alfa Aesar or Strem Chemicals) and were used as received unless noted otherwise. Iodosobenzene was prepared according to the literature procedure.[57] All synthesis and manipulations of metal complexes for spectroscopy and characterization were carried out in an MBraun UNIlab 2000 inert-atmosphere glovebox maintained under nitrogen atmosphere. Anhydrous solvents were purchased from Sigma Aldrich (Sure/Seal™) and stored over 4Å molecular sieves for at least 24h before use. Molecular sieves (purchased from Sigma Aldrich) were activated by heating under vacuum in a sand bath to 250°C for 24 hours. ^{1}H-NMR, ^{13}C-NMR spectra were obtained on an INOVA (400MHz) instrument at 298K and referenced to residual solvent. Infrared spectra were obtained using a Nicolet 6700 FT-IR with Thermo Smart Orbit Diamond ATR attachment, using Paratone oil to coat samples to protect from ambient moisture and with a blank oil spectrum used as the background. Mass spectrometric measurements were performed by electrospray ionization (ESI) on a Thermo Finnigan LTQ-FTMS instrument. Elemental Analyses were obtained from Atlantic Microlab Inc., Norcross, Georgia. UV-Vis-NIR spectra were measured using a Shimadzu UV-3600 UV-Vis-NIR spectrophotometer equipped with D2 and WI source lamps and photomultiplier/PbS/InGaAs detectors using double beam measurement mode for simultaneous reference subtraction. Electron paramagnetic resonance spectroscopy (EPR) and magnetic circular dichroism (MCD) spectroscopic data were collected at the University of Rochester in Rochester, NY. Samples for EPR and MCD spectroscopy were prepared at Emory University and shipped to the University of Rochester in advance as well as on site for comparison. Calibration curves for quantification of phenol were prepared using the internal standard (ISTD) method with either tetradecane ($C_{14}H_{30}$) or nonane (C_9H_{20}) as noted with 3-5 unique standards which were analyzed in duplicate and averaged; when appropriate, calibration curves were regenerated to reflect scaling of reactions such that observed peak areas fell within a linear response range.

2.2.2 Ligand and Co(II) Complex Synthesis

The synthesis of the Co(II) complexes was reported as described herein,[58] were subsequently reported with modifications and extensions.[59] Presented below are examples of the original synthetic routes that were employed prior to the latter publication.

Synthesis of H_3Ts_3tren ligand. In a 1 L round bottom flask charged with a magnetic stirring bar, tosyl chloride (10.00 g, 0.05245 mol, 3.1 equiv) was dissolved in 100 mL of dichloromethane; the flask was sealed with a septum and purged with nitrogen and stirred in an ice bath. Following addition of 2.53 mL (0.0276 mol, 1.6 equiv) of triethylamine to the purged, chilled flask, 2.53 mL (0.0169 mol, 1 equiv) was added to the stirring solution dropwise *via* syringe over 30 minutes, forming a white precipitate. The reaction was allowed to warm to room temperature and stirred overnight. The following day, the mixture was concentrated under reduced pressure to afford an off-white residue, which was then stirred with approximately 500 mL of saturated aqueous sodium bicarbonate, and an off white solid formed. The solution was decanted and any solid material was collected on a Buchner funnel. The remaining solid and residue were again stirred with 500 mL of saturated aqueous sodium bicarbonate and the remainder of solid material was collected on the Buchner funnel. The off-white solid was washed large volumes of water, brine, and water and transferred to a 250 mL round bottom flask, and dried under vacuum overnight. The white solid was then washed with ether (100 mL, 3x) to remove excess unreacted tosyl chloride and again dried under vacuum overnight to afford 7.6048 g H_3Ts_3tren as a white solid (76.89%). ^{1}H-NMR, $CDCl_3$; δ(ppm) 2.638 (s, 3H), 2.690 (t, 2H), 3.107-3.148 (dd, 2H), 6.210 (t, 1H), 7.506 (d, 2H), 8.012 (d, 2H); ^{13}C-NMR, δ(ppm): 21.738, 41.016, 54.320, 127.395, 129.984, 136.978, 143.518.

Synthesis of Co(II) complex ***1***. In the glovebox, in a 100 mL Schlenk tube charged with a magnetic stirring bar, 2.0070 g (3.297 mmol, 1 eq.) of H_3Ts_3tren was combined with 427.2 mg of $CoCl_2$ (3.290 mmol, 1 eq.) and dissolved in 10 mL of DMF to afford a dark blue solution. To the solution, 231.7 mg (5.50 mmol, 1.7 eq.) CaH_2 was added in portions and a small amount of gas evolution was observed and the solution became darker in color. When gas evolution had ceased, the flask was removed from the glovebox and the stirring solution was heated to 80°C in a shallow oil bath, with periodic venting by rapid cycling of the side-arm stopcock to relieve pressure. Once substantial gas evolution at elevated temperature had ceased, the reaction was allowed to continue without venting overnight. The following day, the dark purple solution was concentrated under reduced pressure and the flask was returned to the glovebox. The residue was then dissolved in toluene (20 mL) to afford a purple solution and some pink precipitate. Approximately 1-2 mL of DMF was added until all the pink precipitate had dissolved. The solution was allowed to stand and colorless crystalline precipitate began to form. The purple solution was filtered and a small amount of diethyl ether was added, the solution was allowed to stand, and additional colorless precipitate that formed was filtered off. The remaining solution was layered under diethyl ether and a purple precipitate that formed over night was collected on a fine-porosity glass fritted funnel. The precipitate was redissolved in dichloromethane to afford a violet solution. Molecular sieves were added to the solution and upon standing overnight, X-ray quality blue-violet crystals of $Ca[Co(Ts_3tren)]_2$ (**1**) formed, leaving a clear, colorless solution. The crystals became pink in color and became unsuitable for X-ray crystal structure determination when exposed to ambient moisture. Elemental analyses were consistent with incorporation of four water molecules into the extant structure. Anal. Calcd for $C_{54}H_{74}CaCo2N_8O_{16}S_6$: C, 44.99; H, 5.17; N, 7.77. Found: C, 44.32; H, 5.20; O, 7.70. Crystal Data for $C_{54}H_{66}CaCo_2N_8O_{12}S_6$ (M =1369.44): monoclinic, space group $P2_1$ (no. 4), a = 13.9236(11) Å, b = 13.3642(10) Å, c = 17.2950(13) Å, β = 112.3550(10)°, V = 2976.3(4) $Å^3$, Z = 2, T = 109.01 K, μ(MoKα) = 0.921 mm^{-1}, $Dcalc$ = 1.528 g/mm^3, 22136 reflections measured ($3.162 \leq 2\Theta \leq 58.432$), 14778 unique ($R_{int}$ = 0.0328) which were used in all calculations. The final R_1 was 0.0476 (I > 2σ(I)) and wR_2 was 0.1149 (all data). ESI-MS, [M-], (m/z): calcd for ($CoTs_3tren^-$): 664.08942; Found: 664.09036 (Δ=1.4ppm); [M+] (m/z): calcd for (Ca^{2+})($CoTs_3tren^-$)(H_2O): 722.06258; Found: 722.06121 (Δ=-1.9ppm).

*Synthesis of Co(II) complex **2** $^{tBu}Ph_4P[Co^{II}(Ts_3tren)]$.* In the glovebox, **1** (549.3 mg, 0.90mmol) was dissolved in DMF (8mL). To this stirring solution, solid KH (118.0 mg, 2.94 mmol) was added in portions and the solution formed an off-white suspension. When gas evolution had ceased, $CoBr_2$(197.o mg, 0.90 mmol) was added. The suspension rapidly became clear and the initially blue solution became deep purple. $^{tBu}PPh_4Br$ was added (191.2 mg, 0.91 mmol). The reaction was allowed to stir overnight and then concentrated under reduced pressure and filtered over celite to remove KBr. Upon addition of a small amount of pentane, the complex precipitated from solution as a microcrystalline blue-purple solid, which after storing at -35C was collected on a medium porosity glass fritted funnel (557.2 mg, 78%). The aqua complex was generated by removing the solid from the glovebox, after which it quickly turned pink. Single crystals of both complexes were grown by vapor diffusion of pentane into THF. UV-Vis, MeCN: λ_{max} 535 nm , 411 nm, 690 nm. ESI-MS $[M]^-$ Exact mass calculated for $C_{27}H_{33}CoN_4O_6S_3$:664.08942, Found: 664.09023. Elemental analysis calculated for **2,** $C_{27}H_{35}CoN_4O_7S_3$**:** C:47.50 H:5.17 N: 8.21% Found: C:51.85 H:6.83 N: 8.51%.

2.2.3 Catalytic Oxygenation of Benzene

Catalysis experiments were carried out by preparing stock solutions of **1** in benzene. The poor solubility of **1** under strictly anhydrous conditions relative to hydrated environments rendered exact concentration calculations difficult; thus, the mass of **1** was either weighed in the glovebox under anhydrous conditions and combined with benzene outside the glovebox, wherein the dissolution was allowed to continue in the presence of moisture prior to catalysis experiments, or the molecular weight of 1441.53 g/mol incorporating 4 water molecules was assumed (consistent with elemental analysis).

Standards for phenol were prepared by dissolving known masses of the analyte, phenol and ISTD, tetradecane in 10 mL of benzene. The standard solutions were analyzed by 20.0 split ratio injection (1.0 μL volume) followed by gas chromatographic separation. A method for suitable chromatographic separation with efficient time profile was developed with parameters as follows: injection temperature: 300°C; detector temperature: 300°C; initial oven temperature of 80°C held for 2.00 minutes, 50°C/min ramp to 280°C, and a final hold of 280°C for 2.00 before cooling to 80°C at a rate of 50°C/min to 80°C. The peak areas of target analyte and ISTD were measured and fitted as shown in Table 2.1 through linear regression with a $1/C^2$ weighting scheme and without forcing a zero point for the analyte and ISTD. The obtained parameters through this method were as follows: function: f(x)=0.776129x-0.0269103; mean response factor(RF): 6.932032e-001; RF standard deviation(SD): 4.242677e-002. Rr1=0.9992282 Rr^2=0.9984570 RSS=8.125280e-004.

Table 2.1 Calibration curve generation for phenol with $C_{14}H_{30}$ ISTD

STD#	PhOH (mg)	$C_{14}H_{20}$ (mg)	Conc.(Ratio)	Mean Area Ratio
1	1.96	11.46	0.1710297	0.106668
2	3.99	11.21	0.3559322	0.245922
3	4.82	12.64	0.3813291	0.263814
4	6.08	13.42	0.4530551	0.323007
5	12.14	23.33	0.5203601	0.388516

Due to poor resolution of tetradecane and biphenyl under said conditions, the absence of biphenyl was verified both by using nonane as internal standard and by GC-MS.

The identities of compounds from benzene oxygenation catalysis experiments were confirmed by gas chromatography-mass spectrometry using a Hewlett Packard HP-5987 gas chromatograph coupled to electron ionization (EI) mass spectrometer. The injection volume used was typically 10-15 uL. Samples were manually injected using the air gap method. The mass spectra of constituent components were compared to published spectra obtained online through NIST Mass Spectrometry Data Center. The presence or absence of benzene oxygenation products not readily apparent in the chromatogram was assessed by selective ion searching for fragment ions characteristic of products reported in EI ionization.

2.2.4 EPR and Magnetic Circular Dichroism Spectroscopy

All samples for EPR spectroscopy were prepared in an inert atmosphere glove box equipped with a liquid nitrogen fill port to enable sample freezing to 77 K within the glove box. EPR samples were prepared in both THF and 1:1 (v:v) THF:2-MeTHF to form low temperature optical glasses. EPR spectra were collected using a Brüker EMXplus EPR spectrometer with liquid helium cooling to 10K and analyzed using the Bruker Xenon software suite. All samples for MCD spectroscopy were prepared in an inert atmosphere glove box equipped with a liquid nitrogen fill port to enable sample freezing to 77 K within the glove box. MCD samples were prepared in 1:1 (v:v) THF:2-MeTHF (to form low temperature optical glasses) in copper cells fitted with quartz disks and a 2 mm gasket. Low temperature MCD experiments were conducted using two Jasco spectropolarimeters. Both instruments utilize a modified sample compartment incorporating focusing optics and an Oxford Instruments SM4000-7T superconducting magnet/cryostat. This set-up permits measurements from 1.6 K to 290 K with magnetic fields up to 7 T. A calibrated Cernox sensor directly inserted in the copper sample holder is used to measure the temperature at the sample to 0.001 K. UV-visible MCD spectra were collected using a Jasco J-715 spectropolarimeter and a shielded S-20 photomultiplier tube. Near-infrared (NIR) data were collected with a Jasco J-730 spectropolarimeter and a liquid nitrogen cooled InSb detector. All MCD spectra were baseline-corrected against zero-field scans.

2.2.5 Resonance Raman Spectroscopy

In the glovebox, 70 mg of **1** was combined with 1 mL of THF in a 20 mL scintillation, affording a pale violet solution with the majority of the solid remaining undissolved. *tert*-Butylhydroperoxide (TBHP) (~5.5M in decane) was slowly added dropwise to the stirring solution. The solution instantly became intensely deep green in color and some gas evolution was observed; the dropwise addition was continued until gas evolution had ceased and undissolved violet solid was no longer apparent, affording an intensely dark green solution. The mixture was allowed to continue stirring at room temperature. Meanwhile, a small volume (2-3 drops) of the dark solution was removed from the solution and diluted in 3 mL of THF and its UV-Vis absorption spectrum was measured to verify completion of the reaction. Subsequent measurement of the spectrum did not show significant changes after 5 minutes and the solution was exposed to 530 nm LED light at maximum power of 980mA for 30 minutes and the spectrum re-measured. The reaction was effectively terminated 20 minutes from initiation by flooding of the bulk solution with pentane, immediately yielding a fine green precipitate. The precipitate was allowed to settle from the solution, and was separated from the faintly colored supernatant by collection over a fine-porosity glass fritted funnel and washed three times with pentane (2 mL) and briefly held under reduced pressure to remove residual solvent. The fine green powder was collected into a borosilicate glass NMR tube. Within 30 minutes, the tube was irradiated with 514 nm or 633 nm laser radiation and the Raman absorption spectrum was measured.

2.2.6 X-ray Crystallography

Single crystals of **1**-**O** were grown by layering of pentane onto a THF solution of **1**-**O** prepared from urea-H_2O_2 following filtration of urea. Dark green, nearly black crystals formed over several days upon standing with 4Å molecular sieves (on the solid surface of the molecular sieves). The crystals were porotected from moisture at all times and a suitable crystal was selected, mounted in Paratone oil and immediately mounted on a Bruker APEX-II diffractometer with CCD area detector. Data was collected using MoKα radiation (λ = 0.71073 Å) and the crystal was maintained at 100(2) K during data collection with an Oxford Cryosystems Cryostream 700 liquid nitrogen controller. Using Olex2[60], the structure was solved with the XT [61] structure solution program using Intrinsic Phasing and refined with the XL[62] refinement package using Least Squares minimization.

2.3 Results and Discussion

2.3.1 Synthesis of Co(II) Complexes

The preparation of the dimeric Ca[Co(Ts_3tren)$_2$] complex, denoted as **1**, was achieved in a facile manner using CaH_2 as a base in organic media. The mixture of Co(II) and ligand likely leads to coordination of cobalt that increases the acidity of the sulfonamide ligand, accounting for the observation that the ligand deprotonation reaction proceeds much faster if Co(II) is present. Otherwise the deprotonated ligand is extremely insoluble in solvents such as DMF and THF. The complex crystallizes as a dimer due to the monoanionic charge of the $[Co(Ts_3tren)]^-$ moiety, as shown in Figure 2.4. The complex **2** is a monomer and features a non-interacting bulky counterion. This complex was prepared using KH as the base with subsequent addition of the counteraction as it's bromide salt and removal of KOAc or KCl.

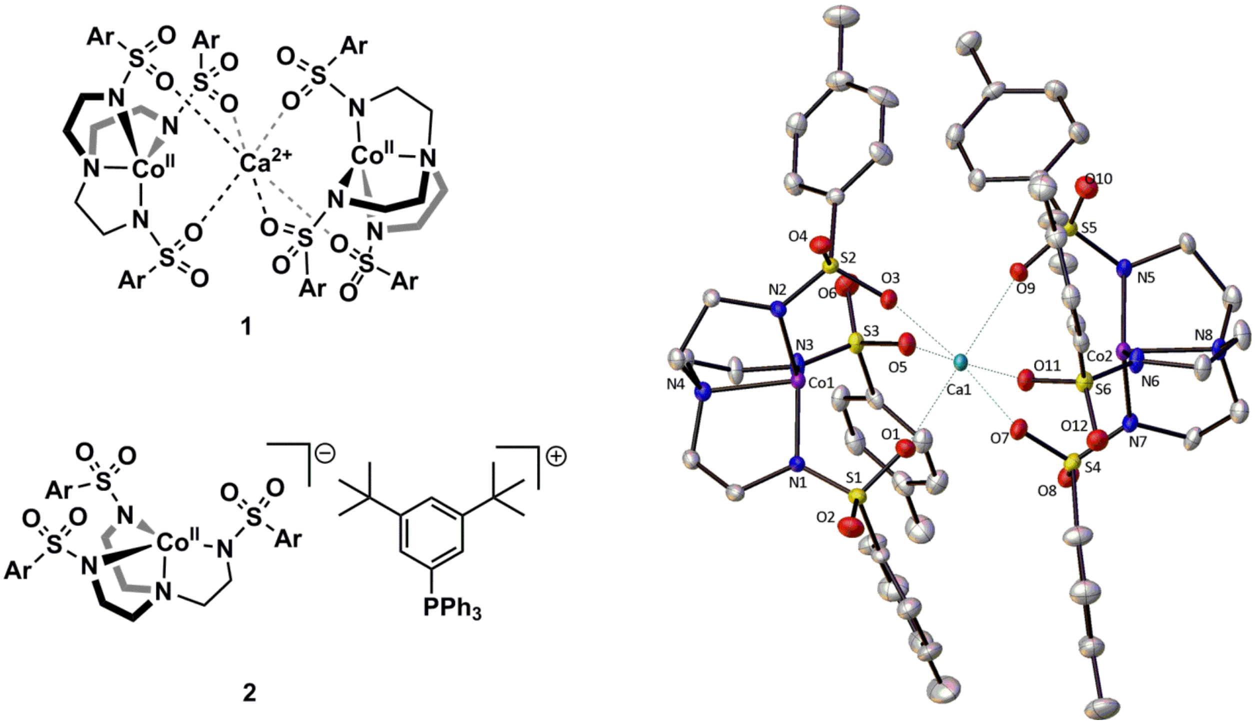

Figure 2.4 Schematic drawings of complex 1 and 2 and the X-ray crystal structure of 1. Hydrogen atoms are omitted for clarity. Thermal ellipsoids are shown at the 50% probability level. Carbon atoms shown in grey, nitrogen in blue, oxygen in red and sulfur in yellow.

2.3.2 Reactivity of Complexes towards Oxygen Atom Transfer Agents

A variety of O-atoms transfer agents were explored to probe means of forming a Co^{IV}-oxo species. Initial investigations showed no sign of reaction with mild reagents such as *N*-

methylmorpholine *N*-oxide. The use of a hypervalent iodine reagent, iodosobenzene (PhIO), however, yielded more promising results, but the choice of solvent and counterion played a significant part in the observed reactivity. As shown in Figure 2.4, addition of one equivalent of PhIO to solutions of **2** which features a bulky, non-interacting arylphosphonium counteraction in the absence of Ca^{2+} in THF or THF/MeOH results in no apparent reaction. In benzonitrile, however, a color change from deep purple to dark red-brown was observed (shown in Figure 2.5 in red). This spectrum is consistent with a Co^{III}-aqua species but could not be isolated. In the presence of K^+ ions in various solvents, reaction with PhIO or peroxides results in a rapid color change to dark brown and this species decayed to a new red-orange species over time, particularly in the presence of toluene and ether solvents, and also could not be isolated long enough to fully characterize. This species is most likely a Co^{III}-OH species, which is known to decompose to the Co^{II}-OH_2.[49] In stark contrast, upon addition of two equivalents of iodosobenzene, PhIO, solutions of **1** which feature Ca^{2+} counterions rapidly became intensely deep forest green (Figure 2.5). The reaction is accompanied with changes in the UV-Vis spectrum, which shows a dramatic rise of a strong band centered near 425 nm and a near-IR band centered near 708 nm. This intense color fades as the species decays with approximately first-order kinetics, showing a half-life of approximately four days in benzonitrile (Figure 2.7). Addition of a single equivalent to the dimeric complex showed incomplete conversion by UV-Vis, suggesting two oxygen atoms are transferred. Furthermore, in agreement with this observation, GC confirmed the formation of 2 equivalents of iodobenzene upon reaction with 2 equivalents of PhIO.

An identical absorption spectrum resulted upon addition of *tert*-butylhydroperoxide (TBHP) (Figure 2.5, inset). Reaction with TBHP is rapid and the intense green species quickly begins to lose intensity, but this is deferred if the cobalt complex is precipitated from the reaction solution and washed with pentane, suggesting the new species continues to react either with the reagent or with by-products of the reaction, presumably *tert*-butanol.

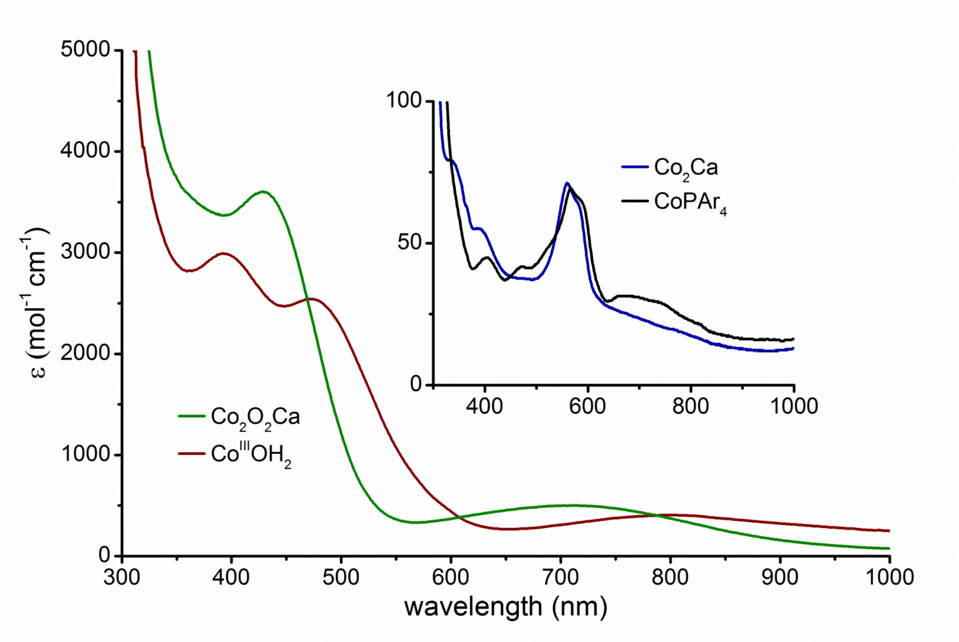

Figure 2.5 Comparison of UV-Vis spectra of complex 1 and 2 and the products of reaction with PhIO in benzonitrile. The product from complex 2 matches the spectrum of Co^{III}-aqua complex.[49]

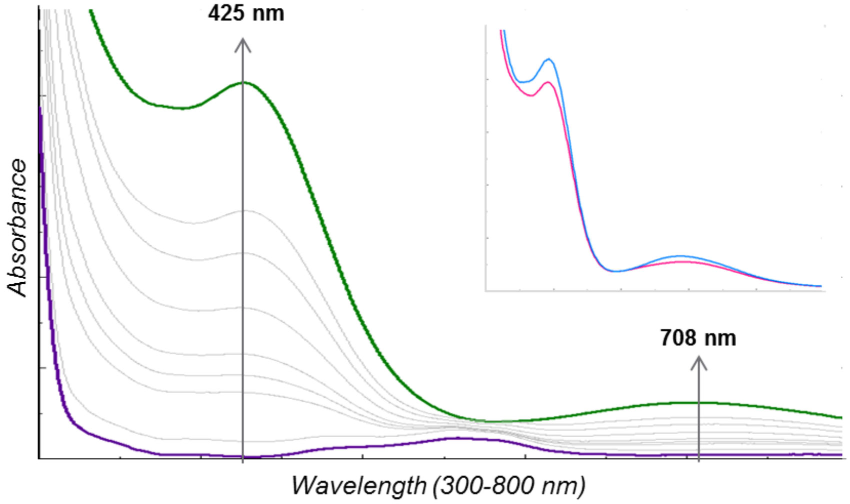

Figure 2.6 Reaction of ~0.5 mM 1 (purple) with 2 equivalents PhIO to form 1-O in benzonitrile. The inset shows a comparison of 1-O formed from TBHP (blue) and PhIO (pink).

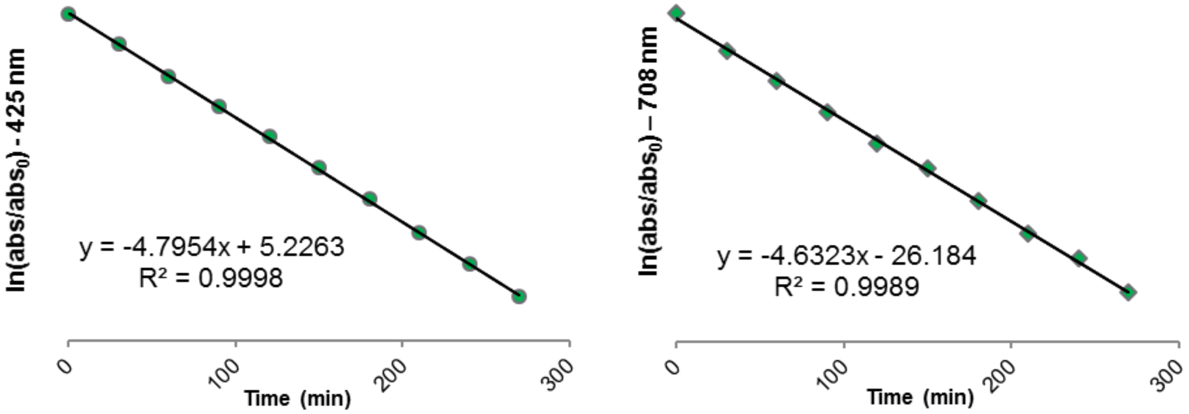

Figure 2.7 Linear fit of the decay of absorbance bands associated with decomposition of 1-O formed from reaction of 1 with PhIO.

The stability of **1-O** was evaluated in a variety of solvents as illustrated in Figure 2.5. There was no correlation between bond dissociation energies and the half-life, suggesting H-atom abstraction was not the preferred route of decomposition as **1-O** decays to **1-**OH_2. The longest half-like observed was for THF, giving 270 hours as shown in Table 2.2.

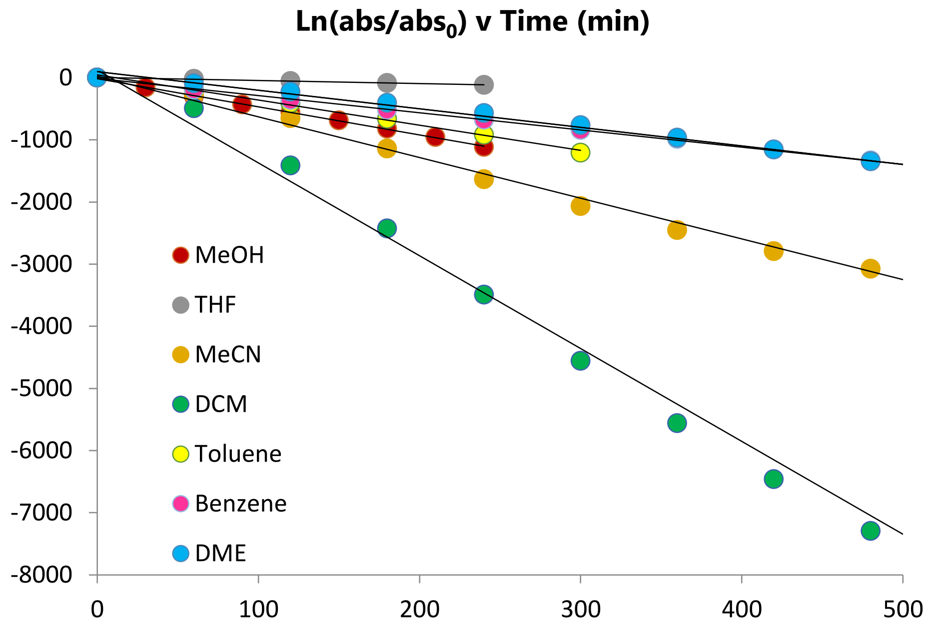

Figure 2.8 Comparison of half-life of 1-O formed from PhIO in various solvents. The longest $T_{1/2}$ *observed for THF was ~10 days.*

This suggested that this would be the ideal solvent for isolation of **1-O** in the solid state, and thus THF was explored as crystallization solvent in efforts to structurally characterize the unstable **1-O** prior to regeneration of **1**. As shown in Figure 2.5, in the absence of K^+ or Ca^{2+} ions, no reaction of the $[Co^{II}(Ts_3tren)]^-$ anion was observed with PhIO or peroxides. However both UV-Vis and GC suggest the transfer of two O atoms is possible to the dimeric complex. The presence of this species, **1-**O_2 cannot be distinguished from **1-O** and is likely to exist in equilibrium with the singly oxygenated species **1-O.**

2.3.3 Characterization of **1-O**

As described above, the instability of **1-O** rendered it extremely difficult to isolate as a single crystal suitable for structure determination. The PhIO and TBHP oxidants were abandoned due to the difficulty of purification of by-poroducts before decomposition. In the case of aqueous H_2O_2, rapid disproportionation and the presence of excess water led to incomplete formation of **1-O** and rapid reformation of **1**. Rather urea-H_2O_2, as a solid source of H_2O_2 proved to be ideal because the urea could be easily filtered away. As summarized in Table 2.2, the half-life of **1-O** was measured in a variety of solvents. Having identified THF as the ideal solvent for isolation of **1-O** due to the long half-life of 270 h in this solvent, a variety of conditions were employed using THF. In all cases crystals visibly decomposed upon exposure to moisture within seconds. In order to structurally characterize **1-O**, a solution of **1** was allowed to react with an excess of urea-H_2O_2 in THF for ~ 5 minutes until visible bubbling ceased. The urea was filtered off and activated 4Å molecular sieves were added before pentane was carefully layered over the solution. X-ray crystal structure determination of crystals obtained from reactions aimed at producing **1-O** revealed an unexpected oxygen atom in the ligand environment which is also coordinated to both Co and Ca^{2+} in ~20% occupation. It was later determined that this complex is most likely a small amount of Co^{III}-OH which forms with O-atom transfer and H-atom abstraction, presumably from adventitious solvent. Interestingly the Co^{III} species is not observed in the absence of Ca^{2+}, suggesting that the ion changes the mechanistic pathway for formation of the Co^{II}-OH_2 final product.

Table 2.2 Half-life of 1-O generated from urea-H_2O_2 in various solvents and C-H bond dissociation energies.

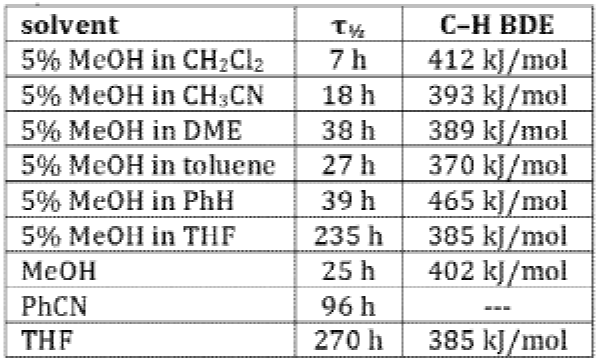

solvent	$\tau_{½}$	C–H BDE
5% MeOH in CH_2Cl_2	7 h	412 kJ/mol
5% MeOH in CH_3CN	18 h	393 kJ/mol
5% MeOH in DME	38 h	389 kJ/mol
5% MeOH in toluene	27 h	370 kJ/mol
5% MeOH in PhH	39 h	465 kJ/mol
5% MeOH in THF	235 h	385 kJ/mol
MeOH	25 h	402 kJ/mol
PhCN	96 h	---
THF	270 h	385 kJ/mol

Although the isolable product is Co^{III}-OH, a non-isolable intermediate may exist prior to H-atom abstraction. Various methods were explored in efforts to determine if the Co^{III}-OH species forms via a Co^{IV}-oxo species. The IR spectrum of the oxidized cobalt species, **1-O** is remarkably unchanged in comparison to that of the precursor **1** as shown in Figure 2.11. The vibrational spectrum of **1-O** shows a slight increase in the Co-N frequencies (~2 cm^{-1}) but the most apparent change is in the position of the N-S stretch that occurs at 922 cm^{-1}, which shifts to 933 cm^{-1}**.** Also shown in the spectrum is the absence of a prominent O-H stretching vibration as was reported for the related bridging hydroxo complex[64]. This suggests the Co^{III}-OH stretching band is broadened by coordination to calcium, and upon decomposition to Co^{II}-OH_2 the band becomes more prominent. Neither additional bands for the new Ca-O interaction, such as bands between 578 – 606 cm^{-1} that are characteristic of the Ca-O stretching mode in $Ca(OH)_2$, nor bands suggesting ligand decomposition are observed. The CH_2 bending modes associated with the ethylene bridge of the ligand remain unchanged and no alkene vibrations are observed.

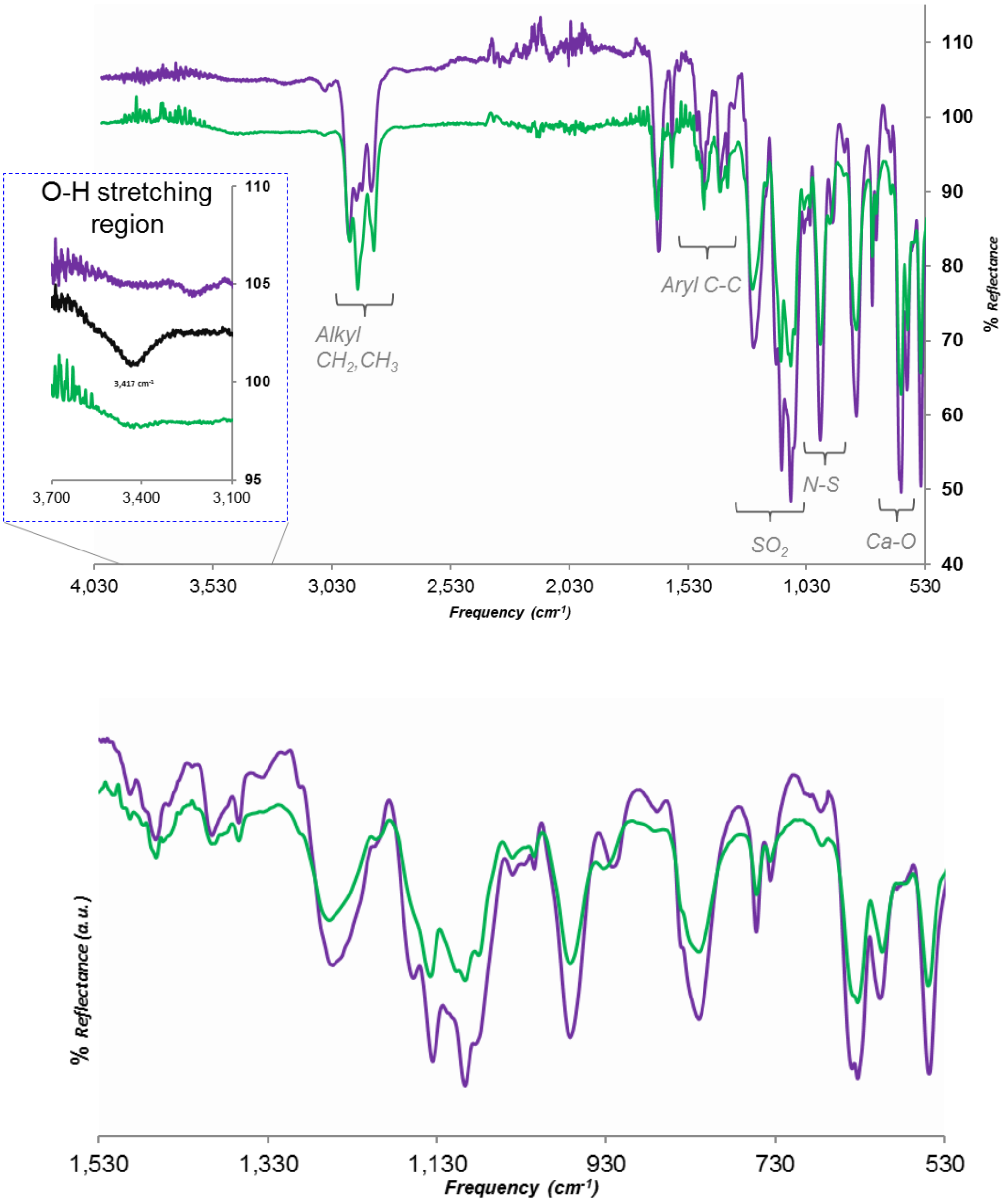

Figure 2.9 Comparison of the IR spectra of 1 (purple) and 1-O (green). Full spectrum (top) with inset showing O-H band that appears over extended periods and zoom of the fingerprint region (bottom).

The reaction of **1-O** with the electron donor dihydroanthracene (DHA) results in formation of anthracene as evidenced by UV-Vis spectroscopy as shown in Figure 2.10, along with concomitant formation of **1-H_2O**. The result agrees with the observation that the Borovik group's Co^{III}-OH is capable of H-atom abstraction to form the final product **1-H_2O.** The formation of the hydroxo was observed in only one Co of the dimeric complex by XRD. However since UV-Vis and GC both suggested that 2 equivalents per dimer can be transferred, it is possible that the species in solution is a dimeric form, **1-O_2** but that this decomposes (possibly through interaction with other **1-O_2** species) and is not isolable in the crystalline solid state, and only **1-O** is observed.

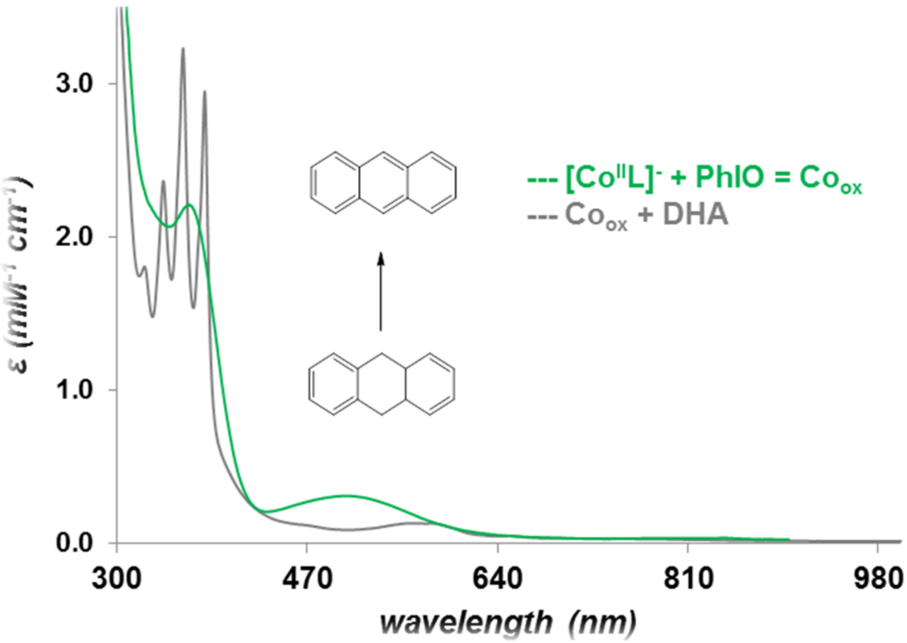

Figure 2.10 Reaction of 1 equivalent of 1-O generated from PhIO with DHA yields 1 equivalent of anthracene per Co(II) and regenerates 1.

The negative mode electrospray ionization (ESI) mass spectrum (MS) of **1-O** showed both the starting compound **1** and a signal for **1** + the mass of O atom with the Δ of 0.47 ppm for H_2O_2 and 0.71 PhIO is in excellent agreement with that calculated for m/z for [CoTST]+O = 680.08434, strongly suggesting this is the signal for the **1-O** anion. The intensity of the spectrum was dependent on the time, and was no longer observable as **1-O** decayed by UV-Vis, consistent with the observation that only **1** is re-isolated and no signs of incorporation into the ligand (*via* the benzylic tosyl group for example) were detected. These inconclusive MS results presented the interesting question of whether the oxygenated signal that is observed in the absence of Ca^{2+} ion is still a Co^{II} center with oxygen incorporation into the ligand or a transient Co^{IV}-oxo, which would have the same mass and charge. The difference cannot be distinguished by mass spectrometry. Thus, a more suitable technique for determining the electronic structure of **1-O** was explored, namely electronic paramagnetic resonance (EPR) spectroscopy. The spectrum of **1** in frozen THF solution shows an interesting 9:1 mixture of two species. The nature of these is not entirely clear, but may be related to aqua coordination or fluxionality in solution that reveals two coordination structures at cryogenic temperature. The spectrum of **1-O** shows only one signal, which accounts for ~90% of the integration of the **1** signal and is indistinguishable from the majority signal of **1** (Figure 2.11). This suggests the majority species present remains in the Co(II) state. The alternative conclusion would be that the Co(II) and Co(IV) species have identical parameters which does not seem likely.

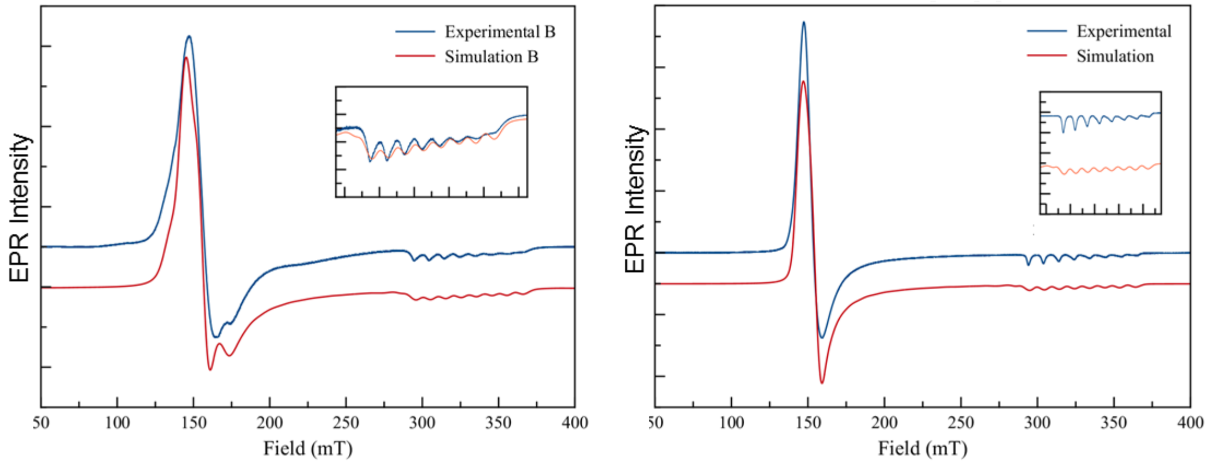

Figure 2.11EPR spectrum and simulation of frozen THF solution (4 K) of 1, left; Simulation 65% gx=gy= 4.45, gz= 2.02 (Az = 9.7 x 10-3Hz) and 35% gx= 4.95, gy= 3.95, gz= 2.02 (Az = 9.5 x 10-3 Hz), (1-O, right) EPR spectrum of 2 after reaction with excess H2O2 in THF, Simulation 100% gx=gy= 4.45, gz= 2.03 (Az = 9.5 x 10-3Hz)

The nature of the Co-O bond in **1-O** was further probed by resonance Raman (rR) spectroscopy as shown in Figure 2.12. Excitation with both 514 and 633 nm radiation produced a very weak signal at 797 cm^{-1}. The absorbance is relatively weak for **1-O** at this excitation wavelength and so the lack of enhancement is not entirely surprising. At 514 nm excitation, an additional band is observed at 1594 cm^{-1}. The 514 nm excitation wavelength is in a weaker tailing region of the intense λ_{max} at 425 nm of **1-O**. The presence of these two bands is very similar to the ν_{F-O} pair at 798 cm^{-1} band + 1598 cm^{-1} overtone observed in the rR spectrum of the Fe^{V}-oxo supported by tetramethylcyclam (TMC) ligand with an oxygenated *trans*-MeCN, [Fe^{V}(O)(TMC)NC(O)CH$_3$]$^{+}$.[65]

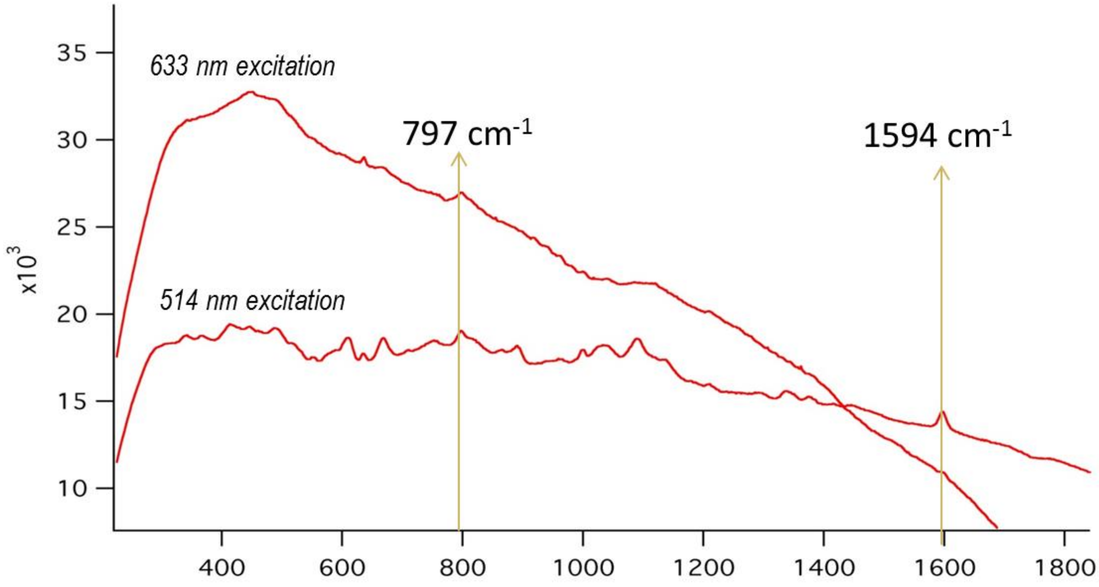

Figure 2.12 Resonance Raman spectra of 1-O generated from TBHP at 514 nm and 633 nm excitation.

Despite efforts to improve the resolution of the rR spectrum, the signal was not reproducible in the same sample over several exposures to the excitation laser. In order to examine whether the complex may be photosensitive, **1-O** was exposed to high intensity (900 mA) LED light at 455 nm and it's spectrum measured. As shown in Figure 2.13, the intensity of the 425 nm and 708 nm bands increases with light exposure up to a maximum after 5 hours. Subsequently, the signal decays into that of **1** over 48 hours. This suggests that the high intensity laser of excitation leads to rapid decomposition of **1-O**; thus, further rR studies may require low temperatures. It is not clear if the excitation involves formation of a Co^{IV}-oxo and the possibility of this transient species forming cannot entirely be excluded.

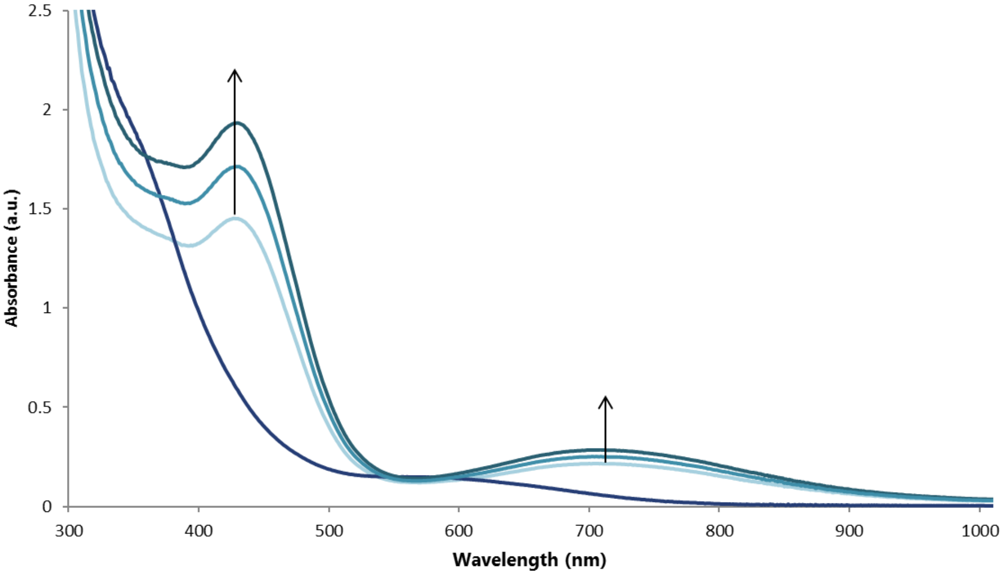

Figure 2.13 UV-Vis spectrum of 1 + $^{t}BuO_2H$ in THF to form 1-O (light blue) with exposure to 455 nm LED (900 mA) over 5 h (medium and dark blue lines) and final product after 48 h (purple).

2.3.4 Preliminary Reactivity Studies for Catalytic Monooxygenation of Benzene

The possibility of a transient Co^{IV}-oxo suggested that the compound may be active for oxygenation reactions and preliminary studies were conducted to probe its utility in the catalytic oxidation of benzene. Heating **1** in benzene in the presence of urea-H_2O_2 or aqueous H_2O_2 showed clean formation of PhOH; however, disproportionation of H_2O_2 was evident from the vigorous bubbling observed. Nonetheless, PhOH was formed as the sole detectable product based on gas chromatography (GC). The undesired over-oxidation products *ortho*-quinone, 1,4-benzoquinone, biphenyl, hydroquinone, catechol, maleic anhydride, maleic acid, and trihydroxybenzene were undetectable by GC-MS. The yield of PhOH revealed that the cobalt species was catalytically active, providing 10 turnovers in the initial test, but yield of PhOH based on H_2O_2 was only 0.4% because of the competitive disproportionation. Conditions were improved by altering the catalyst and H_2O_2 concentration and the temperature to achieve a maximum of 27,000 turnovers in 72 hours, with PhOH as the sole detectable product (Figure 2.14). This selectivity for oxidation of benzene to phenol was encouraging. Addition of 100,000 equivalents of phenol based on catalyst at the start of the reaction resulted in continued formation of phenol without concomitant formation of phenol oxidation products, showcasing an unprecedented selectivity against over-oxidation (Figure 2.15, top). In contrast, simple Co(II) salts exhibit rapid overoxidation in only 4 hours (Figure 2.15 bottom, red) compared to negligible oxidation of PhOH in a 24 hour period for **1**. The lack of over-oxidation may be attributable to interaction of the sulfonamide ligand with PhOH which would effectively hinder further reaction. Although overoxidation does occur over longer periods of time due to uncatalyzed reactions, these results suggest that **1** is capable of suppressing these side reactions, possibly via the competitive disproportionation which may eliminate some of the reactive species in solution.

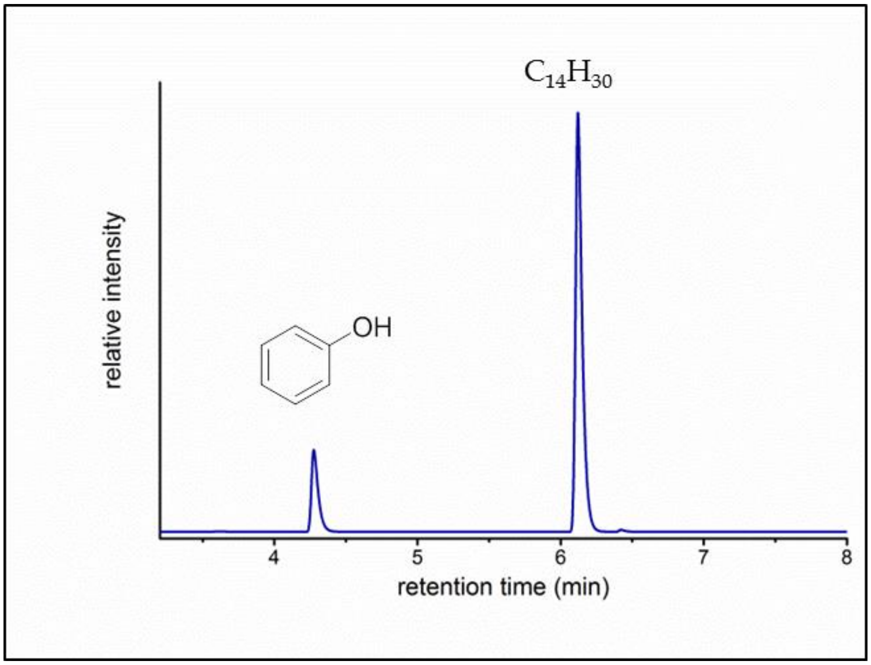

Figure 2.14 Phenol detected by GC from catalytic monooxygenation of benzene with H_2O_2.

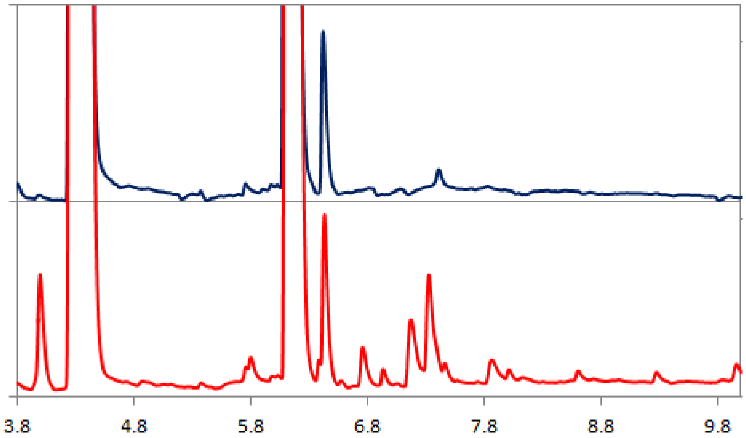

Figure 2.15 Overoxidation of phenol from $CoCl_2$ detected by GC. Reaction conditions: 0.006µmol catalyst (Co atom), 80°C, 10mL benzene, 1mmol H_2O_2. Catalyst 1 after 24 h (top, blue) and $CoCl_2$ after 4 hours (bottom, red).

Although **1** exhibits excellent catalytic properties in the selective monooxygenation of benzene to PhOH using H_2O_2, the system suffers from several deficiencies: (a) low yield based on H_2O_2 due to competitive disproportionation (b) inhibition of the reaction below temperatures of 80° C due to H_2O coordination at Co that is unavoidable due to H_2O formation from deficiency (a) as noted and (c) catalyst deactivation over time. Unlikely is it that this deactivation occurs to ligand degradation or hydrolysis of the anion, but rather due to urea buildup as shown in Figure 2.16. This product is isolated from reactions of **1** with urea-H_2O_2 in attempts to isolate **1-O.** The strong coordination of urea to the Ca^{2+} ions most likely prevents the interaction required to form the reactive intermediate, instead resulting in mainly H_2O_2 disproportionation.

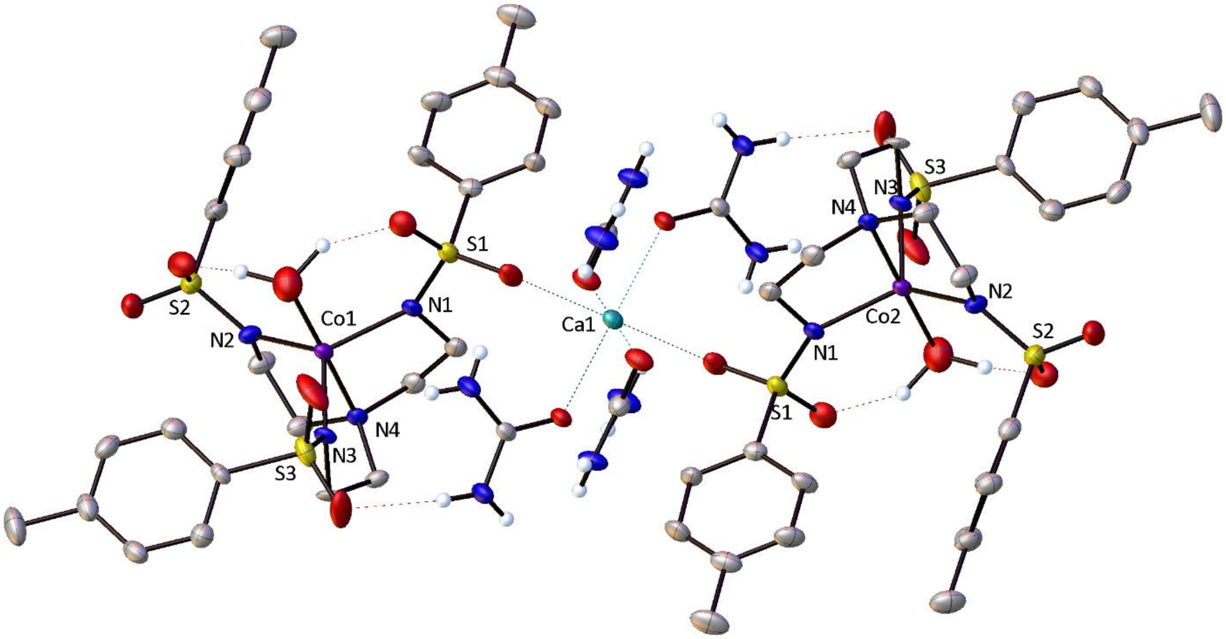

Figure 2.16 Crystal structure of 1-urea adduct isolated from urea-H_2O_2 solutions of 1 in attempts to isolate 1-O.

2.4 Conclusions

The prevalence of transition metal terminal-oxos in selective oxygenation reactions in Nature suggests that artificial counterparts may serve as valuable catalysts and biological models. Cobalt complexes bearing trianionic, tripodal sulfonamide ligand scaffolds were targeted due to the molecular orbital theory arguments suggesting this geometry and electronic environment would be amenable for supporting late-metal terminal-oxo complexes. The secondary sphere binding ability of the sulfonamide in the Ts_3tren ligand scaffold proved ideal for exploring the effects of strongly-interacting alkali cations K^+ an Ca^{2+} in the reactions of Co(II) complexes with O-atom transfer agents. Although spectroscopic evidence suggests the ligand scaffold may be promising, the specific effect of Ca^{2+} cations on oxygenation of the ligand scaffold is of particular interest. The Ca^{2+} ion appears to activate oxidation of Co(II), while MS and rR studies suggest formation of a transient Co^{IV}-oxo. EPR studies corroborate the presence of a majority Co(II) species in **1** but the disappearance of the ~10% secondary species is difficult to interpret. The spectrum after reaction is not consistent with any of the known coordination modes in this scaffold. The Co(III) species would be expected to be EPR silent so it is possible that the **1-O** signal is extremely similar to that of **1** with only a portion of Co(III) species captured in the frozen THF solution before reformation of the Co(II). More EPR studies would be valuable, as would magnetic circular dichroism (MCD) studies. These were explored but suffered difficulties in sample preparation due to water from H_2O_2 disproportionation.

This complex proved to be catalytic active with high selectivity in the monooxygenation of benzene to yield PhOH using H_2O_2, although low yields based on H_2O_2 and catalyst deactivation remain as barriers to further application of this catalytic system. Ultimately a stable Co^{IV}-oxo was not isolated in the solid state, although the significant effects of the redox-inert cation Ca^{2+} were revealed to have a specific effect in generating the reactive species. In the following chapters, the studies of redox-inactive cations are extended to the artificial catalytic oxidation of water to yield dioxygen.

2.6 References

1. Ortiz de Montellano, P. R., *Cytochrome P450: Structures, Mechanism and Biochemistry*. 2nd ed.; Plenum Press: New York, 1995.

2. Nam, W.; Kim, I.; Kim, Y.; Kim, C., Biomimetic alkane hydroxylation by cobalt() porphyrin complex and -chloroperbenzoic acid. *Chemical Communications* **2001,** (14), 1262-1263.

3. (a) Kanan, M. W.; Nocera, D. G., In Situ Formation of an Oxygen-Evolving Catalyst in Neutral Water Containing Phosphate and Co2+. *Science* **2008,** *321* (5892), 1072-1075; (b) Nocera, D. G., The Artificial Leaf. *Accounts of Chemical Research* **2012,** *45* (5), 767-776; (c) Betley, T. A.; Surendranath, Y.; Childress, M. V.; Alliger, G. E.; Fu, R.; Cummins, C. C.; Nocera, D. G., A ligand field chemistry of oxygen generation by the oxygen-evolving complex and synthetic active sites. *Philosophical Transactions of the Royal Society B: Biological Sciences* **2008,** *363* (1494), 1293-1303.

4. Yin, Q.; Tan, J. M.; Besson, C.; Geletii, Y. V.; Musaev, D. G.; Kuznetsov, A. E.; Luo, Z.; Hardcastle, K. I.; Hill, C. L., A Fast Soluble Carbon-Free Molecular Water Oxidation Catalyst Based on Abundant Metals. *Science* **2010,** *328* (5976), 342-345.

5. Saouma, C. T.; Peters, J. C., ME and ME complexes of iron and cobalt that emphasize three-fold symmetry. *Coordination Chemistry Reviews* **2011,** *255* (7–8), 920-937.

6. Winkler, J. R.; Gray, H. B., Electronic structures of oxo-metal ions. *Struct. Bonding (Berlin, Ger.)* **2012,** *142* (Copyright (C) 2012 American Chemical Society (ACS). All Rights Reserved.), 17-28.

7. Egan, J. W.; Haggerty, B. S.; Rheingold, A. L.; Sendlinger, S. C.; Theopold, K. H., Crystal structure of a side-on superoxo complex of cobalt and hydrogen abstraction by a reactive terminal oxo ligand. *Journal of the American Chemical Society* **1990,** *112* (6), 2445-2446.

8. Hu, X.; Meyer, K., Terminal Cobalt(III) Imido Complexes Supported by Tris(Carbene) Ligands: Imido Insertion into the Cobalt−Carbene Bond. *Journal of the American Chemical Society* **2004,** *126* (50), 16322-16323.

9. Bigi, J. P.; Harman, W. H.; Lassalle-Kaiser, B.; Robles, D. M.; Stich, T. A.; Yano, J.; Britt, R. D.; Chang, C. J., A High-Spin Iron(IV)–Oxo Complex Supported by a Trigonal Nonheme Pyrrolide Platform. *Journal of the American Chemical Society* **2012,** *134* (3), 1536-1542.

10. Lacy, D. C.; Park, Y. J.; Ziller, J. W.; Yano, J.; Borovik, A. S., Assembly and Properties of Heterobimetallic Co(II/III)/Ca(II) Complexes with Aquo and Hydroxo Ligands. *J. Am. Chem. Soc.* **2012,** *134* (42), 17526-17535.

11. Park, Y. J.; Ziller, J. W.; Borovik, A. S., The effects of redox-inactive metal ions on the activation of dioxygen: isolation and characterization of a heterobimetallic complex containing a Mn(III)-(mu-OH)-Ca(II) core. *J. Am. Chem. Soc.* **2011,** *133* (24), 9258-61.

12. (a) Collins, T. J.; Gordon-Wylie, S. W., A manganese(V)-oxo complex. *Journal of the American Chemical Society* **1989,** *111* (12), 4511-4513; (b) Collins, T. J.; Powell, R. D.; Slebodnick, C.; Uffelman, E. S., A water-stable manganese(V)-oxo complex: definitive assignment of a .nu.Mnv.tplbond.O infrared vibration. *Journal of the American Chemical Society* **1990,** *112* (2), 899-901; (c) MacDonnell, F. M.; Fackler, N. L. P.; Stern, C.; O'Halloran, T. V., Air Oxidation of a Five-Coordinate Mn(III) Dimer to a High-Valent Oxomanganese(V) Complex. *Journal of the American Chemical Society* **1994,** *116* (16), 7431-7432; (d) Shirin, Z.; Hammes, B. S.; Young, V. G.; Borovik, A. S., Hydrogen Bonding in Metal Oxo Complexes: Synthesis and Structure of a Monomeric Manganese(III)−Oxo Complex and Its Hydroxo Analogue. *Journal of the American Chemical Society* **2000,** *122* (8), 1836-1837.

13. (a) McDonald, A. R.; Que Jr, L., High-valent nonheme iron-oxo complexes: Synthesis, structure, and spectroscopy. *Coordination Chemistry Reviews* (0); (b) Rohde, J.-U.; In, J.-H.; Lim, M. H.; Brennessel, W. W.; Bukowski, M. R.; Stubna, A.; Münck, E.; Nam, W.; Que, L., Crystallographic and Spectroscopic Characterization of a Nonheme Fe(IV)=O Complex. *Science* **2003,** *299* (5609), 1037-1039.

14. Pfaff, F. F.; Kundu, S.; Risch, M.; Pandian, S.; Heims, F.; Pryjomska-Ray, I.; Haack, P.; Metzinger, R.; Bill, E.; Dau, H.; Comba, P.; Ray, K., An Oxocobalt(IV) Complex Stabilized by Lewis Acid Interactions with Scandium(III) Ions. *Angew. Chem. Int. Ed.* **2011,** *50* (7), 1711-1715.

15. Hu, X.; Meyer, K., New tripodal N-heterocyclic carbene chelators for small molecule activation. *Journal of Organometallic Chemistry* **2005,** *690* (24–25), 5474-5484.

16. Chen, J.; Lee, Y. M.; Davis, K. M.; Wu, X.; Seo, M. S.; Cho, K. B.; Yoon, H.; Park, Y. J.; Fukuzumi, S.; Pushkar, Y. N.; Nam, W., A mononuclear non-heme manganese(IV)-oxo complex binding redox-inactive metal ions. *J. Am. Chem. Soc.* **2013,** *135* (17), 6388-91.

17. Prakash, J.; Rohde, G. T.; Meier, K. K.; Jasniewski, A. J.; Van Heuvelen, K. M.; Münck, E.; Que, L., Spectroscopic Identification of an Fe(III) Center, not Fe(IV), in the Crystalline Sc–O–Fe Adduct Derived from [Fe(IV)(O)(TMC)](2+). *J. Am. Chem. Soc.* **2015,** *137* (10), 3478-3481.

18. Saltzman, H.; Sharefkin, J. G., Iodosobenzene. In *Org. Synth.*, John Wiley & Sons, Inc.: 2003.

19. Scarborough, C. C.; WIELICZKO, M., Catalysis in the production of phenols from aromatics. Google Patents: 2015.

20. Wallen, C. M.; Wielizcko, M.; Bacsa, J.; Scarborough, C. C., Heterotrimetallic sandwich complexes supported by sulfonamido ligands. *Inorganic Chemistry Frontiers* **2016,** *3* (1), 142-149.

21. Dolomanov, O. V.; Bourhis, L. J.; Gildea, R. J.; Howard, J. A. K.; Puschmann, H., OLEX2: a complete structure solution, refinement and analysis program. *J. Appl. Crystallogr.* **2009,** *42*, 339-341.

22. Sheldrick, G., SHELXT - Integrated space-group and crystal-structure determination. *Acta Crystallographica Section A* **2015,** *71* (1), 3-8.

23. Sheldrick, G., A short history of SHELX. *Acta Cryst. A* **2008,** *64*, 112-122.

24. Desai, L. V.; Malik, H. A.; Sanford, M. S., Oxone as an Inexpensive, Safe, and Environmentally Benign Oxidant for C−H Bond Oxygenation. *Org. Lett.* **2006,** *8* (6), 1141-1144.

25. Lacy, D. C.; Park, Y. J.; Ziller, J. W.; Yano, J.; Borovik, A. S., Assembly and Properties of Heterobimetallic CoII/III/CaII Complexes with Aquo and Hydroxo Ligands. *J. Am. Chem. Soc.* **2012,** *134* (Copyright (C) 2012 American Chemical Society (ACS). All Rights Reserved.), 17526-17535.

26. Van Heuvelen, K. M.; Fiedler, A. T.; Shan, X.; De Hont, R. F.; Meier, K. K.; Bominaar, E. L.; Münck, E.; Que, L., One-electron oxidation of an oxoiron(IV) complex to form an [O═FeV═NR]+ center. *Proc. Natl. Acad. Sci.* **2012,** *109* (30), 11933-11938.

Chapter 3

Specific Cation Interactions and Effects on Redox and Acid-Base Properties of the Homogeneous Ru_4POM Water Oxidation Catalyst

With Guibo Zhu, Alan M. Bond, and Yurii Gueletii

3.1 Introduction to Cations in Water Oxidation

3.1.1 Redox-inactive Cations in Photosynthesis and OEC Models

The origin of all life-sustaining oxygen on Earth is the four-electron oxidation of two water molecules by an inorganic Mn_4CaO_5 cluster. This oxygen-evolving complex, or OEC, is the only biological molecule known to catalyze this reaction and is found in photosystem II (PSII), the pigment-protein complex where photosynthesis occurs, embedded in the thylakoid membranes of plants, green algae and cyanobacteria. The high potentials required for this reaction (Equation 3.1) are achieved by conversion of light energy from the sun. One of the most peculiar aspects of the cluster is the requirement for the redox-inert Ca^{2+} ion in the cubane core.[66]

$$2H_2O + 4h\nu \rightarrow O_2 + 4H^+ + 4e^- \qquad (3.1)$$

X-ray diffraction (XRD) methods of increasingly higher-resolution capabilities have been applied successfully to determine the structure of the OEC and in order to study the mechanism of water oxidation. Synchrotron radiation (SR) source data at 1.9Å resolution revealed an outer Mn with two coordinating water molecules connected to the distorted cubane Mn_3CaO_4 structure and via bridging oxo ligands, as well as two water molecules that coordinate to Ca^{2+}.[67]

Analysis of high resolution crystal structures can elucidate protonation and oxidation states. Structural analysis of bond lengths and Jahn-Teller distortions in the OEC of crystals of PSII without radiation-damage at 1.95A resolution, achieved using femtosecond X-ray pulses, suggests the oxidation states (III,III,IV,IV) and that one oxygen atom of the Mn_4O_5Ca cluster, which features bond distances to Mn of 2.2-2.7A, is protonated in the S_1 state, in contrast to four bridging oxo ligands with bond distances of 1.8-2.1A. [8]

Although model systems featuring organic ligand scaffolds share some commonalities with the OEC, none of these function as water oxidation catalysts (WOCs). Analogous cation effects have not been previously in synthetic WOCs, and thus neither the true nature of Ca^{2+} in the OEC nor implications for artificial photosynthesis for large-scale solar energy capture have been completely established. Indeed, the specific requirement for Ca^{2+} in the OEC suggests that judicious choice of cation may be critical in artificial WOCs, wherein specific redox-inactive cations may activate or enhance activity in some systems and inhibit or passivate catalysis in others. Thus a fundamental understanding of non-innocent cation interactions in water oxidation is relevant and important to both biological and artificial processes.

3.1.2 Transition Metal-substituted Polyoxometalate WOCs

Artificial water-splitting technology has been recognized as a potentially unlimited replacement for fossil fuels that currently are unsustainable due to long-term environmental and economic costs. Efficient and sustainable water oxidation is a key success-limiting factor in artificially achieving clean and renewable energy. Metal oxides based on Ru, Ir and Co are the most well-established and extensively studied heterogeneous WOCs, where the cubane motif and high oxidation states are common features in these systems. Molecular analogues of these bulk materials can be supported by polyoxometalate (POM) ligands, which are oxidatively robust unlike organic ligand scaffolds (Chapter 1).

One of the most well-established POM WOCs and the first to be reported is $[Ru_4O_4(OH)_2(H_2O)_4(SiW_{10}O_{34})_2]^{1-}$, **$Ru_4$POM**, which has been likened to a minimally-hydrated RuO_2 nanocrystal, and whose cubane core can be compared to the Mn_4O_4 core structure of the OEC. The most significant difference between these two important WOCs is the presence of the redox-inactive ion, Ca^{2+} in the OEC, for which an analogous feature in **Ru_4POM** had not yet been identified.

Despite the advent of more active and faster **CoPOM** WOC's, which are described further in Chapter 4, the slower kinetics, rich electrochemistry, and stability of **Ru_4POM** over a wide pH range have facilitated numerous studies into the nature of water oxidation. Recent electrochemical studies of **Ru_4POM** over the pH range 2 - 12 revealed some unusual cation-specific effects in measurements of the pH-dependence on redox potential; among various group I and II cations, the pH dependence of the first 1-e^- reversible potential is independent of the identity of the electrolyte, except in the case of KNO_3, which shows a plateau in the pH range 4 to 7 with oxidation potential ~0.2 V higher than the plateau for all other electrolytes, which is observed in the pH range of 6 to 8.[68] One hypothesis is that the smaller hydrodynamic radius of potassium ions in solution leads to greater electrostatic interaction, and the observed deviation is the result of ion-pairing. An alternative hypothesis which was tested here is that a *specific* cation binding mode near the active tetraruthenium core results in changes in the redox and acid base properties of this WOC, much akin to the way specific binding of Ca^{2+} ions in the OEC may do the same.

3.1.3 Specific and Non-specific Cation Effects in POMs

There have been some quantitative studies of ion-pairing effects on electron transfer in POMs that are attributable to changes from outer sphere to inner sphere mechanisms, which leads to faster rates of ET when ion-pairing is favored.[69] Bond et al reported the electrolyte cation dependence of electron transfer kinetics in voltammetric studies on the POM $[\alpha\text{-SiW}_{12}O_{40}]^{n-}$ (n=4-6), with *k* values increasing $LiNO_3 < NaNO_3 < KNO_3 \approx NH_4NO_3$. [70] As the Keggin POM is highly symmetrical, this effect on electron-transfer kinetics is presumably non-specific and dependent on the extent of ion-pairing between the anionic POM surface and the cation. In contrast, specific cations are known to be important to the formation and isolation of POM species from solution via crystallization.[71] Specific binding of K^+ and NH_4^+ cations to crown-ether like POM clusters has been observed with binding constants similar to that of 18-crown-6.[72] In the oxidation of alcohols with H_2O_2 by sulfate-containing Preyssler ions, Na^+ and K^+ showed similar catalytic activity.[73] The rate of electron transfer between charged reactants strongly depends on ionic strength but generally do not show specific effects of electrolyte ions.[74] However, the self exchange rates of reactions between anions show a strong specific effect of K^+ in $[Fe(CN)_6]^{3-/4-}$ ([74]) and $[AlW_{12}O_{40}]^{5-/6-}$ couples [75]. It has been proposed that cation catalysis involves the formation of a bridge between two reacting anions by a cation that has been partially dehydrated. [75-76]

In addition to ions pairs with alkali cations, **Ru_4POM** (as well as others) forms a strong ion pair with one or several $[Ru(bpy)_3]^{3+/2+}$ cations[27d, 77]. This ion-pairs are poorly soluble in water and may result in a decrease of overall [**Ru_4POM**] in solution [27d, 78]. It also decreases the quantum yield in light driven water oxidation reactions [77a]. Furthermore, these ion-pairs might be involved in a catalytic bpy-ligand oxidation by Ru^{III} center of $[Ru(bpy)_3]^{3+}$ resulting in a decrease of O_2 yield based on initial $[Ru(bpy)_3]^{3+}$ concentration. The ion-pairing of $[Ru(bpy)_3]^{2+}$ with POMs can be quantified by measuring a quenching of $[Ru(bpy)_3]^{2+*}$ photoluminescence by POM, the effect of counteraction on this process had not been clarified.

The detailed electrochemical studies of **Ru_4POM** had shown that well defined voltammograms are only obtainable when Frumkin double layer effects are suppressed by the presence of a sufficient concentration of additional supporting electrolyte [68, 79] and that K^+ behaves differently than $NaNO_3$, $LiNO_3$, $Ca(NO_3)_2$, $Mg(NO_3)_2$, $MgSO_4$ or Na_2SO_4 in altering the pH dependence of Ru_4POM reversible redox potential.[68] However, since correlations or trends were not observed among the other cations, a *specific* binding interaction of K^+ to the tetraruthenium core of **Ru_4POM**, as opposed to ion-pairing with the polyoxotungstate ligands, could not be ruled out. Commonly, the effect of electrolyte ions on the thermodynamics and rate of electron transfer processes are studied by cyclic voltammetry in electrochemistry and homogeneous kinetics of electron transfer reactions. The relationship between these techniques has been reviewed by Swaddle. [74] In the ideal case, electron transfer between molecules in solution and a solid electrode is mechanistically equivalent to the reaction in homogeneous solution. Generally experimental challenges and interpretational difficulties are associated with electrochemical measurements, as the apparent values of rate constants for electrode reactions often depend on the manner in which the measurements are made. In this context, the studies of the kinetics of homogeneous electron transfer reactions is beneficial.

Thus, since the pH dependence of redox potentials could not be conclusively explained by the electrochemical data and known ion-pairing effects, the alternative hypothesis was brought forth that a specific interaction near the active site is responsible for the observed deviation for K^+ ions. Presented in the following sections are studies conducted in order to give a more definitive account of the interaction between **Ru_4POM** and K^+ and its implications for catalysis.

3.2 Experimental

3.2.1 General Considerations

Reagents were purchased from commercial sources in the highest purity available and used without further purification unless noted. The POM ligand $K_{10}(\gamma\text{-SiW}_{11}O_{34})$ was prepared according to the literature method.[80] **Ru_4POM** was prepared by the literature method[24b] and the 2-electron reduced **Ru_4POM(2^-)** was isolated by modification of this procedure (*vide infra*) and its purity assessed by IR and elemental analysis. FT-IR spectra were obtained on a Nicolet 6700 FT-IR spectrometer with a Smart Orbit diamond ATR attachment. UV-vis spectra were obtaining using an Agilent 8453 spectrophotometer with a diode-array detector. Voltammetric data were acquired using a BAS CV-50W Voltammetric Analyzer potentiostat and CH Instruments electrodes. Nanopure water was obtained from a Metrohm Milli-Q system with resistance of 18.2 $M\Omega\cdot cm^{-1}$. Stopped-flow measurements were obtained using a HI-TECH Scientific KinetAsyst sample handling unit.

Synthesis of ***Ru_4POM(2^-).*** The polyanion **Ru_4POM(2^-)** was synthesized by slight modification of the literature procedure as follows: to a stirring solution of $K_{10}(\gamma\text{-SiW}_{10}O_{34})$ (2.00 g in 10 mL DI H_2O) was added $RuCl_3$ in one portion. The solution immediately became black in color. The solution was allowed to stir for 15 minutes before addition of approximately 2.0 g of KCl. The solution was filtered over a medium-porosity fritted glass funnel and concentrated to approximately 10 mL. To the solution, ethanol was added slowly until the solution was slightly cloudy. The mixture was refrigerated overnight to afford thin black elongated prism crystals in 55% yield. Subsequent crops were obtained from the mother liquor by additional concentration and addition of ethanol.

3.2.2 X-ray crystallography

Singles crystals of **Ru_4POM@**K_3 were obtained by dissolving in the K_2Rb_8 salt in ~1 M KCl and allowing the solution to slowly evaporate. Singles crystals of **Ru_4POM**(2-) were obtained by layering of ethanol onto an aqueous solution of Ru_4POM which had been prepared according to the literature procedure and substituting KCl for RbCl. A suitable crystal was selected and mounted on a nylon loop using paratone oil. Data were collected on a Bruker APEX2 diffractometer using Mo Kα radiation and a CCD detector. The crystal was kept at 109(2) K during data collection with an Oxforford Cryosystems liquid nitrogen controller. The structure was solved using charge flipping and refined using least-squares minimization.

3.2.3 Electrochemical and Electrocatalytic Behavior

Solutions for cyclic voltammetry were prepared by addition of solid electrolytes LiCl, NaCl, and KCl to 1mM solution of **Ru_4POM** in 2,6-lutidine buffer. The lutidine buffer was prepared by preparation of 50 mM lutidine in Nanopure H_2O and subsequent pH adjustment to 7.00 using 6 M HCl. Electrochemical measurements were conducted using a standard 3-electrode setup, with a 3 mM glassy carbon working electrode, Ag/AgCl reference electrode, and platinum wire as counter electrode. Solutions were purged with Ar and maintained under Ar.

3.2.4 Titrations

Acid-base titrations were carried out on 1 mM solutions of **Ru_4POM** in Nanopure water which were purged with argon prior to and maintained under positive argon atmosphere during titration. The solutions were first acidified using 0.1 M HCl and titration conducted with 0.01 M NaOH which was standardized against 0.1M HCl. UV-Vis titrations were conducted in 1 cm quartz cells by addition of solid electrolyte to solutions of Ru_4POM.

3.2.5 Stopped flow kinetics measurements

Stopped-flow measurements were conducted using freshly prepared Ru(bpy)$^{3+}$ and a stock of 1 mM solution of **Ru_4POM** in Britton-Robinson buffer at pH 7.00, to which solid electrolyte was added in order to probe the effect of cations. The absorbance of the main feature associated with [Ru(bpy)$_3$]$^{3+}$ at 670 nm was monitored over time.

3.3 Results and Discussion

3.3.1 Specific Binding of K^+ in the X-ray crystal structures of Ru_4POM

Initial attempts to isolate pure K_{10}[**Ru_4POM**] by simply substituting a K^+ source for RbCl in the original method were not successful, as the elemental analyses showed low Ru even after multiple recrystallizations. Aggregation is known to occur with K^+ in lacunary POMs, and POMs are known to sometimes require isolation from solution via crystallization, after which they can be redissolved and remain stable. Therefore it is not surprising that Rb^+ and Cs^+ were required to isolate the POM. However, recrystallization with ethanol, EtOH, afforded K_{10}[**Ru$_4$POM**].[24b] The structure is shown in Figure 3.1 and shows a remarkable hexadentate binding of two K^+ ions by the tetraruthenium core and W=O groups of the tungstate ligands. The structure may be denoted as **Ru$_4$POM@K$_2$** to signify the binding of 2 K^+ ions. Much like the specificity for certain ions by crown ethers of varying ring sizes, **Ru$_4$POM** in this structure can be described as a chelator analogous to 18-crown-6, which is highly specific for K^+.

Bond valence sum (BVS) calculations show that there are two distinct Ru centers that differ in oxidation state and protonation state. Around the same time, the electrocatalytic oxidation of alcohols by **Ru$_4$POM** was reported; oxidation of ethanol yields 1,1-diethoxyethane and ethyl acetate formed from condensation of acetaldehyde or acetic acid with excess ethanol.[81] As shown in the scheme in Figure 3.2, reduction results in protonation of two μ-oxo ligands. This novel structure suggests that the K^+ may be stabilizing the 2-electron reduced tetraruthenium core, The 2-electron reduced **Ru$_4$POM**, denoted as **Ru$_4$POM(2$^-$)** has only been observed in air free solutions (Claire Besson, unpublished at the time of this work).

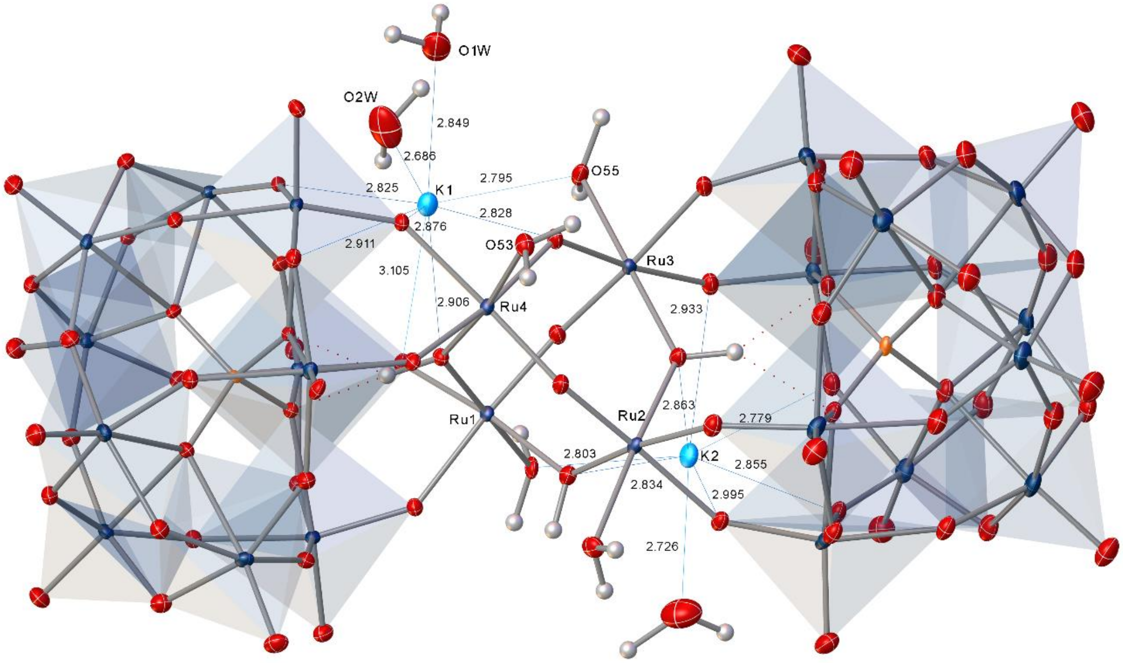

Figure 3.1 X-ray crystal of Ru$_4$POM@K$_2$ .The additional K$^+$ counterions are omitted for clarity and are disordered over interactions with the tungstate ligands. Thermal ellipsoids are shown at the 50% probability level.

$$[Ru_4\,O_{\color{red}4}\,(OH)_{\color{blue}2}(H_2O)_4(\gamma\text{-}SiW_{10}O_{36})_2]^{10-} \xrightarrow{K^+,\ aq.\ EtOH} [Ru_4\,O_{\color{red}2}\,(OH)_{\color{blue}4}(H_2O)_4(\gamma\text{-}SiW_{10}O_{36})_2]^{10-}$$

$$\{Ru^{IV}Ru^{IV}Ru^{IV}Ru^{IV}\} \qquad \{Ru^{\color{red}III}Ru^{\color{red}III}Ru^{IV}Ru^{IV}\}$$

Figure 3.2 Schematic of the 2-electron and 2-proton change that results in the same net charge upon reduction of Ru$_4$POM in aqueous EtOH.

Since pure K_{10}[**Ru_4POM**] could not be obtained *via* direct isolation following synthesis with K^+ salting-out, the K_2Rb_8 salt was recrystallized from neutral high [K^+] aqueous solutions to avoid reduction and presumably isolate a 'resting-state' complex. Slow evaporation of these solutions gave the desired all-Ru^{IV} complex and the X-ray crystal structure this time showed binding of three K^+ ions (Figure 3.3). The structure also reveals that three terminal-hydroxo (Ru-O bond lengths of 2.156, 2.155, and 2.207 Å) ligands which are considerably shorter than the sole terminal aqua ligand (Ru-O bond length of 2.405 Å).

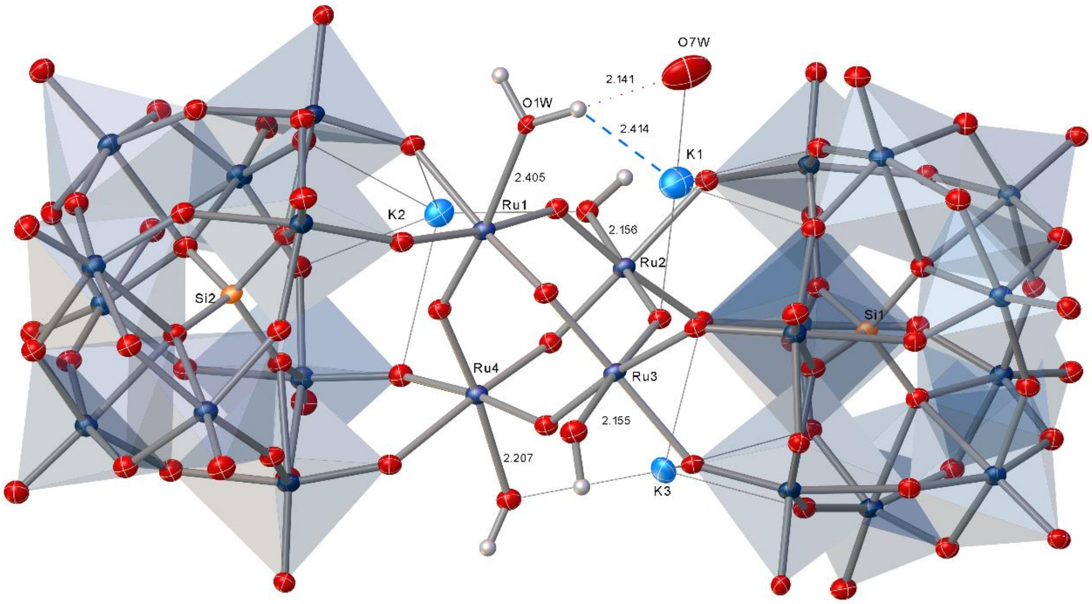

Figure 3.3 X-ray crystal structure of Ru_4POM@K_3. Seven additional K^+ counterions are omitted for clarity. Thermal ellipsoids are shown at the 50% probability level.

In summary, both of these X-ray crystal structures of [**Ru_4POM**] reveal a K^+-specific binding interaction with the tetraruthenium core and possible stabilization of reduced states. The core and POM ligands are capable of chelating K$^+$ ions in the solid state. These ions interact closely with water ligands, which may be involved in water oxidation in solution. The structure of the **Ru$_4$POM@K$^+$** bears many similarities to the OEC, as illustrated in Figure 3.4. The K$^+$ ions coordinate water molecules to complete their coordination sphere, similarly to the way in which the Ca^{2+} ion coordinates water molecules that may be positioned for nucleophilic attack or dioxygen displacement.

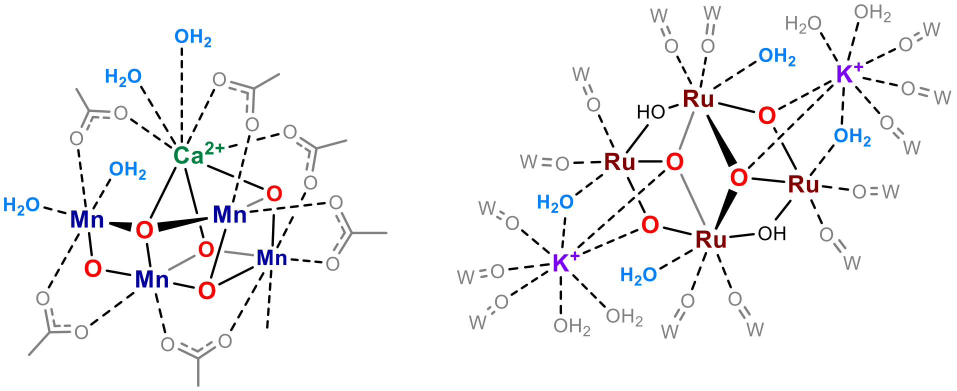

Figure 3.4 Schematic drawing similarities in the coordination of K$^+$ ions in Ru$_4$POM (right) and Ca^{2+} ion in the OEC (left).

Additionally, K+ ions facilitate contact ion pairing between two **Ru$_4$POM** molecules as shown in Figure 3.5. This interaction is specific to the ionic radius of K$^+$, which facilitates dimerization through bridging of the Ru$_4$ core to an adjacent POM. This predicts changes in both rates of electron transfer (ET) as well as redox couples, particularly if these are proton-coupled. The solution-state behavior of **Ru$_4$POM** was examined further to test if the specific binding of K$^+$ could be measured and agreed with the solid-state observations.

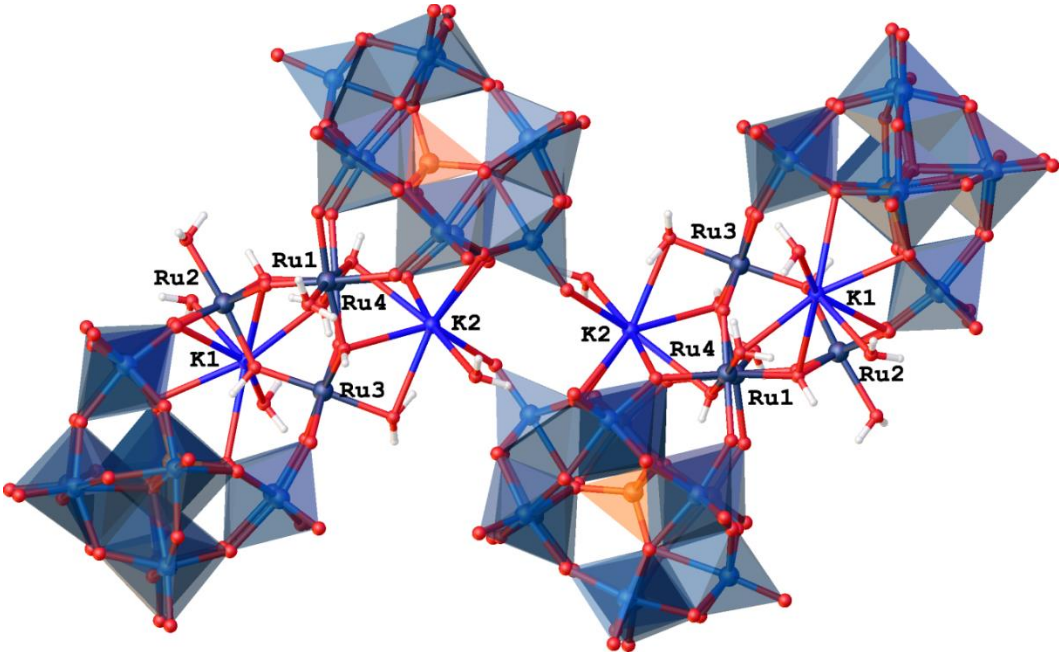

Figure 3.5 Dimerization of two Ru_4POM in the crystal structure of $Ru_4POM(2^-)$.

3.3.2 Cation-specific Deviations in Acid-base Properties

Titrations of **Ru_4POM** with OH^- in the presence of various cations show that K^+ ions have a specific effect on the pK_a values of the complex. Titrations with varying $[K^+]$ show this effect is dependent on $[K^+]$ and the curves suggest that protonation is hindered in the presence of K^+. Figure 3.6 shows the impact of alkali metal cations on the acid-base titration curves for **Ru_4POM**. The curves in the cases with either Li^+ (LiCl) or Na^+ (NaCl) added do not deviate from that in the absence of electrolyte. In contrast, the addition of K^+ (KCl) shows an unexpected and quite pronounced deviation from this behavior. Compared to the other cations, the data showing more base needed to increase the pH suggest that in the presence of K^+, deprotonation of Ru_4POM by OH^- is more facile.

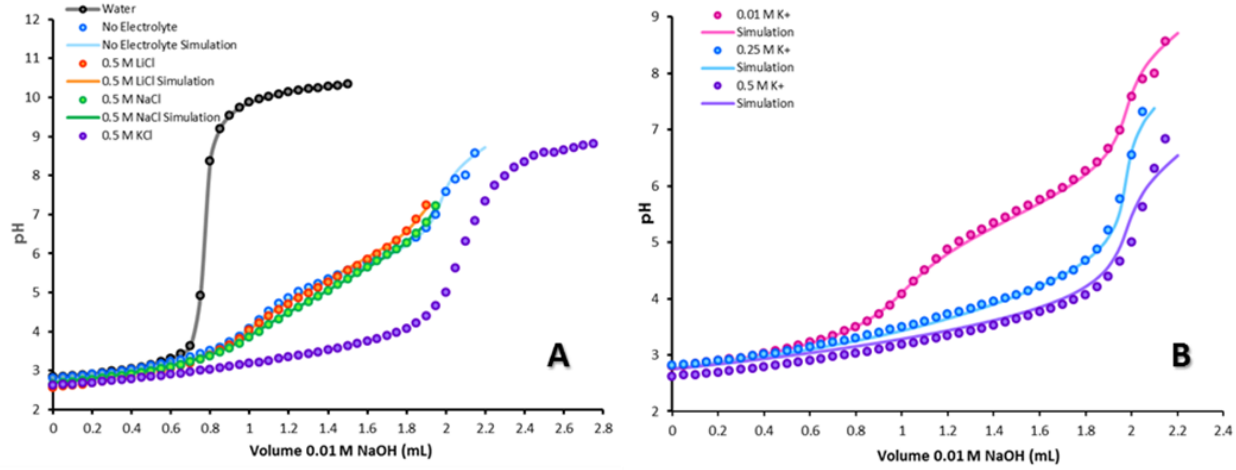

Figure 3.6 Change in pH of 1 mM solutions of Ru_4POM during titration with 10 mM NaOH with no added electrolyte (blue), 0.5M LiCl (orange), 0.5M NaCl (green) and 0.5M KCl (purple).

In order to further probe this effect, the concentration dependence of the deviation were explored as shown in Figure 3.6. The deviation from typical acid-base behavior is more pronounced with increasing [K^+]. This suggests that K^+ and H_3O^+ compete for the same site which is in agreement with the observation of K^+ binding by the POM in the solid state. As described earlier, the **Ru_4POM@K^+** interaction resembles the specific binding of K^+ by 18-crown-6. In addition to K^+, 18-crown-6 is known to bind hydronium ions, as shown in Figure 3.7, as well as protonated primary amines.[82] Consistent with this description, we observe that protonation (i.e. hydronium binding) is hindered in the presence of K^+ ions, as described below.

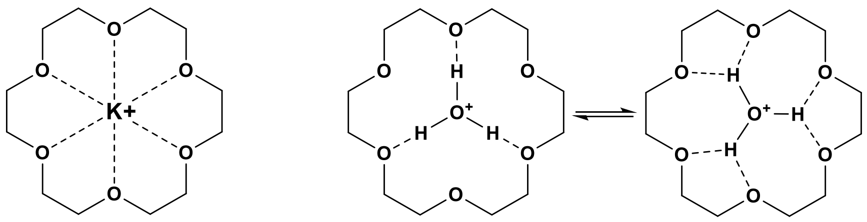

Figure 3.7 Binding of K^+ and hydronium (H_3O^+) by 18-crown-6 ether chelator.

The electronic absorption spectrum of Ru_4POM exhibits a broadened and indistinct feature at neutral pH. This feature sharpens with decreasing pH with the molar extinction coefficient, ε, of λ_{max} at 455 nm reaching a plateau ($\varepsilon = 4.8 \times 10^4$ $M^{-1}cm^{-1}$)at pH~2 (in 0.1M HNO_3). This suggests that the band is associated with protonation of an oxygen atom in proximity to the tertaruthenium core. As shown in Figure 3, the intensity of this band in the electronic absorption spectrum is dependent on the identity of the cation. This feature is associated with $Ru_4O_4(OH)_2(OH_2)_4$ and at pH > 4.0 is not observed for $Ru_4O_6(OH_2)_4$. However, other experimental observations suggest that this band may be associated with Ru-OH_2. Thus, at higher pH, Ru-OH is the dominant species and the feature is not present.

In the absence of an added electrolyte, the absorption maximum is observed. The presence of an additional electrolyte results in a decrease in the extinction coefficient for this feature (Figure 3.8); this suggests that the protonation that results in this feature is prevented to different degrees by different cations. The most significant decrease in absorption in the presence of K^+ ions is consistent with the observation that K^+ has specific effects on acidity of **Ru_4POM**, namely by competing for the site where protonation would occur in the absence of this cation. The observation that ammonium ions have a similar effect is expected if the POM can chelate protonated primary amines similarly to 18-crown-6.

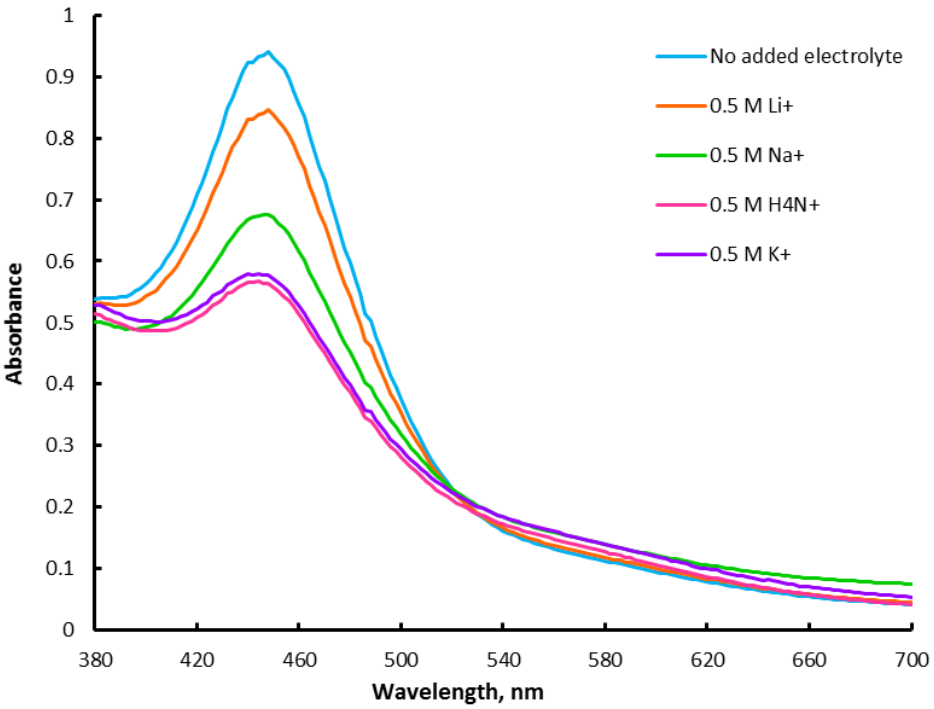

Figure 3.8 Changes in the UV-Vis spectrum of 0.02 mM Ru$_4$POM in the presence of alkali cations.

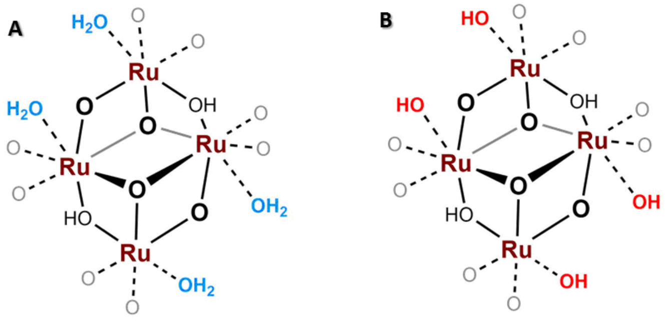

pH < 2
lambda max 455 nm

increased pH
no defined peaks

Figure 3.9 Protonation state changes associated with electronic absorbance spectral features where (a) at low pH all terminal aqua ligands are protonated and (b) increased pH or cation binding leads to proton transfer and loss of the associated 455 nm absorbance band.

The solid-state data indicates that the POM tends to equilibrate to maintain overall charge of 10$^-$. Upon K$^+$ chelation, the anion charge decreases by 1. This change in charge is compensated by the loss of H^+. Therefore the absorbance band is most likely associated with the protonation state changes shown in Figure 3.9. In the presence of K^+ the deprotonation occurs to some extent even in 0.1 M HNO_3.

3.3.3 Effects of Cations on Kinetics of Oxidation

As only the first reversible one-electron redox couple was amenable to a thorough analysis of the pH dependence of potential, the presence of K^+ was probed under turnover conditions to test if this specific binding has a measurable effect on catalytic activity. The kinetics of water oxidation by **Ru4POM** can be monitored by the consumption of the pre-generated oxidant $[Ru(bpy)_3]^{3+}$ by stopped-flow UV-Vis; this is the pre-oxidized form of the photosensitizer typically used in light-driven water oxidation, and the rate of water oxidation can be extracted from the rate of decay of the absorption band associated with the oxidant using stopped-flow UV-Vis spectroscopy.

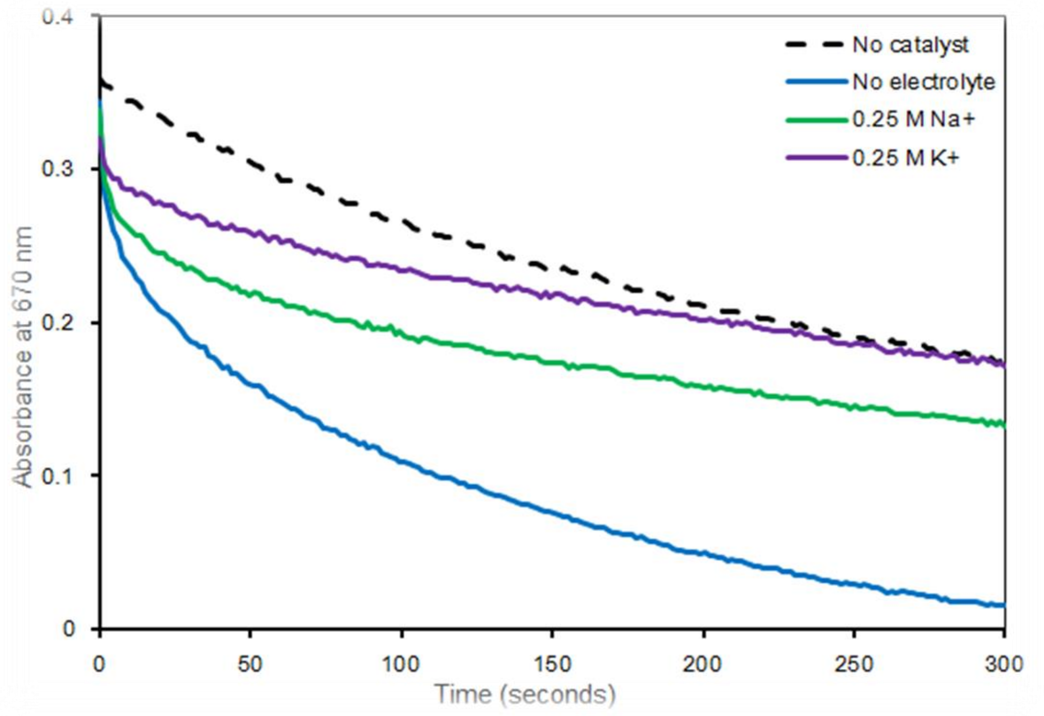

Figure 3.10 Kinetics of $[Ru(bpy)_3]^{3+}$ consumption in the presence of electrolytes. Conditions: 5μM Ru_4POM, 1mM $[Ru(bpy)_3]^{3+}$, 40 mM Britton-Robinson buffer, pH 7.

In order to measure the effects of K^+ cations on water oxidation by **Ru_4POM**, the WOC was exposed to an excess of the oxidant in Britton-Robinson buffer at pH 7 and the consumption of oxidant was measured by decrease in the absorption band at 670 nm. As shown in Figure 3.10, $[Ru(bpy)_3]^{3+}$ self-decomposition occurs at a known rate in the absence of catalyst (dashed line.) As $[Ru(bpy)_3]^{3+}$ is not stable in aqueous solution, a background self-decomposition reaction is observed by the decay of the band at 670 nm in the absence of a catalyst. This self-decomposition is partially mitigated by the presence of supporting electrolytes and is not strongly dependent on cation identity (a non-specific cation effect). In the presence of 1 mM **Ru_4POM**, the increased rate of decay is due to catalytic water oxidation, which is a 4-electron process. Significant differences between the rates of water oxidation as measured by the decay of λ = 670 nm are observed between cations Li^+, Na^+ and K^+.

While the rate of self-decomposition of $Ru(bpy)_3^{3+}$ in water is also mitigated by the presence of cations, however this is primarily an effect of ionic strength. At the same ionic strength, a more significant inhibition of **Ru_4POM** is observed for K^+ compared to Na^+, although the effect could not be modeled quantitatively due to the competing self-decomposition reaction. These individual aspects of redox properties and acid-base are both expected to be contributing factors to the kinetics and thermodynamics of the overall water oxidation process.

In the presence of **Ru_4POM**, the absorbance of the oxidant decays rapidly as water oxidation occurs until the oxidant is consumed. In the presence of added electrolyte, the rate of self-decomposition is lower overall and the cation-dependence of this process is likely to be important but is beyond the scope of this work. Although quantitative values for the effect of the cation are difficult to extract due to the confounding self-decomposition of $[Ru(bpy)_3]^{3+}$, it is evident from Figure 3.10 that at constant ionic strength below that at which self-decomposition is markedly affected, K^+ have a significantly more pronounced effect on water oxidation than Na^+.

3.4 Conclusions

Unlike OEC mimics which do not catalyze water oxidation, neither redox potentials nor pKa's correlate to countercation identity or Lewis-acidity for the **Ru_4POM** WOC. The specific binding of K^+ ions to the tetraruthenium core of **Ru_4POM** has significant effects on the Ru redox potential and pKa of the associated u-oxo and terminal aqua ligands. The presence of K^+ stabilizes the 2-electron reduced POM **Ru_4POM(2^-)** and facilitated its isolation in the solid state. The binding of K^+ in the resting state results in deprotonation of associated terminal aqua ligands in the solid state, as revealed by XRD. Features in the UV-Vis spectrum associated with pH increase are also reproduced by K^+ ions, strongly suggesting this interaction and deprotonation takes place in solution as well and this is responsible for the pH-dependence of this absorption band.

Although quantitative parameters are difficult to obtain due to the many complicating factors, including background reactions, the kinetics of water oxidation appear to be significantly slowed in the presence of K^+. This would be in agreement with other observations that the redox potential and pKa are affected by K^+ binding. This suggests both CCET and PCET exist in the presence of K^+ (Figure 3.11) and the CCET process may be slower overall, possibly due to the strong binding of K^+ stabilizing reduced states.

Ultimately, the binding of K^+ ions was demonstrated to have a detrimental effect if the target is rapid water oxidation kinetics. The binding of K^+ shifts the speciation of POMs in solution due to effects on both redox potential and pKa of associated aqua ligands. However, since the steps where K^+ interaction has the strongest effect are not rate-limiting, more studies on the individual steps – i.e. each oxidation and protonation state towards dioxygen evolution – would be extremely valuable. Despite slowed kinetics, the mechanistic branching, illustrated in Figure 3.10, that is introduced by K^+, e.g. testing for CCET and effects on catalysis, opens many avenues for continued mechanistic, computational, and kinetic studies. After all, the blue dimer is still a major subject of mechanistic studies decades after first being reported as a homogeneous WOC.

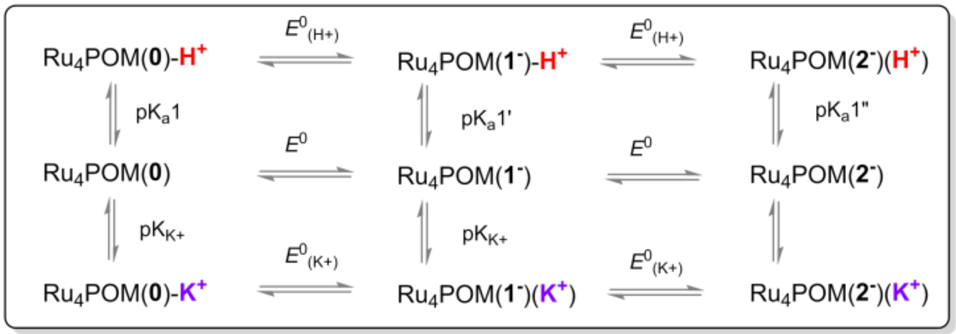

Figure 3.11 Speciation of Ru$_4$POM when K$^+$ ions result in cation-coupled electron transfer and resultant shifts in equilibration.

A major highlight of these studies is the correlation between insights from solid-state structure determination and solution-state dynamics that has been similarly valuable in studies of the OEC structure under different catalytically relevant states to probe the mechanism of water oxidation. These studies demonstrate that K$^+$ may serve as a valuable tool for probing proposed roles of Ca^{2+} in the OEC under conditions where water catalytic oxidation actually occurs. A key difference is that water oxidation in the OEC takes place in the hydrophobic protein environment. In the following chapter, the non-innocent effects of countercations in WOCs will be contrasted with the hydrophobic experimental landscape of innocent, weakly-interacting counterions for studies of hydrolytically unstable Co-based POM WOCs.

3.5 References

1. Ferreira, K. N.; Iverson, T. M.; Maghlaoui, K.; Barber, J.; Iwata, S., Architecture of the Photosynthetic Oxygen-Evolving Center. *Science* **2004,** *303* (5665), 1831-1838.

2. Umena, Y.; Kawakami, K.; Shen, J.-R.; Kamiya, N., Crystal structure of oxygen-evolving photosystem II at a resolution of 1.9 Å. *Nature* **2011,** *473*, 55-60.

3. Suga, M.; Akita, F.; Hirata, K.; Ueno, G.; Murakami, H.; Nakajima, Y.; Shimizu, T.; Yamashita, K.; Yamamoto, M.; Ago, H.; Shen, J.-R., Native structure of photosystem II at 1.95 A resolution viewed by femtosecond X-ray pulses. *Nature* **2015,** *517* (7532), 99-103.

4. Lee, C.-Y.; Guo, S.-X.; Murphy, A. F.; McCormac, T.; Zhang, J.; Bond, A. M.; Zhu, G.; Hill, C. L.; Geletii, Y. V., Detailed Electrochemical Studies of the Tetraruthenium Polyoxometalate Water Oxidation Catalyst in Acidic Media: Identification of an Extended Oxidation Series using Fourier Transformed Alternating Current Voltammetry. *Inorg. Chem.* **2012,** *51* (21), 11521-11532.

5. Grigoriev, V. A.; Cheng, D.; Hill, C. L.; Weinstock, I. A., Role of Alkali Metal Cation Size in the Energy and Rate of Electron Transfer to Solvent-Separated 1:1 [(M+)(Acceptor)] (M^+) Li^+, Na^+, K^+) Ion Pairs. *J. Am. Chem. Soc.* **2001,** *123*, 5292-5307.

6. Li, J.; Bond, A. M.; Zhang, J., Probing Electrolyte Cation Effect on the Electron Transfer Kinetics of the [α-$SiW_{12}O_{40}$]4−/5− and [α-$SiW_{12}O_{40}$]5−/6− Processes using a Boron-Doped Diamond Electrode. *Electrochim. Acta* **2015**, Published online 14 August 2015.

7. Pope, M. T.; Müller, A., Polyoxometalate Chemistry: An Old Field with New Dimensions in Several Disciplines. *Angewandte Chemie International Edition in English* **1991,** *30* (1), 34-48.

8. (a) Boyd, T.; Mitchell, S. G.; Gabb, D.; Long, D.-L.; Cronin, L., Investigating Cation Binding in the Polyoxometalate-Super-Crown [P8W48O184]40−. *Chemistry – A European Journal* **2011,**

17 (43), 12010-12014; (b) Müller, A.; Sousa, F. L.; Merca, A.; Bögge, H.; Miró, P.; Fernández, J. A.; Poblet, J. M.; Bo, C., Supramolecular Chemistry on a Cluster Surface: Fixation/Complexation of Potassium and Ammonium Ions with Crown-Ether-Like Rings. *Angewandte Chemie* **2009,** *121* (32), 6048-6051.

9. Zhang, Z.-M.; Yao, S.; Li, Y.-G.; Han, X.-B.; Su, Z.-M.; Wang, Z.-S.; Wang, E.-B., Inorganic Crown Ethers: Sulfate-Based Preyssler Polyoxometalates. *Chemistry – A European Journal* **2012,** *18* (30), 9184-9188.

10. Swaddle, T. W., Homogeneous versus Heterogeneous Self-Exchange Electron Transfer Reactions of Metal Complexes: Insights from Pressure Effects. *Chem. Rev.* **2005,** *105*, 2573-2608.

11. Czap, A.; Neuman, N. I.; Swaddle, T. W., Electrochemistry and Homogeneous Self-Exchange Kinetics of the Aqueous 12-Tungstoaluminate(5−/6−) Couple. *Inorg. Chem.* **2006,** *45*, 9518-9530.

12. Dogonadze, R. R.; Ulstrup, J.; Kharkats, Y. I., A theory of electrode reactions through bridge transition states; bridges with a discrete electronic spectrum. *J.Electroanal. Chem. Interfacial Electrochem.* **1972,** *39* (1), 47-61.

13. (a) Natali, M.; Orlandi, M.; Berardi, S.; Campagna, S.; Bonchio, M.; Sartorel, A.; Scandola, F., Photoinduced Water Oxidation by a Tetraruthenium Polyoxometalate Catalyst: Ion-pairing and Primary Processes with $Ru(bpy)_3^{2+}$ Photosensitizer. *Inorg. Chem.* **2012,** *51*, 7324-7331; (b) Ballardini, R.; Gandolfi, M. T.; Balzani, V., Dynamic and static quenching of the luminescence of ruthenium(II) polypyridine complexes by heteropolytungstate anions. Direct measurements of intramolecular electron - transfer rate constants. *Inorg. Chem.* **1987,** *26* (6), 862-867; (c) Stracke, J. J.; Finke, R. G., Water Oxidation Catalysis Beginning with 2.5 μM [Co4(H2O)2(PW9O34)2]10–:

Investigation of the True Electrochemically Driven Catalyst at ≥600 mV Overpotential at a Glassy Carbon Electrode. *ACS Catal.* **2013,** *3* (6), 1209-1219; (d) Vickers, J. W.; Sumliner, J. M.; Lv, H.; Morris, M.; Geletii, Y. V.; Hill, C. L., Collecting meaningful early-time kinetic data in homogeneous catalytic water oxidation with a sacrificial oxidant. *Phys. Chem. Chem. Phys.* **2014,** *16* (24), 11942-11949.

14. Guo, S.-X.; Lee, C.-Y.; Zhang, J.; Bond, A. M.; Geletii, Y. V.; Hill, C. L., Mediator enhanced water oxidation using $Rb_4[Ru^{II}(bpy)_3]_5[\{Ru^{III}{}_4O_4(OH)_2(H_2O)_4\}(\gamma\text{-}SiW_{10}O_{36})_2]$ film modified electrodes. *Inorg. Chem.* **2014,** *53* (14), 7561-7570.

15. Liu, Y.; Guo, S.-X.; Bond, A. M.; Zhang, J.; Geletii, Y. V.; Hill, C. L., Voltammetric Determination of the Reversible Potentials for $[\{Ru_4O_4(OH)_2(H_2O)_4\}(\gamma\text{-}SiW_{10}O_{36})_2]^{10-}$ over the pH Range of 2−12: Electrolyte Dependence and Implications for Water Oxidation Catalysis. *Inorg. Chem.* **2013,** *52* (20), 11986-11996.

16. Tézé, A.; Hervé, G., α-, β-, and γ-Dodecatungstosilicic Acids: Isomers and related Lacunary Compounds. In *Inorg. Synth.*, Ginsberg, A. P., Ed. John Wiley and Sons: New York, 1990; Vol. 27, pp 85-96.

17. Geletii, Y. V.; Botar, B.; Kögerler, P.; Hillesheim, D. A.; Musaev, D. G.; Hill, C. L., An All-Inorganic, Stable, and Highly Active Tetraruthenium Homogeneous Catalyst for Water Oxidation. Selected as the VIP Article by the reviewers and editor. *Angew. Chem. Int. Ed.* **2008,** *47*, 3896-3899.

18. Liu, Y. P.; Zhao, S. F.; Guo, S. X.; M., B. A.; Zhang, J.; Zhu, G.; Geletii, Y. V.; Hill, C. L., Electrooxidation of Ethanol and Methanol Using the Molecular Catalyst $[\{Ru_4O_4(OH)_2(H_2O)_4\}(\gamma\text{-}SiW_{10}O_{36})_2]^{10-}$. *J. Am. Chem. Soc* **2016,** *138* (8), 2617-2628.

19. Junk, P. C., Crown ethers as stabilising ligands for oxonium ions. *New J. Chem.* **2008,** *32* (5), 762-773.

Chapter 4

Stability and Reactivity of Cobalt Polyoxometalate Water Oxidation Catalysts with Hydrophobic Counterions in Non-aqueous Media

With Kevin P. Sullivan, Mooeung L. Kim, Sarah M. Lauinger, Daniel Collins-Wildman, Anil K. Mehta, Yurii V. Geletii, John Bacsa, Djamaladdin G. Musaev, and Craig L. Hill

Partially published in Marika Wieliczko, Yurii V. Geletii, John Bacsa, Djamaladdin G. Musaev, Craig L. Hill, "Effects of Competitive Active-Site Ligand Binding on Proton- and Electron-Transfer Properties of the $[Co_4(H_2O)_2(PW_9O_{34})_2]^{10-}$ Polyoxometalate Water Oxidation Catalyst" *J. Cluster Sci.* 2017 **28**: 839. doi:10.1007/s10876-016-1135-3; Adapted with permission of Springer.

4.1 Introduction to Cobalt-catalyzed Water Oxidation

For large-scale energy-harvesting applications, the use of abundant, inexpensive, and readily available elements is preferable over those based on rare and precious elements like Ru. In this realm, cobalt-based materials are especially attractive, as they can often be prepared through self-assembly – even and exhibit self-repair - from abundant elements and have shown considerable promise for efficient and fast water oxidation. The most effective Co-based heterogenous WOCs are CoO_x and amorphous Co*Pi* type materials. As described in earlier chapters, heterogeneous systems are useful for catalyst stability and recycling but also present significant challenges for logical and effective modification to improve desired reactivity and properties. In contrast, molecular catalysts can facilitate detailed studies of mechanistic aspects and properties and lead to improved catalytic activity through rational and/or systematic design. In principle, the activity of a homogeneous catalyst which mimics a metal-oxide type heterogeneous catalyst could be much faster because of the maximized surface area and exposure of catalytically active sites to molecular collisions. Thus, both heterogeneous and homogeneous catalysts are valuable tools for designing amenable energy-harvesting systems. This chapter describes electrochemical studies of the P and V derivatives Co-based POM WOCs, primarily in non-aqueous media, and studies of stability and reactivity in solution.

4.1.1 Heterogeneous Cobalt Catalysts for Water Oxidation

Heterogeneous materials based on Co oxide have shown promise as effective materials for energy-harvesting through water oxidation, for example in the so-called artificial leaf. This system self-assembles from Co(II)$_{aq}$ with sodium phosphate buffer at neutral pH. The cubane motif is a common feature in cobalt WOCs.[83]

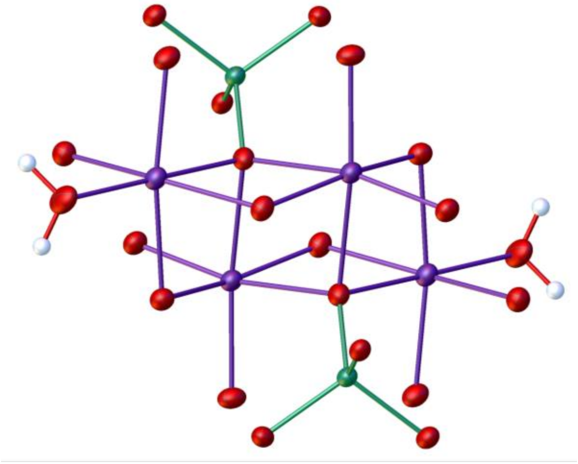

Figure 4.1 Simplified schematic illustrating general composition of some heterogeneous CoWOCs. The purple atoms can represent Co(III) in a Co(II, III) oxide CoO_x material with the green atoms representing tetrahedral Co(II) moieties. In a CoP_i material the purple atoms correspond to Co(II) and the green atoms to PO_4^{3-} moieties.

4.1.2 Homogeneous Cobalt Catalysts for Water Oxidation

Organic systems that are known to catalyze homogeneous water oxidation tend to suffer from ligand degradation as described in Chapter 1. For this reason, the POM-supported WOCs like **Ru_4POM**, studies of which are described in detail in Chapter 3, have emerged as superior systems in terms of oxidative stability. The growing interest in earth-abundant metal-catalysis and heterogeneous cobalt-based systems presents tetracobalt POMs as promising WOCs with potential for large-scale applications, as they do not rely on precious elements. The Tourné-Weakly ions[84] of the general form $[M_4X_2W_{18}O_{68}]^{10-}$ feature four 3d metal atoms (M = Mn, fe, Co, Ni, Zn or Cu; $M_2M'_2$ mixed-metal systems are also possible) arranged between two trivacent lacunary Keggin ions. The $[Co_4P_2W_{18}O_{68}]^{10-}$ derivative, **$Co_4P_2W_{18}$** was reported as a fast, all-inorganic homogeneous light-driven WOC capable of TOF of ~6 s^{-1} (units are mol O_2 mol catalyst^{-1} s^{-1}).

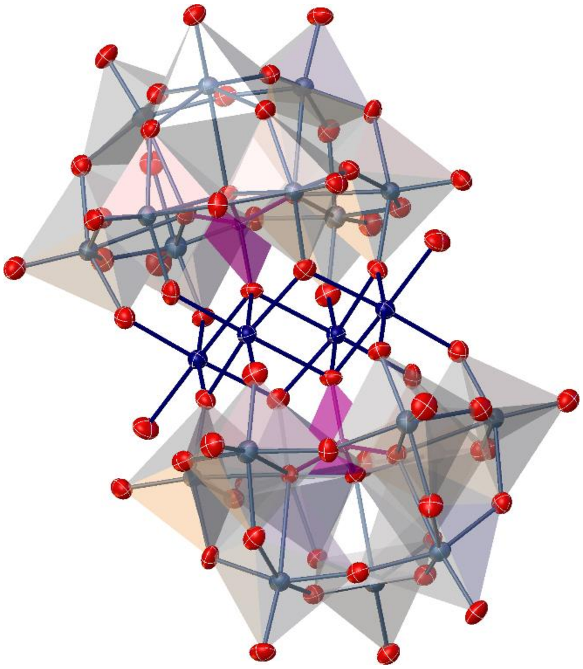

Figure 4.2. Solid-state structure of the Tourné-Weakly ion $[M_4X_2W_{18}O_{68}]^{10-}$ where the central belt is composed of four first-row transition metals.

Similarly to the way in which the tetraruthenium core of the **Ru_4POM** WOC can be likened to a minimally hydrated RuO_2 nanocrystal, the **$Co_4P_2W_{18}$** resembles a monolayer of CoO_x sandwiched between the two trivacent Keggin ligands as illustrated in Figure 4.2. The presence of the PO_4^{3-} parallels the proposed structure of amorphous CoP_i nanoparticles of the Nocera-Kanan catalyst system which self-assembles from $Co(II)_{aq}$ in phosphate buffer at pH 7.

The substitution of heteroatom, **X**, is a common modification in POM plenary structures. Substitution of the P of **$Co_4P_2W_{18}$** with V to yield the isostructural $[Co_4V_2W_{18}O_{68}]^{10-}$ derivative, **$Co_4V_2W_{18}$** was reported to result in a nearly 200-fold increase in the rate of water oxidation activity with TOF approaching 1000 s^{-1} as measured by rate of consumption of oxidant in the commonly-used $Ru(bpy)_3^{3+}/S_2O_8^{2-}$ photo-assay. Despite being isostructural, the compounds exhibit remarkably distinct stability and reactivity. However, the origin of such stark differences remains unclear. It has been proposed (Folkman and FInke 2016) that the considerably longer V-O bond length compared to the P-O bond distance in the respective crystal structures may indicate this bonding motif allows a more labile Co(II) center. Thus the difference between the rates of water oxidation could not be fully explained and continues to be debated, although this discovery suggests promising new routes for probing contributing factors to catalytic activity and stability.

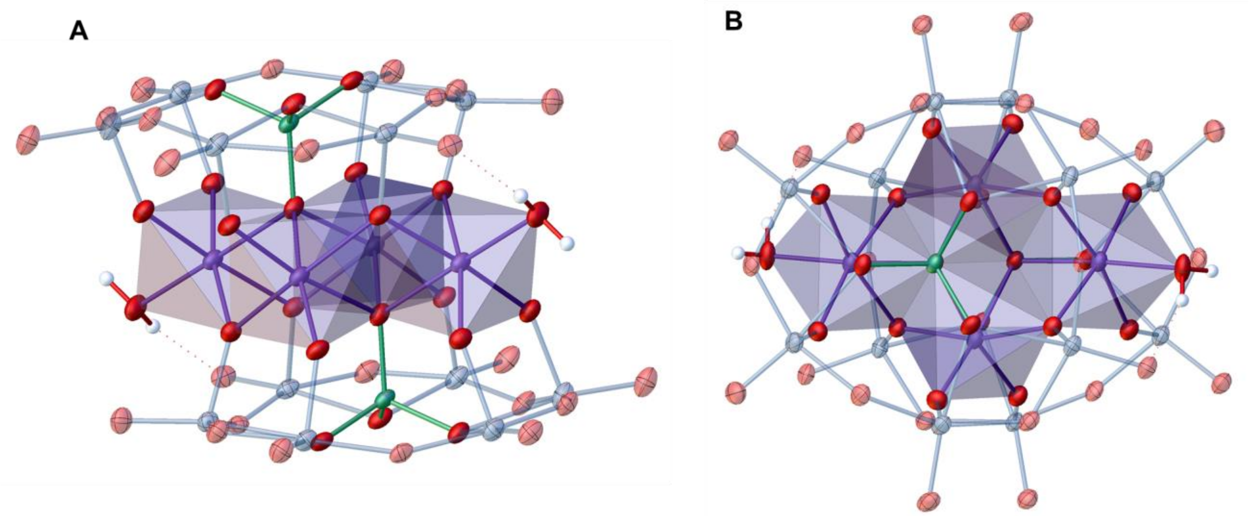

Figure 4.3 Tetracobalt core of $Co_4X_2W_{18}$ POM WOCs shown in (a) side-on~9.5 A across from Co-Co terminal ligands coordinating atom and (b) top-down view, the highlighted area ~6.0 x 9.5 A at its widest.

While the POM ligands impart considerably greater oxidative stability than organic ligand scaffolds, on the other hand, hydrolytic stability becomes problematic for these aqueous systems. The electrochemical properties of these sandwich POMs in aqueous solution are poorly understood, as only a large catalytic wave is observed at high potentials, but the stability of the molecular species is a subject of contention. Given the clear parallels between the compositions, structures, and activities of these POMs and their heterogeneous counterparts, the distinction between catalysis by the molecular species and decomposition to known, heterogeneous catalysts is an important and continued topic of debate with many questions about the identity of the true catalyst remaining. The importance of distinguishing heterogeneous and homogeneous catalysts is described in the following section.

4.1.3 Stability of Homogeneous Catalysts in Aqueous Media

The enhanced reactivity of Co-based systems introduces a problematic issue in that these systems are considerably more hydrolytically unstable than Ru systems like **Ru_4POM**. This is generally due to the propensity of inorganic POM ligands towards hydrolytic rather than oxidative degradation. It was shown that under electrochemical conditions, the $Co(II)_{aq}$ which is leached into solution from **$Co_4P_2W_{18}$** under electrocatalytic conditions (i.e. sustained high potentials in NaPi or NaB buffers) led to formation of CoO_x on the electrode surface for both glassy carbon and fluorinated tin-oxide (FTO). Therefore, a key hypothesis explored here is that the initial oxidation step of a terminal Co(II)-OH_2 to Co(III)-OH_2 results in formation of Co(III)-hydroxide species which aggregate and bind to cathodic surfaces. This immobilization may interfere with the solution dynamics that allow catalytic turnover at the molecular level and instead shift the equilibrium towards further decomposition through deposition of insoluble CoO_x or other amorphous Co-based material.

POMs in aqueous solution are equilibrated systems and are thus, in bulk water, are highly susceptible to hydrolysis; it is not entirely surprising that sustained potentials at electrode surfaces lead to heterogeneous catalyst deposition. This contrasts with a homogeneous system which allows molecular collisions in three dimensions without the influence of a surface-applied potential. Electrochemical studies such as the extensive experiments that have been conducted with the robust **Ru_4POM** would be valuable in ascertaining WOC mechanisms or for elucidating some of the reasons for their differences in reactivity and stability of the CoPOM WOCs, but have been entirely impeded by their hydrolytic degradation. POMs are known to be significantly stabilized against hydrolysis in non-aqueous media. In photosynthesis, water oxidation by the OEC occurs in the hydrophobic protein environment and not in bulk water. The reported reaction rates of the Co_4POMs (6 – 1000 s^{-1}) are on par with those of the OEC (up to 400 s^{-1}). While the estimates for the P derivative are reasonable, the TOF reported for the V analogue was recently brought into question, especially in aqueous conditions where its stability has not been fully established.

In the following studies, the aqueous synthesis, reactivity and stability of **$Co_4V_2W_{18}$** under conditions that are also relevant to **$Co_4P_2W_{18}$** were investigated. Next, the hydrophobic protein environment was mimicked to prevent hydrolytic instability of Co-POM WOCs by introducing alkylammonium cations that weakly interact with the anions, and the alkyl chains can facilitate solubility of these anions in non-aqueous media. The observation and characterization of catalytically relevant intermediates was explored in organic media where it has not been observed in water. The reactivity of the more well-established **$Co_4P_2W_{18}$** towards electrochemical and chemical oxidation as well as competitive inhibition by the terminal ligand was investigated, the stability and reactivity of **$Co_4V_2W_{18}$** in solution were established, and the electrochemical properties of both **$Co_4P_2W_{18}$** and **$Co_4V_2W_{18}$** hydrophobic derivatives and their stability at electrode surfaces were examined.

4.2 Experimental

4.2.1 General considerations

Materials, reagents and solvents were purchased from commercial sources in the highest purity available and used without further purification unless otherwise noted. The acetonitrile-soluble tetra-*n*-butylammonium (TBA) salt of **$Co_4P_2W_{18}$** and **$Co_4V_2W_{18}$** were prepared according to modifications of the literature procedures[85] as described below, from the water-soluble sodium salt, for which preparations have been described elsewhere[25, 86]. The optimized procedure based on extensive modifications of the published procedures for synthesis of and **$Co_4V_2W_{18}$** are described in detail below.The identity and purity were verified using EA, IR and UV-Vis, and ^{51}V NMR in the case of **$Co_4V_2W_{18}$** where EA, UV-Vis, and IR had been shown to be inconclusive in assessing purity. Infrared spectra were recorded on a Nicolet 6700 FT-IR with Smart Orbit Diamond ATR accessory. Elemental analyses for C, H, N, Cl, and Br were conducted by Atlantic Microlabs (Norcross, Georgia) and analyses for Co, P, and W were conducted by Galbraith Laboratories (Knoxville, Tennessee). UV-Vis spectra were obtained on an Agilent 8453 diode-array spectrophotometer equipped with an Agilent 8909A Peltier temperature-control unit. Dioxygen concentrations were measured *in situ* in both headspace and solution using an Ocean

Optics Neofox system with a FOXY-R with FOXY-AF-MG coating and FOXY-PI600 oxygen-sensing probe. Air-saturated solutions were taken as the background.

4.2.2 Synthesis of POMs

Synthesis of Na_{10} *[**$Co_4V_2W_{18}$**].* The sodium salt of **$Co_4V_2W_{18}$** was prepared by modifications of the literature procedure [87] as follows. In a 150 mL beaker, Na_2WO_4 $2H_2O$ (2.97g, 9 mmol) and V_2O_5 (91 mg, 0.5 mmol) were dissolved with stirring in 50 mL NaOAc buffer (1.0 M, pH 4.8) at 70 - 80°C to yield a slightly turbid brownish yellow solution. The solution may be filtered at this point, however we found that it did not significantly affect the yield versus filtration at a later stage. To the stirring heated solution was added $Co(OAc)_2 \bullet 4H_2O$ (498 mg, 2 mmol) and immediately the solution became deep brown. The stirring solution was maintained at 70 - 80°C for 40 - 60 minutes uncovered, until the solution was concentrated to approximately half the original volume. The solution was filtered while hot over a medium-porosity fritted funnel. We observed that the use of a coarse-porosity funnel did not sufficiently trap the fine precipitate that is likely some insoluble V_2O_5 impurities. Within minutes upon cooling to room temperature, dark brown crystals began to form. The solution was allowed to cool completely before ~5mL EtOH was slowly added (to avoid the crystals turning a fine powder that is difficult to collect.) The crystals were allowed to grow for 24 – 72 hours and then collected on a coarse-porosity fritted funnel with aspiration and the brown crystals were washed gently with EtOH. The material was allowed to dry with aspiration for ~30 minutes until it could be transferred to dry overnight on a piece of filter paper to afford the compound in 46-58% yield based on W. Some additional details: addition of 1 g NaOAc increased yield to 66-70%, however required additional purification to remove acetate; IR was used to verify that excess acetate had been removed. In cases where acetate was still present (indicated primarily by the presence of strong bands at 1413 and 1563 cm^{-1} and medium bands at 1640 and 1690 cm^{-1}) washing the material with EtOH again was effective although it did tend to turn crystalline material into a fine powder. As pointed out in FF1 and FF2, the previously-reported FT-IR spectra and elemental analyses may not be sufficient for determining purity and thus ^{51}V NMR was used to assess purity as discussed in the main text. Monitoring of the spectra over time showed that slow decomposition to side-products takes place at ambient conditions. In accordance, the isolation of the target POM from solution in a timely fashion is important. After 72 hours, isolated yields did not increase and ^{51}V NMR showed a greater degree of side-products present in the bulk material.

4.2.3 Conversion to hydrophobic salts

Synthesis of TBA_6H_4***[**$Co_4P_2W_{18}$**]***. An aqueous solution of 532 mg of $Na_{10}[Co_4(H_2O)_2(PW_9O_{34})_2]\cdot20H_2O$ (0.1 mmol in 20 mL) was extracted with three 10mL portions of a solution of TBABr in 1,2-dichloroethane (1.5 g in 30 mL). Light brownish precipitate formed immediately. The organic extract and precipitate were collected and separated by suction filtration. The solid was washed with three 5mL portions of water. The air dried powder was redissolved in a minimal volume of MeCN (~10 mL) in a 20mL scintillation vial. The solution was layered with diethyl ether and allowed to rest overnight, wherein pink prismatic crystals formed, leaving a clear solution. The crystals were collected by decanting the solution, washed with diethyl ether and allowed to air dry, noticeably becoming opaque upon drying. The crystals were allowed to dry for several minutes until the mass measurement was stable in order to afford 458 mg of the title compound in 74% yield. Molecular Weight of $C_{96}H_{220}N_6Co_4P_2W_{18}O_{68}$: 6153.565 g/mol. Mass with L = H_2O : 6189.595 g/mol. Elemental analyses: Found (Calculated % for

$C_{96}H_{224}N_6Co_4P_2W_{18}O_{70}$). C: 18.96% (18.63); H: 3.67% (3.65); N: 1.38% (1.36); Co: 3.76% (3.81); W: 52.7% (53.46); P: 0.904% (1.00).

Synthesis of TBA_6H_4[$\boldsymbol{Co_4V_2W_{18}}$]. The TBA salt of $\mathbf{Co_4V_4W_{18}}$ was prepared *via* the method used to prepare the $\mathbf{Co_4P_4W_{18}}$ analogue [88] which was based on modifications of literature procedures [85] as follows. An aqueous solution of 537 mg of $Na_{10}[Co_4(H_2O)_2(VW_9O_{34})_2]\cdot26H_2O$ (0.1 mmol in 20 mL) was extracted with three 10mL portions of a solution of TBABr in 1,2-dichloroethane (1.5 g in 30 mL). Some brown precipitate formed which largely redissolved upon stirring of the biphasic mixture. The organic extracts were combined, filtered with suction, and washed with three 5mL portions of water. The solution was layered with diethyl ether and dark brown crystals formed over 2-3 days. When allowed to stand in solution over long periods of time, the dark brown crystals of $\mathbf{Co_4V_4W_{18}}$ separated from a dark green supernatant. Attempts to isolate solid crystalline product from this solution were largely unsuccessful, however a combination of UV-Vis and preliminary X-ray diffraction suggest the solution contains $CoBr_4^{2-}$ and *cis*-$V_2W_4O_{19}^{3-}$ anions with TBA cations. This phenomenon is not observed with $\mathbf{Co_4P_4W_{18}}$ and these observations suggest that Br^- anion may accelerate decomposition of $\mathbf{Co_4V_4W_{18}}$ in solution. Thus, the timely isolation of the crystals may be important for high yield when Br^- is present or a different anion may be more suitable for the extraction procedure. The crystals were washed with water and allowed to dry until the mass measurement was stable to afford 358 mg of the title compound in 58% yield. For both $\mathbf{Co_4P_4W_{18}}$ and $\mathbf{Co_4V_4W_{18}}$**,** the IR spectra are similar to those of the Na^+ analogues with additional bands due to TBA (Figure 4.4).

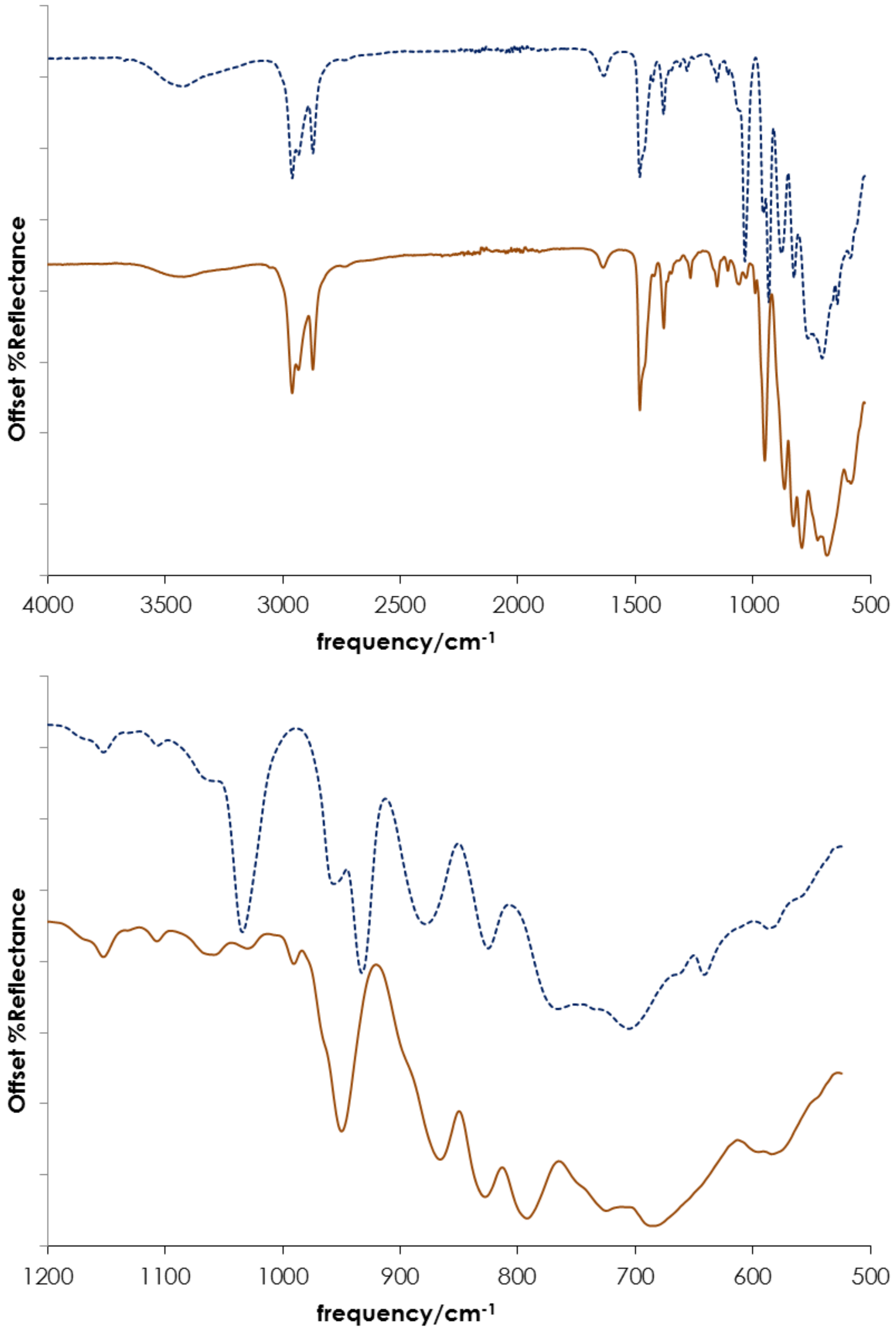

Figure 4.4 Comparison of the FT-IR spectra from 500-4000 cm^{-1} (top) and zoom of the POM fingerprint region from 500-1200 cm^{-1} (bottom) of hydrophobic TBA derivatives of $Co_4P_2W_{18}$ (blue dashed lines) and $Co_4V_2W_{18}$ (solid brown lines)

4.2.4 X-ray crystallography

Single pink crystals of **$Co_4P_4W_{18}$** as its TBA_6H_4 salt were obtained by vapor diffusion of diethyl ether into a concentrated acetonitrile solution. Single red prism-shaped crystals of TBA_6H_4[**$Co_4V_4W_{18}$**] were grown by layering diethyl ether onto a concentrated solution of TBA_6H_4[**$Co_4V_4W_{18}$**] in MeCN.

The crystals of both compounds were unstable at room temperature and were coated immediately with Paratone upon removal from the solvent. The absence of nitrile stretching bands in the IR spectra (~2250 cm^{-1}) confirm the loss of co-crystallized and coordinated MeCN upon drying (Figure 4.3) and so the crystals were coated and mounted quickly to avoid crystal decomposition due to loss of solvent of crystallization. Suitable crystals were selected and quickly mounted in on a nylon loop on a Bruker APEX-II diffractometer with CCD area detector. Data was collected using MoKα radiation (λ = 0.71073 Å) and the crystal was maintained at 100(2) K during data collection with an Oxford Cryosystems Cryostream 700 liquid nitrogen controller. Using Olex2[60], the structure was solved with the XT [61] structure solution program using Intrinsic Phasing and refined with the XL[62] refinement package using Least Squares minimization. **Crystal Data** for $C_{114}H_{248}Cl_4Co_4N_{14}O_{68}P_2W_{18}$ (M = 6652.01 g/mol): monoclinic, space group $P2_1/n$ (no. 14), a = 14.3539(13) Å, b = 32.702(3) Å, c = 20.2799(19) Å, β = 109.9725(14)°, V = 8946.8(14) $Å^3$, Z = 2, T = 100(2) K, μ(MoKα) = 12.034 mm^{-1}, $Dcalc$ = 2.469 g/cm^3, 92049 reflections measured (3.046° ≤ 2Θ ≤ 54.966°), 20452 unique (R_{int} = 0.0544, R_{sigma} = 0.0447) which were used in all calculations. The final R_1 was 0.0679 (I > 2σ(I)) and wR_2 was 0.1745 (all data).

A suitable single crystal (0.42×0.28×0.18 mm^3) was selected and mounted on a loop with paratone oil on an APEX2 Mo source diffractometer equipped with a Oxford Cryosystems low-temperature device, operating at T = 100(2) K. Data were measured using ω scans of 0.5° per frame for 20.0 s using MoK$_\alpha$ radiation (fine-focus sealed X-ray tube, 45 kV, 35 mA). The total number of runs and images was based on the strategy calculation from the program **APEX2** (Bruker). The maximum resolution that was achieved was Θ = 29.575°.

The diffraction patterns were indexed using SAINT (Bruker, V8.37A) and the unit cells were refined using SAINT (Bruker, V8.37A) on 50248 reflections, 76 % of the observed reflections. Data reduction, scaling and absorption corrections were performed using SAINT (Bruker, V8.37A) and CrysAlisPro 1.171.38.41 (Rigaku Oxford Diffraction, 2015) with a spherical absorption correction using equivalent radius and absorption coefficient. Empirical absorption correction using spherical harmonics was implemented in SCALE3 ABSPACK scaling algorithm software.

The final completeness is 99.70 out to 29.575° in Θ. The absorption coefficient μ of TBA$_6$H$_4$[$\mathbf{Co_4P_4W_{18}}$] is 12.034 mm^{-1} and μ of TBA$_6$H$_4$[$\mathbf{Co_4V_4W_{18}}$] is 11.958 mm^{-1} at this wavelength (λ = 0.71073 Å) and the minimum and maximum transmissions are 0.00773 and 0.02831.

The structures were solved and the space group P2$_1$/n (# 14) determined by the **ShelXT** [89] structure solution program using the Intrinsic Phasing solution method and by using **Olex2** [60] as the graphical interface. The model was refined with version 2014/7 of ShelXL-2014/7 (Sheldrick, 2014) using Least Squares minimization. All non-hydrogen atoms were refined anisotropically. Hydrogen atom positions were calculated geometrically and refined using the riding model.

CCDC 1509618 contains the supplementary crystallographic data for TBA$_6$H$_4$[$\mathbf{Co_4P_4W_{18}}$] and CCDC 1540222 contains the supplementary crystallographic data for TBA$_6$H$_4$[$\mathbf{Co_4V_4W_{18}}$]. These data can be obtained free of charge via http://www.ccdc.cam.ac.uk/conts/retreiving.html, or from the Crystallographic Data Centre, 12 Union Road, Cambridge CB2 1EZ, UK.

4.2.5 Electrochemistry

Electrochemical data were obtained using a BAS CV-50W voltammetric analyzer using 3-mm diameter glassy carbon (BAS) working electrode, polished with alumina and rinsed with acetone prior to experiments and a Pt wire as auxiliary electrode. A silver wire was used as a pseudo-reference electrode which was calibrated against the ferrocene/ferrocenium couple in the same solvent/electrolyte system. All potentials (from this study and literature studies) are reported relative to the Fc/Fc^+ couple. Experiments were carried out on freshly prepared 1 mM solutions of $TBA_6H_4[\mathbf{Co_4P_4W_{18}}]$ and $TBA_6H_4[\mathbf{Co_4V_4W_{18}}]$ at room temperature with 0.1 M $TBAPF_6$ as supporting electrolyte. Bulk electrolyses were conducted in a two-compartment electrochemical cell separated by a glass frit. A carbon glassy plate with $S = 1\ cm^2$ was used as a working electrode. At a required time 2 mL of solution from the electrochemical cell were transferred to an optical cell and the spectrum was recorded immediately, after which the solution from the optical cell was returned to the electrochemical cell.

4.2.6 SEM-EDX Measurements

Scanning electron microscopy and energy dispersive X-ray spectroscopy (SEM/EDX) data were gathered at the Clemson University Advanced Materials Center using Hitachi variable pressure scanning electron microscope, S3400N equipped with EDX with 3nm resolution at 30 kV. Samples were prepared using either glassy carbon or FTO in the electrochemical setup described above.

4.3 Results and Discussion

4.3.1 Synthesis of Co_4POMs and Conversion to Hydrophobic Forms

One of the most challenging aspects of CoPOM studies is the synthesis and purification of the target POM because in aqueous solution POMs are equilibrated systems and are thus highly susceptible to changes in speciation based on concentration, pH, and temperature. This has led to continued debates regarding the formation of CoO_x under electrochemical conditions and the identity of the true catalyst in solution under light driven conditions. Thus, any studies seeking to establish the nature of the molecular catalyst must begin with high purity samples of the desired POM. A primary criticism made in recent reports is that the syntheses outlined in the 2014 were unsuccessful in yielding $\mathbf{Co_4V_2W_{18}}$ in its pure form. In agreement with the observations of Folkman and Finke, our group experienced difficulty reproducing results from the original reported method of Wu.[87] This original synthetic route employed a 3:2:9 atomic ratio of V:Co:W - three times the stoichiometry for V in the target POM. We observe that the products of this reaction are primarily V-containing Lindqvist ions such as *cis*-$[V_2W_4O_{19}]^{4-}$ ($\mathbf{V_2W_4}$) and $[VW_5O_{19}]^{3-}$ ($\mathbf{VW_5}$). Considering the large formation constant for $\mathbf{V_2W_4}$ the excess V in solution reacts with the available W, shifting the equilibrium towards a mixture of $\mathbf{V_2W_4}$ and $\mathbf{VW_5}$.[27b] It is likely that the bulk material obtained *via* this synthetic method is largely comprised of these anions and not the target POM. The modified 2014 synthesis employed only a slight excess of V, but led to significantly lower yields than the original report from Wu (12.5% compared to 70% originally reported). Our group has continued making efforts to improve the synthetic methodology, and has successfully reproduced the procedure many times with typical yields of 48 - 58% within 24 - 72 hours.

The purity of samples is imperative for quantitative work, and while pure *solid* phases of POMs can be obtained through crystallization, the purity of POM *solutions* is defined by the relative ratios of equilibrated species present upon dissolution in aqueous media. Vanadium NMR is a useful spectroscopic technique for identifying and tracking V-containing species in solution. In Folkman and Finke's 2016 work [27b], the authors correctly point out the ^{51}V NMR signal that was attributed to the title compound, **$Co_4V_2W_{18}$**, is indeed due to **V_2W_4**. From ^{51}V NMR experiments of the material obtained *via* the newly developed synthetic method, both **V_2W_4** and **VW_5** are present after the bulk solid is dissolved in both H_2O and sodium borate buffer (Figure 4.5). As the vanadium atoms in **$Co_4V_2W_{18}$** are located adjacent to four paramagnetic cobalt centers, the ^{51}V signal for **$Co_4V_2W_{18}$** is expected to be significantly shifted and broadened compared to structurally similar, diamagnetic vanadium-containing species. One approach employed was attempting to identify the ^{51}V NMR spectrum of the diamagnetic Zn analogue **$Zn_4V_2W_{18}$** but this compound could not be successfully prepared and only **V_2W_4** and **VW_5** could be isolated from these reaction mixtures.

Revisiting ^{51}V NMR as a spectroscopic handle for **$Co_4V_2W_{18}$** and expanding the spectral window far beyond the expected region for V-containing POMs reveals a significantly shifted peak located at +320 ppm, which represents a chemical shift difference of greater than 800 ppm relative to **V_2W_4** and **VW_5** (at -511 and -526 ppm, respectively). This peak is significantly broadened, with a linewidth of 680 Hz, relative to the ~20 Hz linewidth of these diamagnetic vanadium POMs (Figure 4.4). The substantial chemical shift difference and line broadening is highly suggestive that this peak is due to **$Co_4V_2W_{18}$** in solution. To confirm this assignment, the spectrum was compared to the tetrabutylammonium (TBA) salt of **$Co_4V_2W_{18}$** (Figure 4.10). This hydrophobic POM is soluble in acetonitrile (MeCN), where it is not susceptible to hydrolysis and speciation. The ^{51}V NMR spectrum of this compound reveals a single peak located at +370 ppm, with no signal observed for the hydrolytic breakdown products at -511 and -526 ppm. The linewidth for this +370 ppm signal for the TBA salt in MeCN ($v_{1/2}$ = 690 Hz) is similar to that of the +320 ppm signal observed for the Na^+ salt in water ($v_{1/2}$ = 680 Hz). This chemical shift difference of 50 ppm is reasonable, considering ^{51}V spectra are known to shift significantly depending on the nature of the solvent, counterion, and intermolecular interactions.[90] The X-ray crystal structure reveals MeCN coordination to cobalt in the solid state, which may contribute to the shift observed in solution (Figure 4.10). The presence of this peak as the primary signal for the Na^+ salt, and the exclusive signal for the TBA salt, leads to the conclusion that $\mathbf{Co_4V_2W_{18}}$ is the dominant species in solution under these conditions.

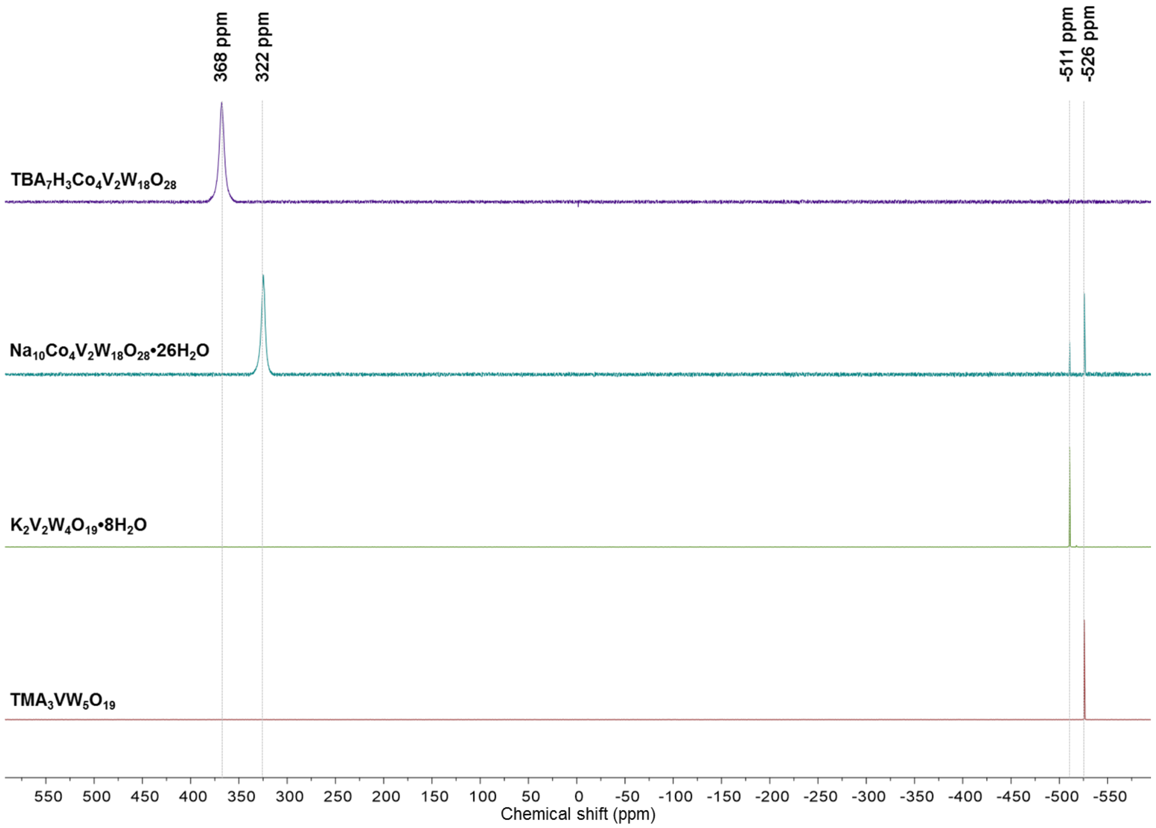

Figure 4.5. The ^{51}V NMR spectra of $Co_4V_2W_{18}$ and $[V_xW_{6-x}]^{(2+x)-}$ POMs (top to bottom); 5 mM $Co_4V_2W_{18}$ as TBA salt in MeCN/CD_3CN (purple) and as Na^+ salt in 10%D_2O/H_2O (green); 5 mM $K_4V_2W_4O_{19}$ (yellow) and 5 mM $TMA_3VW_5O_{19}$ in 10% D_2O/H_2O.

The discovery of this characteristic peak is significant, considering examples of ^{51}V spectra of paramagnetic molecules are exceedingly rare.[27b] This spectroscopic handle allows us to more thoroughly investigate the purity, stability, and solution behavior of **$Co_4V_2W_{18}$**. The ^{51}V NMR spectrum taken 30 minutes after dissolution in 10% D_2O/ H_2O reveals ~2% *cis*-$[V_2W_4O_{19}]^{4-}$ and $[VW_5O_{19}]^{3-}$. After aging 50 days in the same NMR tube at room temperature, signal integration for these side products increases to ~30% with the predominant side product being **V_2W_4**

(Figure 4.6). Thus, though conversion to side products occurs over an extended timescale, **$Co_4V_2W_{18}$** is remarkably stable when dissolved in water.

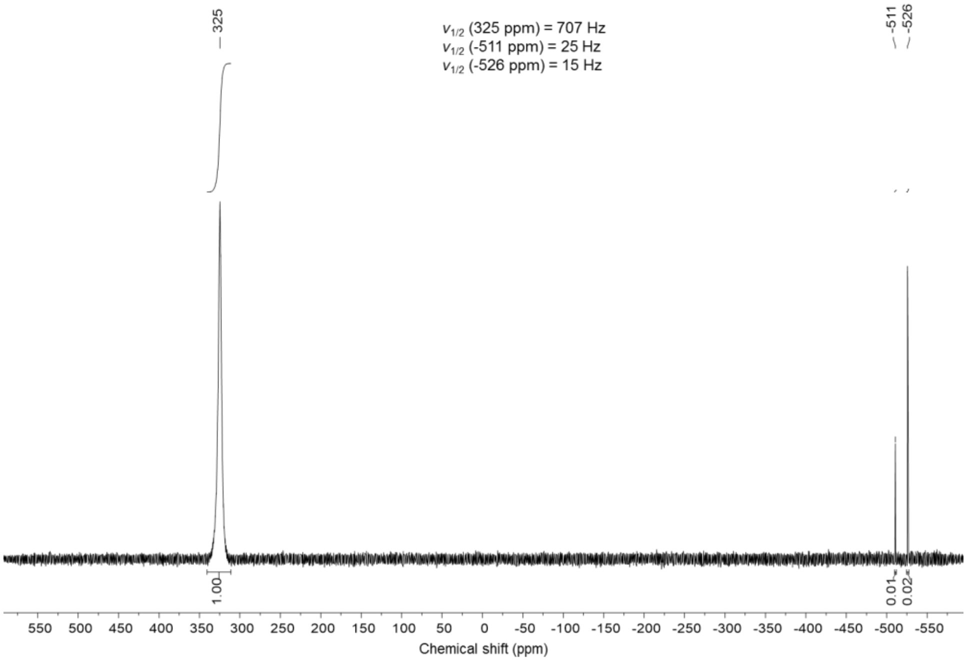

Figure 4.5. The ^{51}V NMR spectrum of $Co_4V_2W_{18}$ taken 30 minutes after dissolution. 5mM $Na_{10}[Co_4V_2W_{18}O_{68}]\cdot 26H_2O$ in 10% D_2O/H_2O. 600 MHz NMR, 512 scans, relaxation delay = 0.5 s, pulse width = 10 µs, acquisition time = 0.08 s

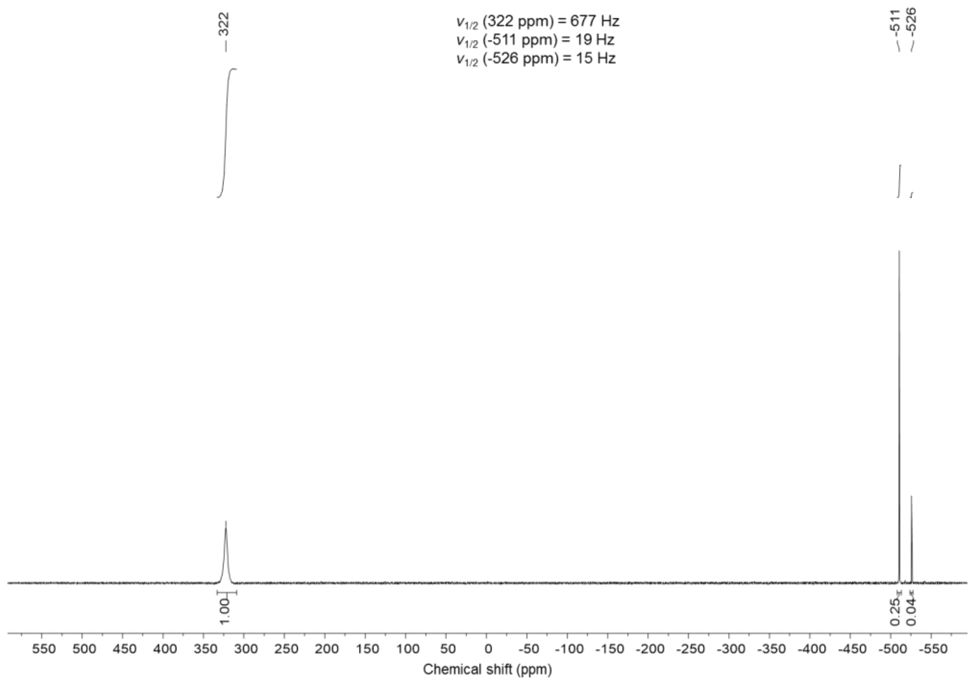

Figure 4.6. The ^{51}V NMR spectrum of $Co_4V_2W_{18}$ taken after aging 50 days in the same NMR tube at room temperature. 5mM $Na_{10}[Co_4V_2W_{18}O_{68}]\cdot 26H_2O$ in 10% D_2O/H_2O. 600 MHz NMR, 512 scans, relaxation delay = 0.5 s, pulse width = 10 µs, acquisition time = 0.08 s

Water oxidation experiments are typically conducted in buffered basic media. Accordingly, the ^{51}V spectrum of **$Co_4V_2W_{18}$** dissolved in 240 mM sodium borate buffer (pH 8.3) shows ~98% pure starting material both 10 minutes and 30 minutes after dissolution, a substantially longer timescale than typical WOC catalysis experiments (Figures 4.7 and 4.8). However, the extremely low concentrations used in water oxidation catalysis preclude the use of ^{51}V NMR to follow speciation under turnover conditions, and requires additional studies to identify the stability of the species under these conditions.

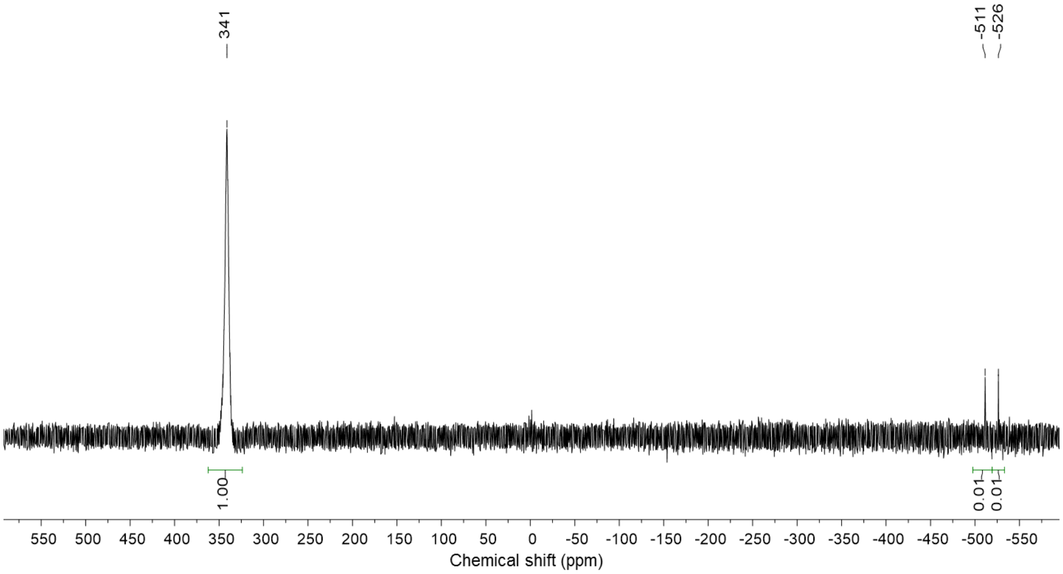

Figure 4.7. The ^{51}V spectrum of $Co_4V_2W_{18}$ in borate buffer 10 minutes after dissolution. 2.5mM Na_{10} $[Co_4V_2W_{18}O_{68}]$•$26H_2O$ in 240mM sodium borate buffer (pH 8.26) with D_2O in coaxial insert. 600 MHz NMR, 512 scans. Relaxation delay = 0.5 s, pulse width = 10 μs, acquisition time = 0.08 s.

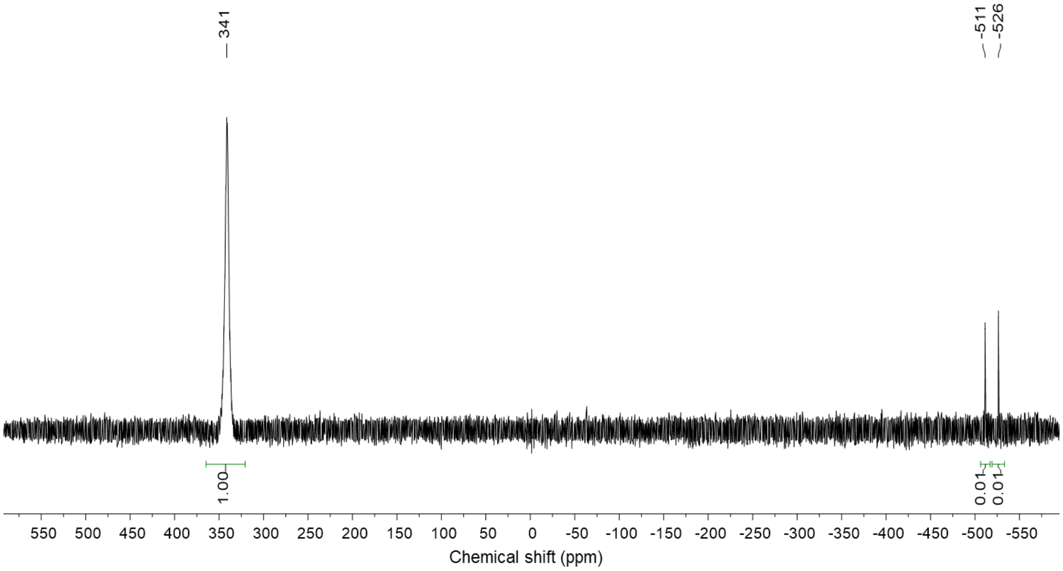

Figure 4.8. The ^{51}V spectrum of $Co_4V_2W_{18}$ in borate buffer 30 minutes after dissolution. 2.5mM $Na_{10}Co_4V_2W_{18}O_{28}$•$26H_2O$ in 240mM sodium borate buffer (pH 8.26) with D_2O in coaxial insert. 600 MHz NMR, 512 scans. Relaxation delay = 0.5 s, pulse width = 10 μs, acquisition time = 0.08 s.

4.3.2 Solid and Solution State Structures of Co_4POMs

The crystal structures of the TBA_6H_4 salts of **$Co_4P_2W_{18}$** and **$Co_4V_2W_{18}$** had not been previously reported. Vapor diffusion or layering of diethyl ether into MeCN solutions afforded X-ray quality single crystals that allowed for structure determination. The crystal structures of **$Co_4P_2W_{18}$** and **$Co_4V_2W_{18}$** show the POMs crystallize with six TBA cations per anion and MeCN in place of water (aqua) as the terminal ligand on the external cobalt centers as shown in Figures 4.9 and 4.10.

In the **$Co_4P_2W_{18}$** structure, the Co-N distance of 2.107(13) Å is comparable to the Co-O bond length in the aqua complex (2.113(7)Å)[91]. Bond valence sum (BVS) confirms the Co(II) oxidation states and the presence of two μ-hydroxo bridges (protonation of atoms O27 and O36) of the polytungstate ligands. The W-O bond lengths (2.010(10) and 1.998(10) Å) at these positions are elongated compared to the other W-O bonds in this coordination geometry (1.806(10) and 1.817(10) Å) consistent with protonation of these oxygen atoms. Thus the centrosymmetric anion of **$Co_4P_2W_{18}$** is, in the solid-state crystal structure, more accurately described as $[Co_4(MeCN)_2(H_2PW_9O_{34})_2]^{6-}$ wherein two distinct cobalt centers are observed. It is not entirely evident whether this exact structure is maintained or whether the protons may be transferred to other moieties in solution.

The anionic charge in the crystals is balanced by the six TBA cations, as illustrated in Figures 4.9 and 4.10, which form weak hydrogen bonds with the tungsten-oxo atoms and surround the POM, effectively encapsulating the POM in the hydrophobic counterion shell. The crystals do not contain any waters of hydration and only co-solvated MeCN molecules are present. This differs from typical POM structures which feature alkali cations that interact directly with the POM and facilitate inter-POM bridging by coordinating water. That is to say, the anion is isolated from contact with other anions as well as water molecules. Interestingly, the structures reveal a small cavity that serves as a binding pocket for the co-crystallization of MeCN

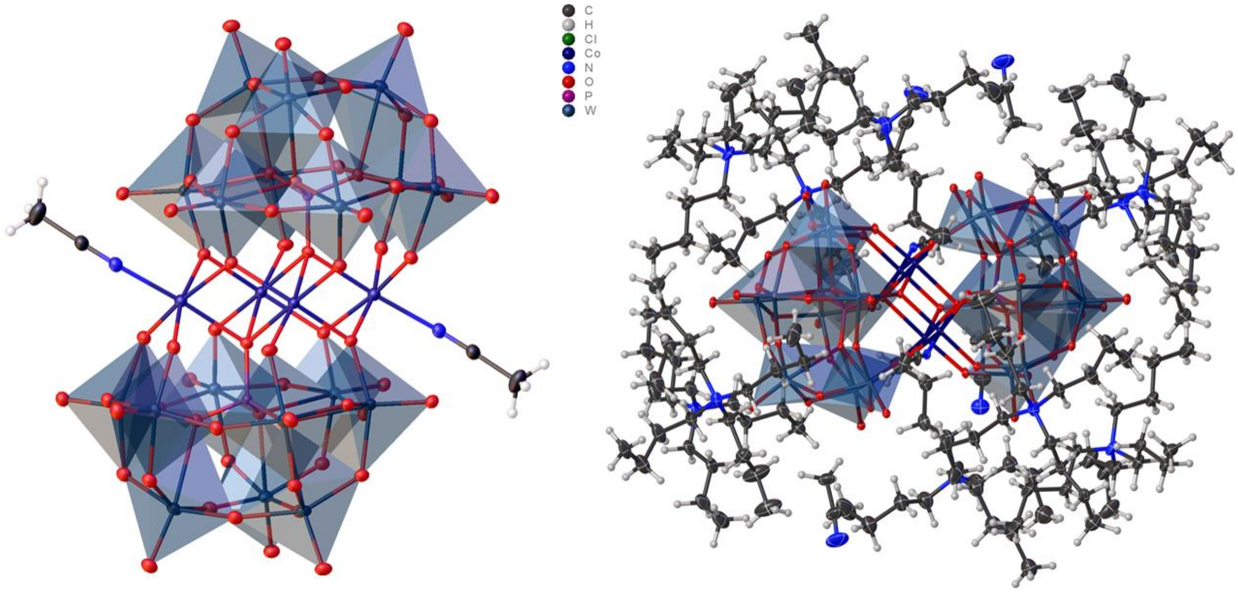

Figure 4.9 X-ray crystal structure of $Co_4P_2W_{18}$ shown as its $[Co_4H_4P_2W_{18}O_{68}]^{6-}$ anion coordinating two MeCN molecules (left) and surrounded by hydrophobic n-Bu_4N^+ counterions. Thermal ellipoids are shown at the 50% probability level.

The **$Co_4V_4W_{18}$** structure is isostructural to that of the **$Co_4P_4W_{18}$** analogue and the two show extremely similar crystal parameters as summarized in Table 4.1; however the **$Co_4V_4W_{18}$** structure exhibits significantly more disorder. As described in the Experimental section, after prolonged periods in solution, signs of decomposition are evident in the **$Co_4V_4W_{18}$** that may contribute to the lower yield upon conversion to the TBA salt. This susceptibility may contribute to the lower overall quality of the **$Co_4V_4W_{18}$** structure. The difference in structure quality can be visualized in the comparison of the thermal ellipsoids of the structures shown in Figures 4.4 and

4.5. The ellipsoids in both figures are shown at the same (50%) probability level, and the increase in positional uncertainty is reflected in the size and shape of the ellipsoid which represents the experimentally-measured electron density. The alkyl chains of the TBA cations show some disorder that is typical of TBA while the anion is fully disordered into more than two components; all nine W atoms were split into only two components where the second component is ~5% occupied.

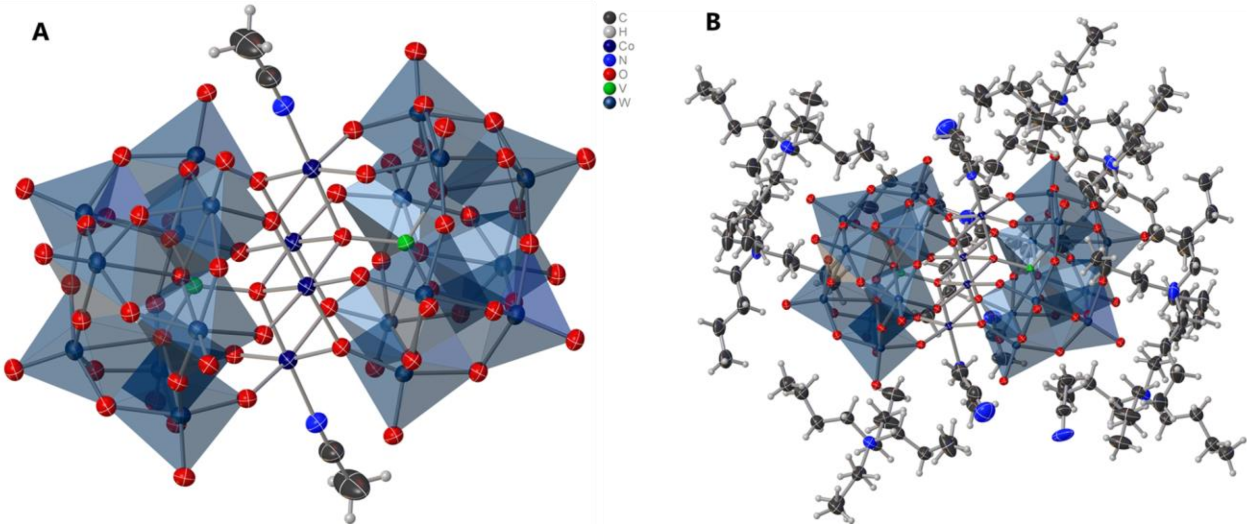

Figure 4.10 X-ray crystal structure of $Co_4V_2W_{18}$ shown as its $[Co_4H_4V_2W_{18}O_{68}]^{6-}$ anion coordinating two MeCN molecules (a) and surrounded by hydrophobic n-Bu_4N^+ counterions (b). Thermal ellipsoids are shown at the 50% probability level.

Due to the significant disorder, the overall quality of the structure model is much lower for the **$Co_4V_4W_{18}$**. Therefore, the bond distances of the **$Co_4V_4W_{18}$** analogue are not as precise, but the distinction is still clear with distances 2.045(15)/2.019(15) vs. 1.853(15)/1.816(15) Å for the analogous μ-hydroxo and μ-hydroxo bond lengths, respectively. Thus the bond lengths of the μ

-OH bonds in the V analogue are similar to the P derivative considering the disorder of this structure, although there is a slight lengthening of the bonds in the V compound. This would be in agreement with some recent proposals that the lengthened bond distances in the V derivative are indicative of a weaker ligand – the VW_9 being a more labile ligand than the PW_9, suggesting a rationale for decreased stability of the V derivative, particulary when ligands capable of binding Co(II) are present. More detailed studies on the stability of $\mathbf{Co_4V_2W_{18}}$ in solution are presented in section 4.3.6.

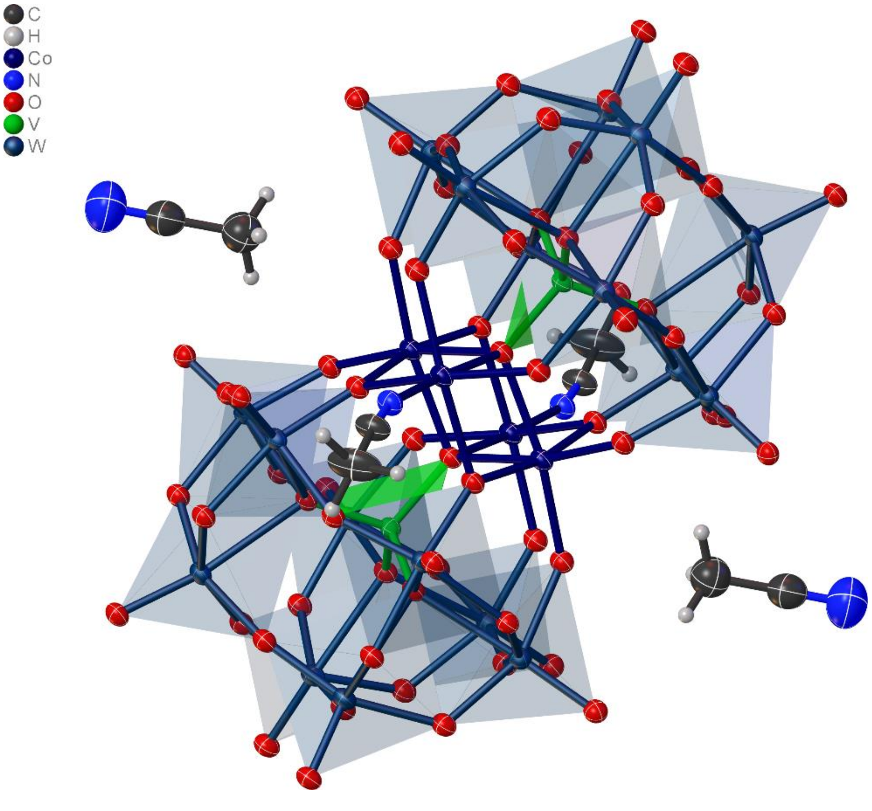

Figure 4.11 Solvent-accessible cavities in the X-ray crystal structure of $Co_4M_2W_{18}$, shown here as its $[Co_4H_4V_2W_{18}O_{68}]^{6-}$ anion. Thermal ellipsoids are shown at the 50% probability level.

Table 4.1 *Crystal parameters for* $\mathbf{Co_4P_4W_{18}}$ *and* $\mathbf{Co_4V_4W_{18}}$

Anion	$\mathbf{Co_4P_4W_{18}}$	$\mathbf{Co_4V_4W_{18}}$
Crystal System	monoclinic	monoclinic
Space Group	$P2_1/n$	$P2_1/n$
a/Å	14.3539(13)	14.4162(2)
b/Å	32.702(3)	32.8597(6)
c/Å	20.2799(19)	20.2434(4)
$\alpha/^\circ$	90	90
$\beta/^\circ$	109.9725(14)	109.886(2)
$\gamma/^\circ$	90	90
V/Å^3	8946.8(14)	9017.7(3)

The coordination of MeCN that is observed in the solid state is corroborated in solution by changes observed in the UV-Vis spectrum. As shown in Figure 4.12, the spectra in MeCN are distinct from those in non-coordinating solvents DCE and THF (Figures 4.13 and 4.14) where terminal aqua ligands are present. MeCN coordination is indicated by a blue-shift of the d-d bands in the UV-spectra, which are similar for $\mathbf{Co_4V_4W_{18}}$ and $\mathbf{Co_4P_4W_{18}}$ although detail of the d-d bands is obscured by the strong V-centered transitions at <500 nm for $\mathbf{Co_4V_4W_{18}}$. Therefore the P analogue is better suited for assessing changes in the UV-Vis spectrum and additional spectral experiments on this compound are discussed in the following section.

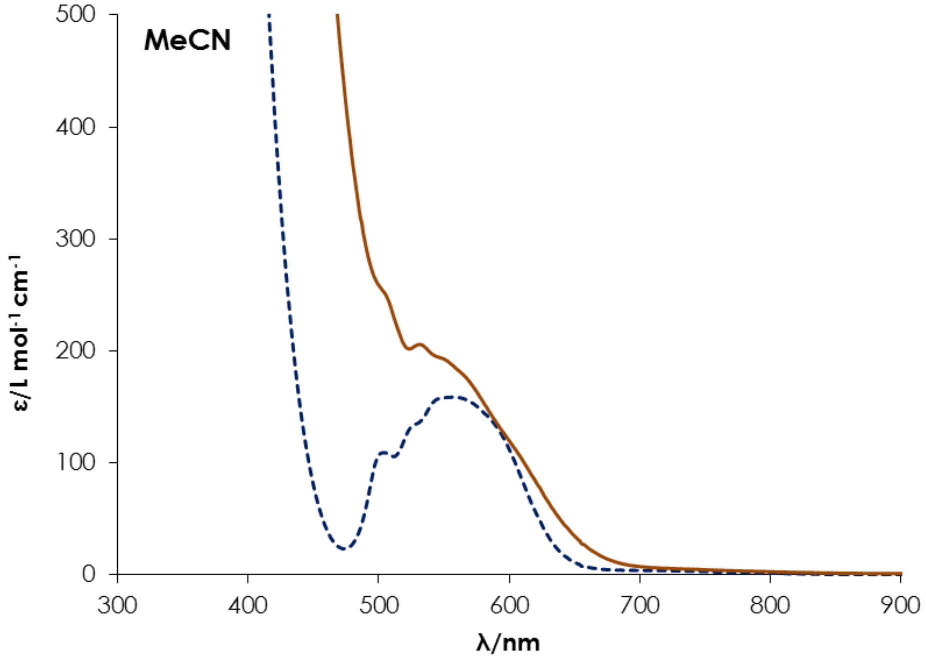

Figure 4.12 UV-Vis spectra comparison of $Co_4P_4W_{18}$ (dashed blue line) and $Co_4V_4W_{18}$ (solid brown line) in MeCN solvent.

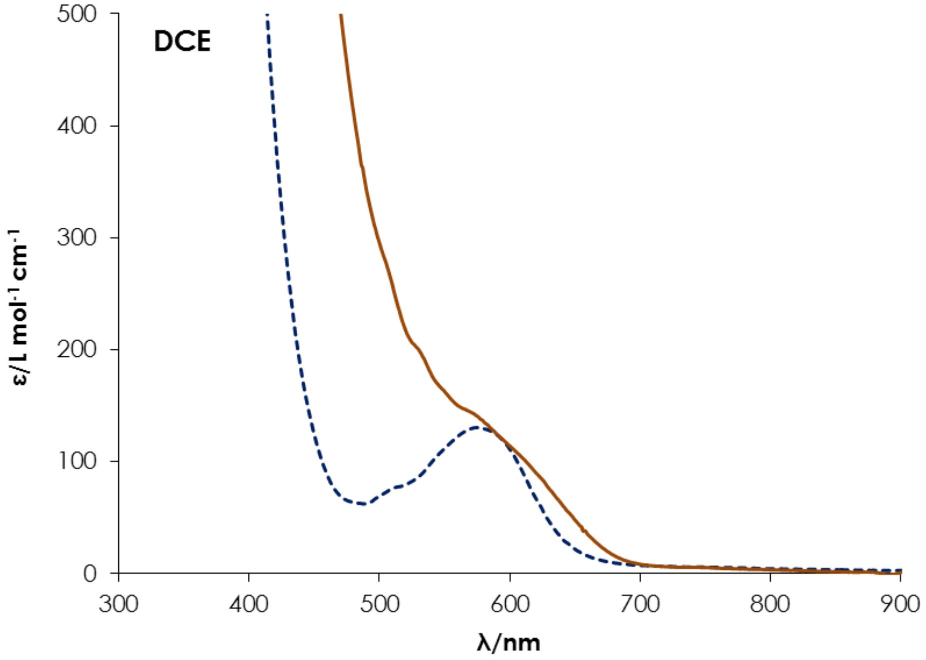

Figure 4.13 UV-Vis spectra comparison of $Co_4P_4W_{18}$ (dashed blue line) and $Co_4V_4W_{18}$ (solid brown line) in 1,2-dichloroethane (DCE) with 0.1 M $TBAPF_6$.

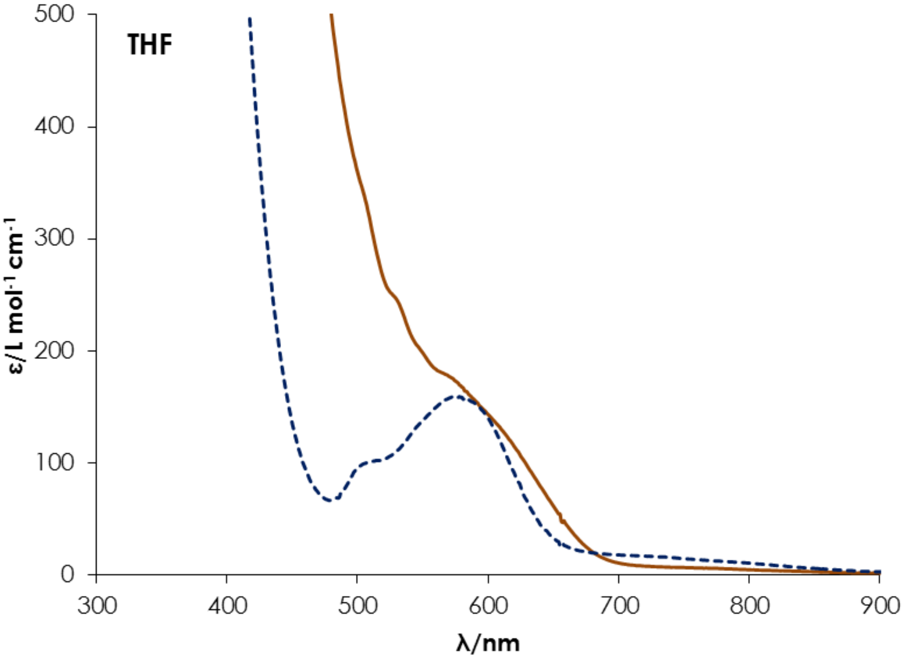

Figure 4.14 UV-Vis spectra comparison of $Co_4P_4W_{18}$ (dashed blue line) and $Co_4V_4W_{18}$ (solid brown line) in tetrahydrofuran (THF) with 0.1 M $TBAPF_6$.

4.3.3 Chemical and Electrochemical Oxidations of $\mathbf{Co_4P_2W_{18}}$ in MeCN

In agreement with the previous report [28], redox events were observable for $\mathbf{Co_4P_2W_{18}}$ in MeCN with 0.1M $TBAPF_6$ as supporting electrolyte. Unlike the previous study employing a Pt foil working electrode which showed two one-electron $Co^{II/III}$ redox couples at +721 mV and +1033 mV, the cyclic voltammetry of $\mathbf{Co_4P_2W_{18}}$ using a glassy carbon working electrode shows one reversible redox couple at +1040 mV. Beyond this redox couple, additional events are observed as shown in Figure 4.15, but neither these nor the first couples are reversible when sufficiently high potentials are applied. As POM charge may be balanced by protons in addition to TBA cations in solution, variance in POM protonation likely facilitates proton-coupled electron transfer. The addition of hydroxide anion, as TBAOH, results in resolution of the single feature into multiple events occurring at lower potentials as illustrated in Figure 4.16. Although this shows that the protonated POM is more difficult to oxidize and may undergo multi-electron PCET rather than individual ET, quantitative studies are precluded by the fact that **$Co_4P_2W_{18}$** is electrochemically unstable in the presence of alkaline H_2O[46-48]. Although similar behavior was observed for **$Co_4V_2W_{18}$** and additional studies to probe the stability of **$Co_4P_2W_{18}$** and **$Co_4V_2W_{18}$** under electrochemical conditions were carried out in anhydrous media as described in section 4.3.5.

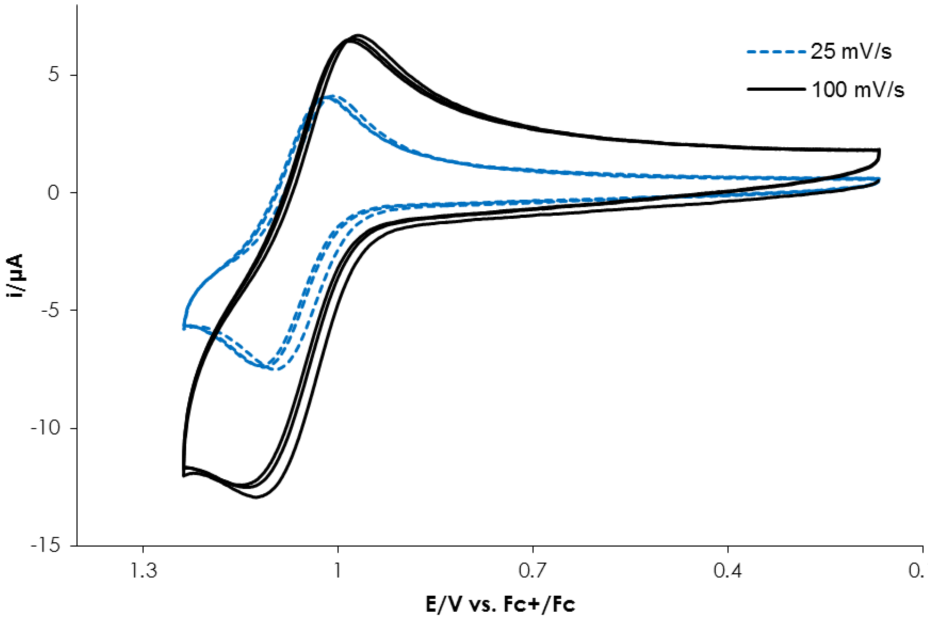

Figure 4.15 Cyclic voltammetry showing single reversible redox couple observed for 500 μM of $Co_4P_2W_{18}$ at a glassy carbon working electrode in MeCN; 0.1 M $TBAPF_6$; scan rate, 25 mV/s (blue dashed line) and 100 mV/s (black solid line).

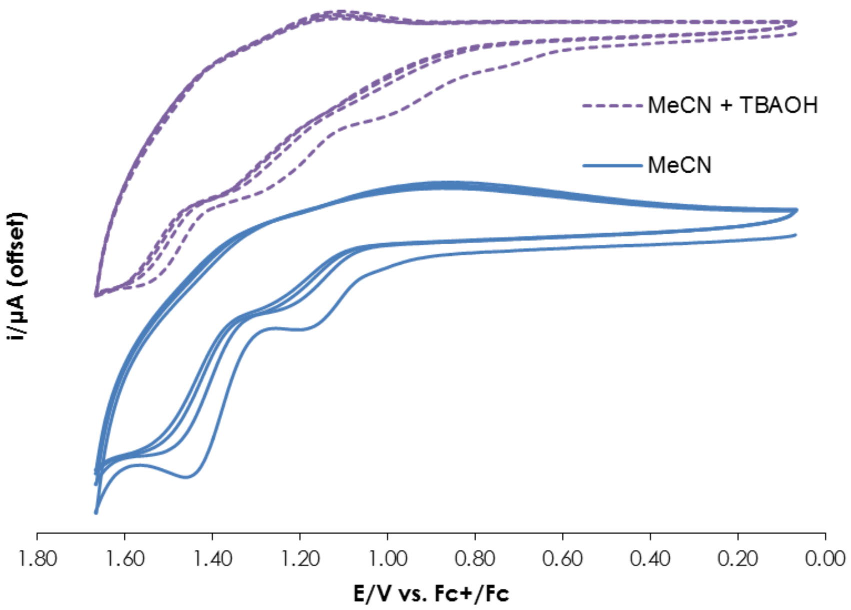

Figure 4.16 Cyclic voltammetry showing irreversible oxidation events observed for 2.0 mM $Co_4P_2W_{18}$ in MeCN (solid blue) and resolution of additional features in presence of hydroxide; 0.1 M $TBAPF_6$; scan rate, 50 mV/s.

The UV-Vis spectrum of **$Co_4P_2W_{18}$** is also expected to change significantly upon oxidation of Co(II) to Co(III), and thus bulk electrolysis of the solution was used to generate the oxidized species which was then monitored spectroscopically. Bulk electrolysis at constant +1300 mV showed spectral changes associated with oxidation, namely broad increases in the absorption spectral regions around 450 nm and 650 nm as shown in Figure 4.17. The current during bulk electrolysis does not stabilize over the time period of 60 minutes and then plateaus. The time dependence of the UV-Vis spectra confirmed that the oxidation product, **$^{27a}{}_{ox}$**, was unstable, as indicated by an exponential decay (k_{app} = 5.3 x 10^{-4} s^{-1}) of the novel absorption features as shown in the inset of Figure 4.18. The spectrum reverted to that of the original, and thus **$^{27a}{}_{ox}$**

could not be isolated under these conditions. The addition of water did not significantly affect the decomposition (re-reduction).

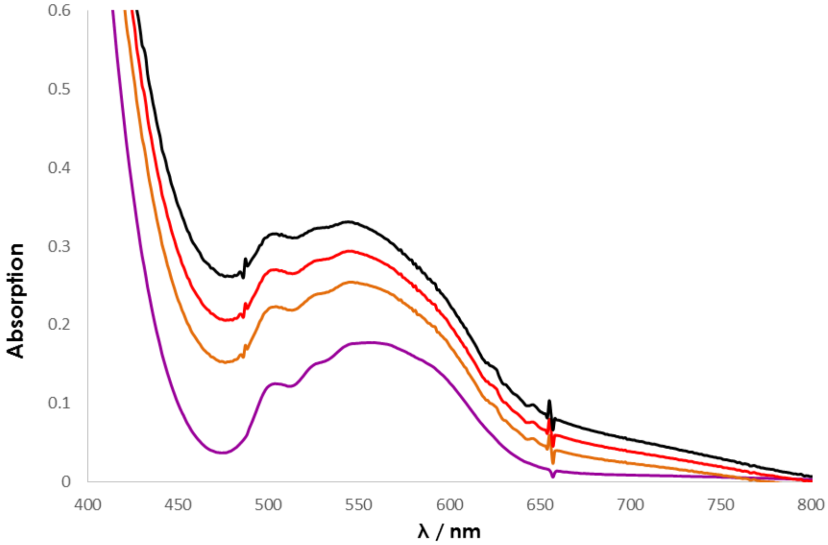

Figure 4.17 Changes in spectra of $Co_4P_2W_{18}$ in the process of bulk electrolysis of $Co_4P_2W_{18}$ in dry MeCN at constant potential, E, in mV, as a function of charge passed through the solution. Conditions: 1 mM $Co_4P_2W_{18}$, 0.1 M $TBAPF_6$, total volume 15 mL, after 0 (pink), 0.4 (orange), 0.56 (red), and 0.8 (black) coulombs were passed. The spectra are recorded in 15-20 min time intervals.

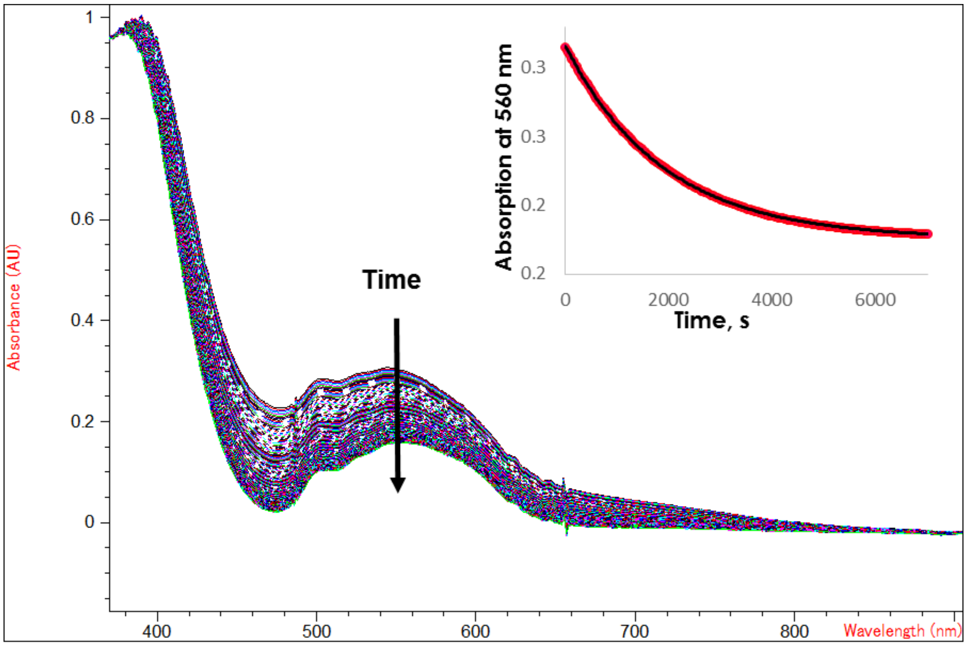

Figure 4.18 Spectral changes of the solution after bulk electrolysis of $Co_4P_2W_{18}$ in MeCN. The kinetics of re-reduction is monitored at 560 nm (inset, a solid line is a fitting to an exponential decay with k_{app} = 5.3 x 10^{-4} s^{-1}).

In order to characterize the oxidized species further, **$Co_4P_2W_{18}$** was exposed to a variety of chemical oxidants in attempts to chemically generate **$\{Co_4P_2W_{18}\}_{ox}$**. Among various oxidants including *N*-oxides, PhIO, H_2O_2 and oxone, the most promising results were observed with a high-potential chemical oxidant that does not absorb in the visible region, [bis(trifluoroacetoxy)iodo]pentafluorobenzene, (FPIFA). Monitoring of the spectral changes as shown in Figure 4.19 shows rapid similar broad increase followed by slower decay, and the spectra of the unstable **$\{Co_4P_2W_{18}\}_{ox}$** intermediate formed in bulk electrolysis and in the reaction of **$Co_4P_2W_{18}$** with FPIFA are very similar (Figure 4.20).

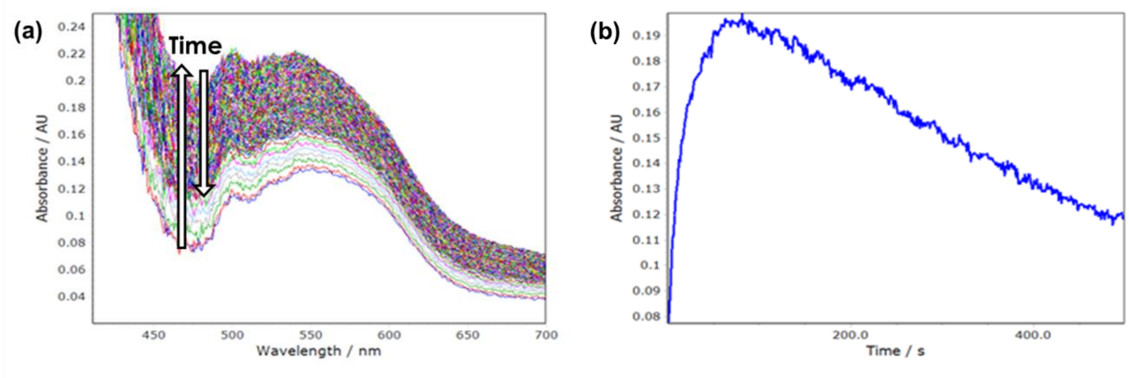

Figure 4.19 (a) Changes in spectra of 0.25 mM FPIFA and 0.5 mM $Co_4P_2W_{18}$ in MeCN. (b) Dependence of absorbance at 470 nm as a function of time.

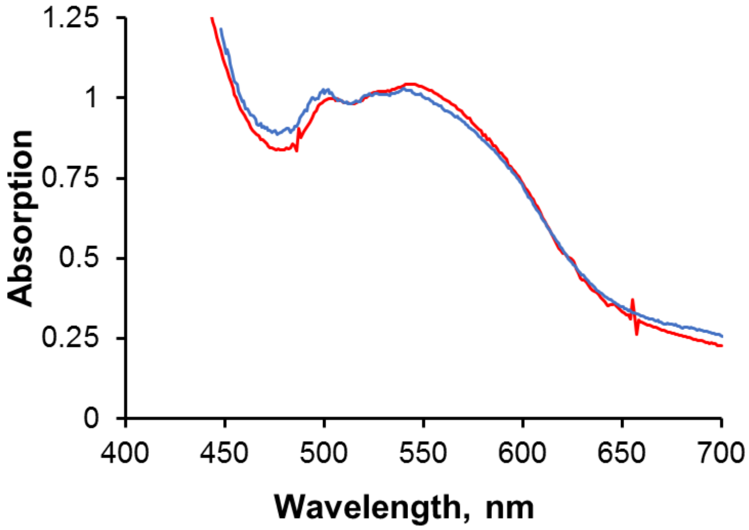

Figure 4.20. The spectra of intermediates (normalized per absorption at 525 nm) generated electrochemically (red) and in the reaction with FPIFA (blue).

Although the oxidized complex could not be isolated from bulk electrolyisis or stoichiometric chemical oxidation by FPIFA, the spectra indicate the reformation of $\mathbf{Co_4P_2W_{18}}$ over time rather than complex decomposition. In contrast, $\mathbf{Co_4P_2W_{18}}$ in aqueous media either shows no signs of reaction or decomposes. To explore the kinetics of oxidation under catalytic conditions, the well-known $[Ru(bpy)_3]^{3+}$ system was employed.[3] Mixing of 0.48 mM $[Ru(bpy)_3]^{3+}$ with 0.05 mM **$Co_4P_2W_{18}$** results in spectral changes depicted in Figure 4.21(a). The changes of absorbance with time at three different wavelengths are shown in Figure 4.21(b).

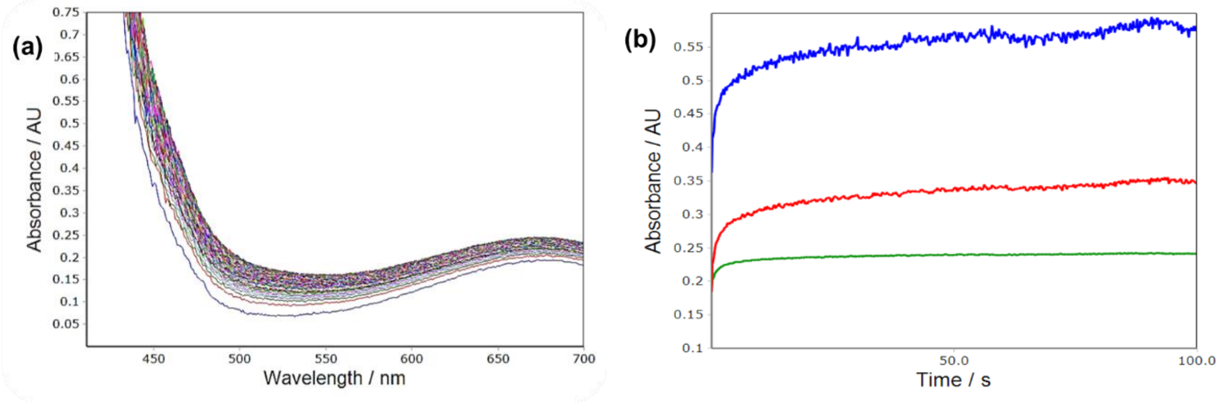

Figure 4.21. (a) Changes in spectra of 0.46 mM $[Ru(bpy)_3]^{3+}$ and 0.05 mM $Co_4P_2W_{18}$ in MeCN, total reaction time 100 s. (b) An increase of absorbance at different wavelengths as a function of time: 680 nm (green); 470 (red); and 450 (blue).

Consumption of $[Ru(bpy)_3]^{3+}$ is expected to decrease the absorbance at 680 nm, but an increase is observed due to formation of the oxidized form of the complex, **$\{Co_4P_2W_{18}\}_{ox}$** which also absorbs at 680 nm. The $[Ru(bpy)_3]^{2+}$ has a strong absorbance band at 450 nm ($\varepsilon = 1.42x10^4\ M^{-1}cm^{-1}$). Therefore the increase in absorbance at 450 nm can be assigned to the formation of 0.014 mM of $[Ru(bpy)_3]^{2+}$. Based on the reaction stoichiometry in eq 2, the concentration of **$\{Co_4P_2W_{18}\}_{ox}$** formed is also 0.014 mM. The difference in standard oxidation potential of $[Ru(bpy)_3]^{3+}/[Ru(bpy)_3]^{2+}$ (1.29 V vs. SCE, or 0.92 V vs. Fc^+/Fc) and **$\{Co_4P_2W_{18}\}_{ox}/Co_4P_2W_{18}$** (1.04 V versus Fc/Fc^+ from CV data in Figure 4.15) is 0.11 V. This difference estimated from the data in Figure 4.21 is 0.115 V, which in excellent agreement with the theoretical value. Thus,

$[Ru(bpy)_3]^{3+}$ is too weak an oxidant and the equilibrium in eq 1 is shifted to the left. $[Ru(bpy)_3]^{3+}$ is not stable towards TBAOH and therefore the proton-dependence could not be explored using the same procedure as in the electrochemical experiments. Thus we tested a non-coordinating organic base, 2,6-lutidine, and observed that consumption of $[Ru(bpy)_3]^{3+}$ takes place in the absence of $\mathbf{Co_4P_2W_{18}}$. In the presence of $\mathbf{Co_4P_2W_{18}}$, consumption is accelerated, as shown in Figure 4.22.

$$[Ru(bpy)_3]^{3+} + \mathbf{Co_4P_2W_{18}} \rightleftarrows [Ru(bpy)_3]^{2+} + \mathbf{\{Co_4P_2W_{18}\}_{ox}} \qquad (1)$$

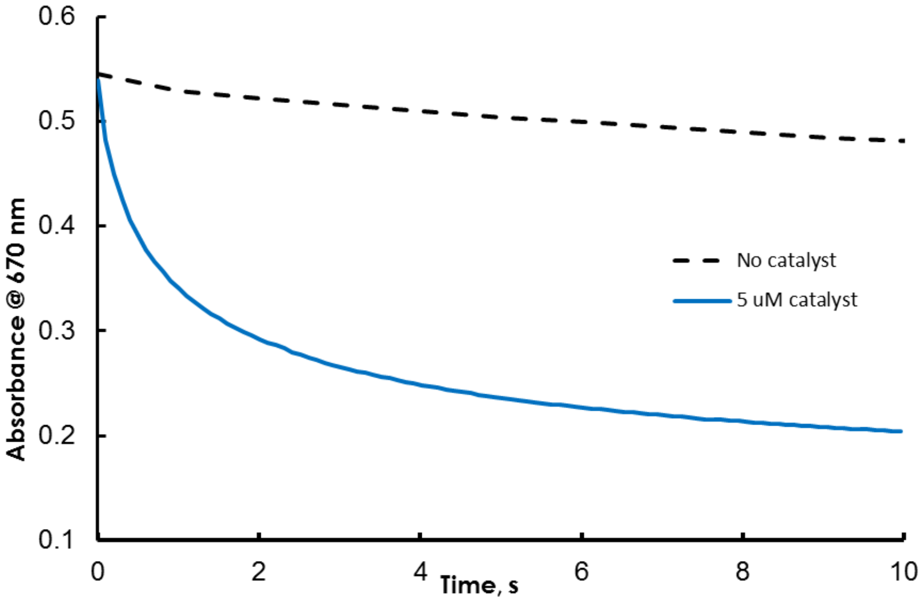

Figure 4.22. Catalytic consumption of $[Ru(bpy)_3]^{3+}$ in MeCN in 2% H_2O, 0.01 M 2,6-lutidine in the absence of $Co_4P_2W_{18}$ (dotted line) and in the presence of 5 μM $Co_4P_2W_{18}$ (blue line)

4.3.4 Dioxygen formation inhibition and pKa modulation in **$Co_4P_2W_{18}$** by MeCN

Under the conditions employed for stopped-flow measurements in H_2O (pH 8), dioxygen formation is quantified using a FOXY probe; however, in all of the experiments in MeCN as described, *no dioxygen formation was detected,* despite catalytic oxidant consumption comparable to that in aqueous media associated with water oxidation. Therefore, although the kinetics suggest a catalytic reaction is taking place, it is not the same water oxidation reaction that is observed in aqueous conditions. Considering the MeCN coordination revealed by the X-ray crystal structure, this suggests the MeCN coordination in solution may be blocking the active site. Thus the effect of MeCN as a competitive binding ligand on water oxidation and dioxygen formation in water was probed. The presence of MeCN (up to 2.5%) does not significantly affect the kinetics of oxidant consumption as shown in Figure 4.23(a). However, it results in almost an order of magnitude decrease in the yield of dioxygen (at 2.5% of MeCN) as shown in Figure 4.23(b).

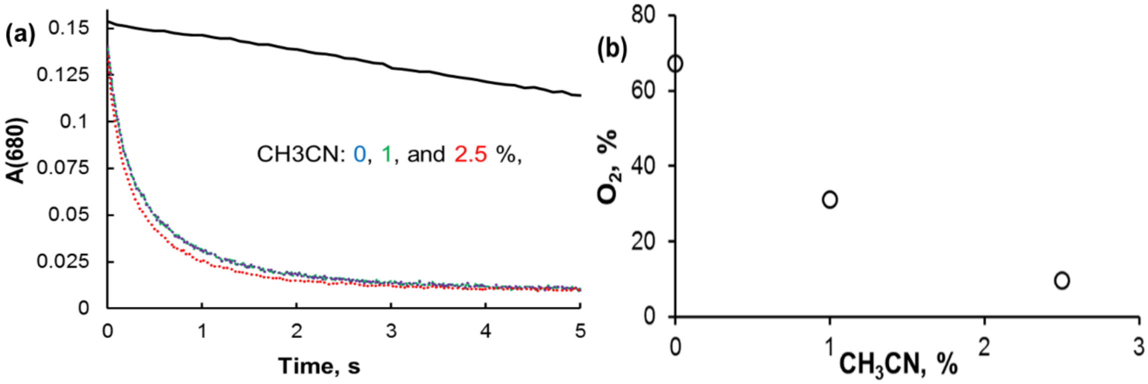

Figure 4.23. (a) The kinetics of $[Ru(bpy)_3]^{3+}$ consumption measured at 680 nm in 80 mM sodium borate buffer (pH 8.0) in the presence of 2.5 μM $Co_4P_2W_{18}$ at 0 (blue), 1 (green) and 2.5 (red) MeCN

(%, v/v). Conditions: 0.36 mM initial [Ru(bpy)$_3$](ClO$_4$)$_3$, 25 °C. Black line: no catalyst, no MeCN. (b) The final yield of O_2 per initial [Ru(bpy)$_3$](ClO$_4$)$_3$ (in %) as a function of added MeCN.

UV-Vis shows spectral changes in the presence of OH^- that suggest MeCN, H_2O, and OH^- can compete as terminal ligands on the two exterior Co atoms. As shown in Figure 2, the spectrum of **$Co_4P_2W_{18}$** in MeCN is slightly blue-shifted with λ_{max} = 555 nm compared to that in water where λ_{max} = 580 nm (ε = 158 L mol^{-1} cm^{-1}), indicating possible coordination of MeCN. Spectra were not significantly affected by the water content of the MeCN (i.e. anhydrous vs. "wet" MeCN), indicating a strong binding of MeCN to **$Co_4P_2W_{18}$**. Titration with 0.1 M OH^- results in shifting of the absorption feature towards that observed in water. The maximum absorption was observed with 5 equivalents of OH^- at 585 nm with ε = 170 L mol^{-1} cm^{-1}. These changes in the UV-Vis spectrum are consistent with the spectrochemical series where the ligand-field-splitting parameter follows the pattern $OH^- < H_2O <$ MeCN. The strong effect of OH^- addition implies that OH^- ligand binds much more strongly to **$Co_4P_2W_{18}$** than MeCN or H_2O.

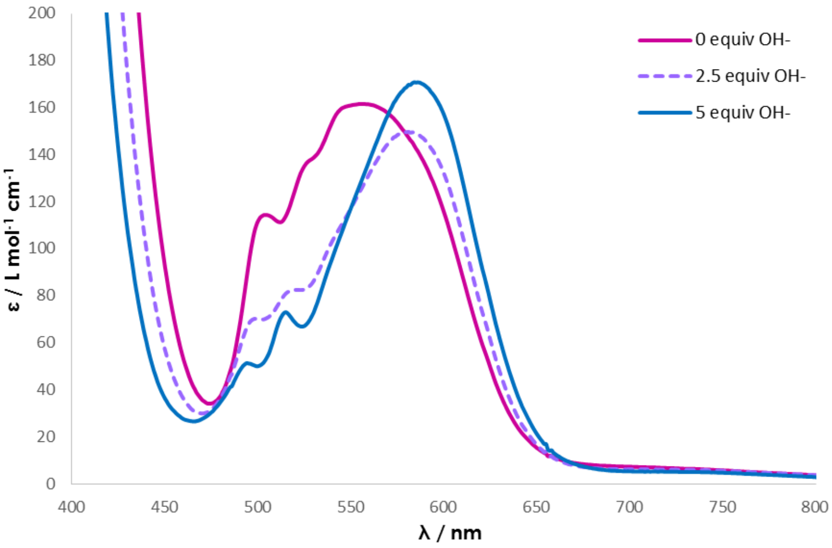

Figure 4.24. Visible spectrum of $Co_4P_2W_{18}$ in MeCN with 0.1 M $TBAPF_6$ during titration with hydroxide (0.1 M TBAOH in MeCN). In MeCN without OH^- (pink, solid line) λ_{max} = 555 nm (ε = 160 L mol^{-1} cm^{-1}); with 2.5 equivalents of OH^- (purple dashed line), λ_{max} = 581 nm (ε = 150 L mol^{-1} cm^{-1}); with 5 equivalents OH^- (solid blue line) λ_{max} = 585 nm (ε = 170 L mol^{-1} cm^{-1}).

In aqueous solution, $\mathbf{Co_4P_2W_{18}}$ does not follow simple acid-base behavior. Addition of base results in prolonged pH drift relative to typical pH meter response times, particularly near pH 7. At this pH, the readings are no longer stable or reliable. The nature of this phenomenon is not yet fully clear and is currently under investigation. Interestingly, the presence of MeCN dramatically decreases the drift in pH readings that are observed in pure H_2O and extends the titratable pH range in a concentration-dependent way. Increasing the percentage of MeCN results in a shift in the quantity of OH^- titrant required to achieve the same pH (Figure 4.25). Such behavior is consistent with competitive binding of MeCN to the external Co-centers in aqueous solution, as acetonitrile decreases the percentage of [$\mathbf{Co_4P_2W_{18}}$-OH^-] and therefore allows normal titration to higher pH in the presence of MeCN.

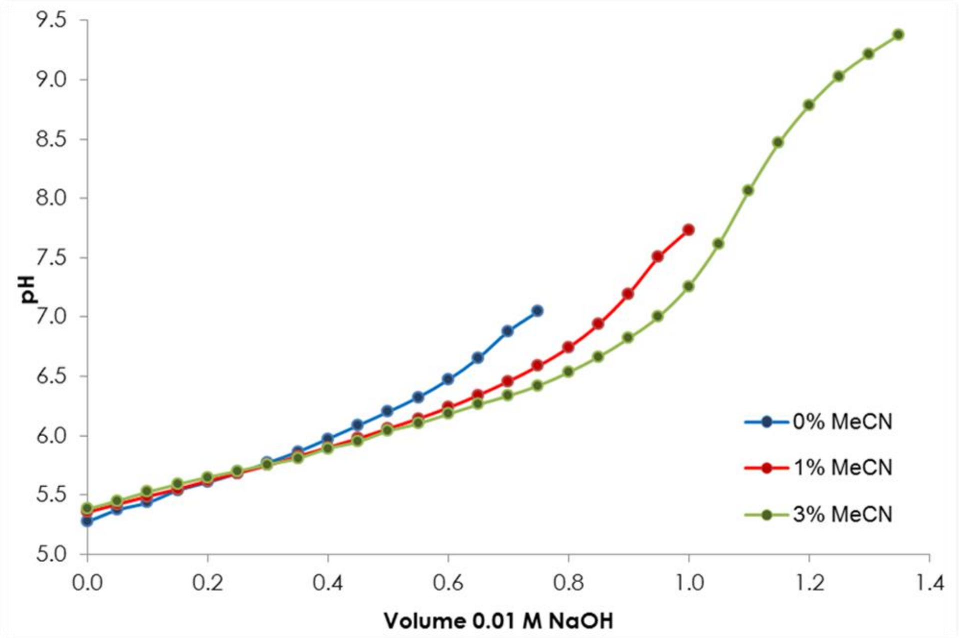

Figure 4.25 Titrations of $Co_4P_2W_{18}$ with 0.01M NaOH in the presence of 0 (blue) 1 (red) and 3 % MeCN (green) in H_2O.

In order to elucidate molecular structure and factors impacting the stability of $[Co_4(MeCN)_2(PW_9O_{34})_2]^{10-}$, **$Co_4P_2W_{18}$**-$(MeCN)_2$, and $[Co_4(H_2O)_2(PW_9O_{34})_2]^{10-}$**,** **$Co_4P_2W_{18}$**-$(H_2O)_2$, DFT calculations were performed on the lowest ferromagnetically coupled ^{13}A-electronic states of these complexes. These calculations show that MeCN ligand coordination to Co in **$Co_4P_2W_{18}$** is 2.1 kcal/mol stronger than for H_2O. Close examination indicates that the stability of **$Co_4P_2W_{18}$**-$(MeCN)_2$, and **$Co_4P_2W_{18}$**-$(H_2O)_2$ is a result of Co-N (or O) and several H-bonding interactions between ligands and the POM tungsten-oxo sites. The calculated O-H distance between the methyl H of MeCN and the tungsten-oxo O is 2.57 Å. The shortest corresponding H-bond observed in the crystal structure is 2.890 Å. The calculated stronger coordination of

MeCN to $\mathbf{Co_4P_2W_{18}}$ compared to a water molecule is in a good agreement with the observation that MeCN effectively competes with water for coordination to the external Co atoms.

4.3.5 Stability and Reactivity of $Co_4V_2W_{18}$ in Solution

It has been well-documented that Co-containing POMs are unstable towards certain buffer anions. This phenomenon is particularly notable in phosphate buffer, where strong complexation of Co by phosphate buffer anions results in a shift of speciation of Co(II) complexes and could lead to decomposition of $\mathbf{Co_4P_2W_{18}}$ [92]. The isostructural $\mathbf{Co_4V_2W_{18}}$ system is both more active (TON, TOF) and less stable than $\mathbf{Co_4P_2W_{18}}$.

The sustained applied potentials intrinsic to the use of electrochemical methods also affect the observed stability of a POM system and frequently lead to POM decomposition. Therefore, observations made through electrochemical methods are not always an accurate reflection of system stability or reactivity under non-electrochemical conditions. Chelating reagents, such as dimethylglyoxime (DMG) or 2,2’-bipyridine (bpy), have been used in conjunction with adsorptive cathodic stripping to quantify and sequester $Co(II)_{aq}$ in solution, including studies of $\mathbf{Co_4P_2W_{18}}$. However, the significantly lower relative stability of $\mathbf{Co_4V_2W_{18}}$ is reflected in its reactivity towards DMG and bpy. These complexing agents may perturb the speciation of $\mathbf{Co_4V_2W_{18}}$ by coordinating Co(II) atoms in the POM and increasing rates of decomposition.

To examine the applicability if these methods in the V system, the reaction between $\mathbf{Co_4V_2W_{18}}$ and DMG was studied using stopped-flow kinetics. The exemplary kinetic curves, are shown in Figure 4.26. Addition of DMG to $\mathbf{Co_4V_2W_{18}}$ results in changes in the spectrum in less than 0.1 s, suggesting rapid complexation with Co centers of the POM. Subsequent changes in the spectrum are associated with decomposition of **$Co_4V_2W_{18}$**. Therefore, an adsorptive cathodic stripping procedure used to quantify free Co(II)$_{aq}$ in the presence of **$Co_4V_2W_{18}$** in borate buffer at pH 9.0 is problematic.

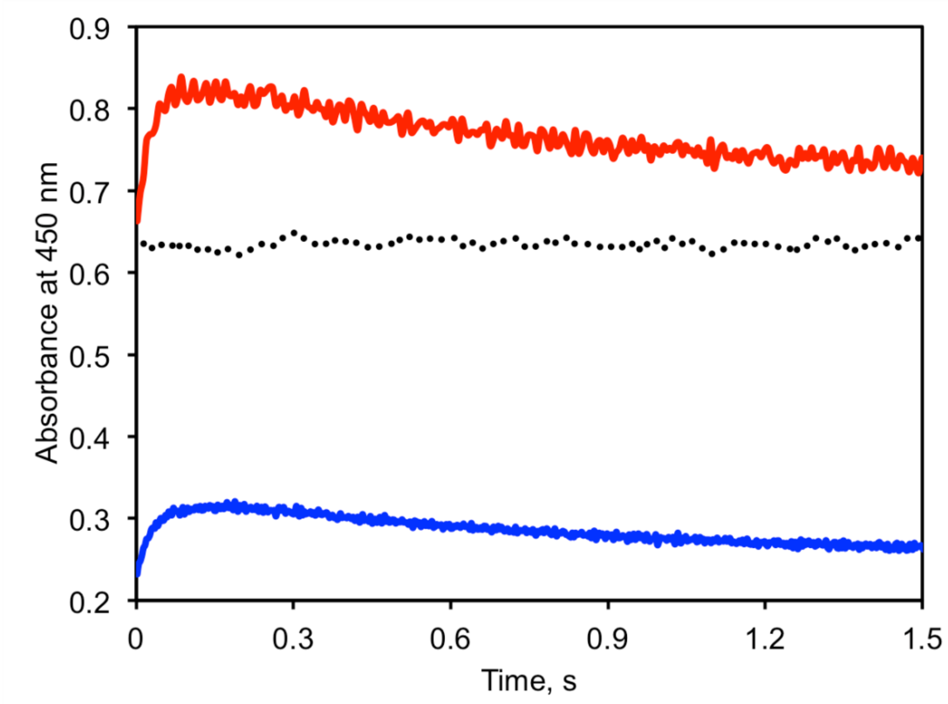

Figure 4.26. The dependence of absorbance at 450 nm versus time after mixing 0.25 (blue) or 1.0 (red) mM $Co_4V_2W_{18}$ in water and 1.0 mM DMG in 180 mM NaB buffer (pH 9.0). The dashed line is after mixing of 1.0 M $Co_4V_2W_{18}$ with 180 mM NaB buffer (pH9.0). The dashed line is after mixing of 1.0 M $Co_4V_2W_{18}$ with 180 mM NaB buffer (pH 9.0).

Instantaneous mixing of the POM with bpy results in reduced light-driven water oxidation activity as seen in Figure 4.27 (a), but with aging together in buffer, the activity is slightly restored to the formation of a new complex and possibly excess Co(II)$_{aq}$ from the decomposition of the POM as shown in Figure 4.27 (b).

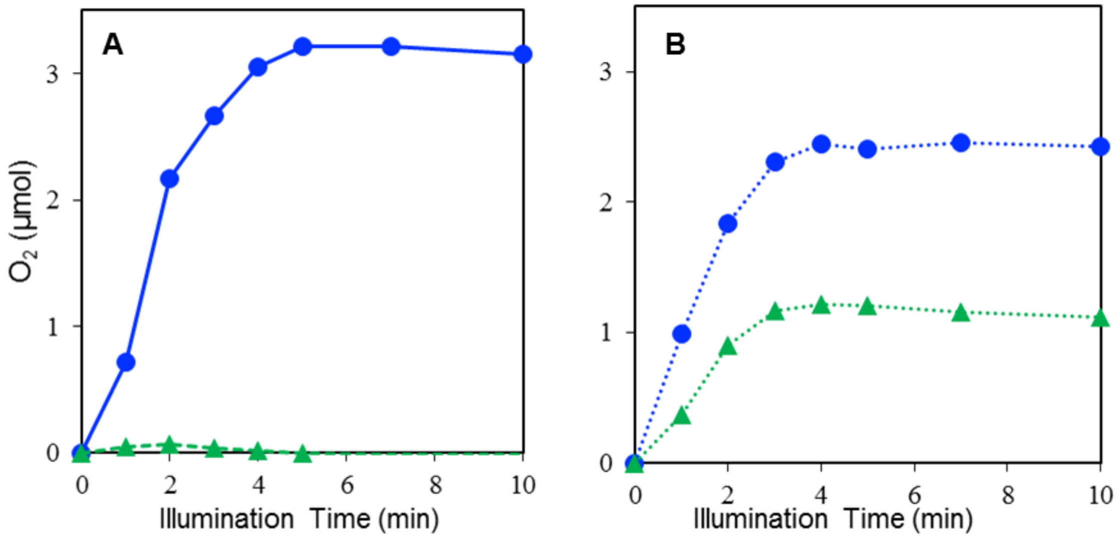

Figure 4.27. Light-driven water oxidation oxygen measurements of $Co_4V_2W_{18}$ (blue circles) and $Co_4V_2W_{18}$ mixed with 1 equivalent of bpy per Co atom (a) with 0 minutes of mixing and (b) aging for 1 hour. Conditions: 2 μM $Co_4V_2W_{18}$ 8 μM of bpy, 1.0 mM $[Ru(bpy)_3]Cl_2$, 5.0 mM $Na_2S_2O_8$, 80 mM sodium borate buffer, pH 9.0.

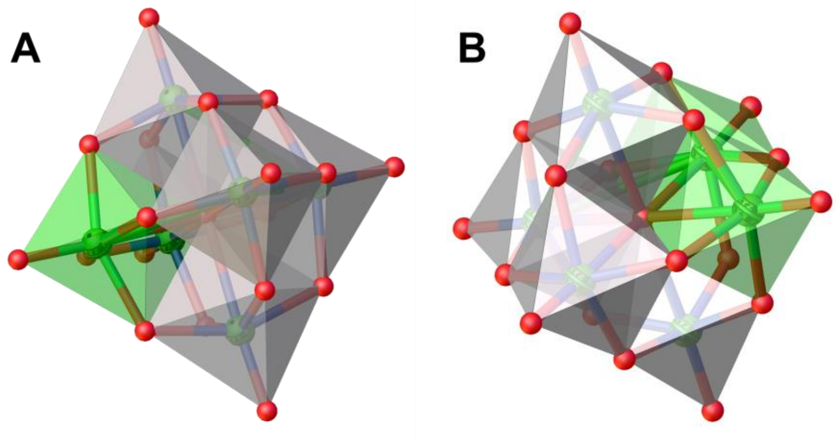

Figure 4.28 X-ray Structures of Lindqvist ions (a) VW_5 and (b) V_2W_4 formed as side-products in synthesis and decomposition products of $Co_4V_2W_{18}$.

The major decomposition products that could be isolated from solutions of **$Co_4V_2W_{18}$** are the *cis*-$[V_2W_4O_{19}]^{4-}$ and $[VW_5O_{19}]^{3}$ Lindqvist ions, **V_2W_4** and **VW_5** shown in Figure 4.28, which are also observed by ^{51}V NMR. Preliminary X-ray diffraction data for crystals which form from this solution have identified at least one major decomposition product as $(Co(bpy)_3)_2[V_2W_4O_{19}]$ (Figure 4.29). The **VW_5** and **V_2W_4** decomposition products, like $Co(bpy)_3^{2+}$, are catalytically inactive as shown in Figure 4.30.

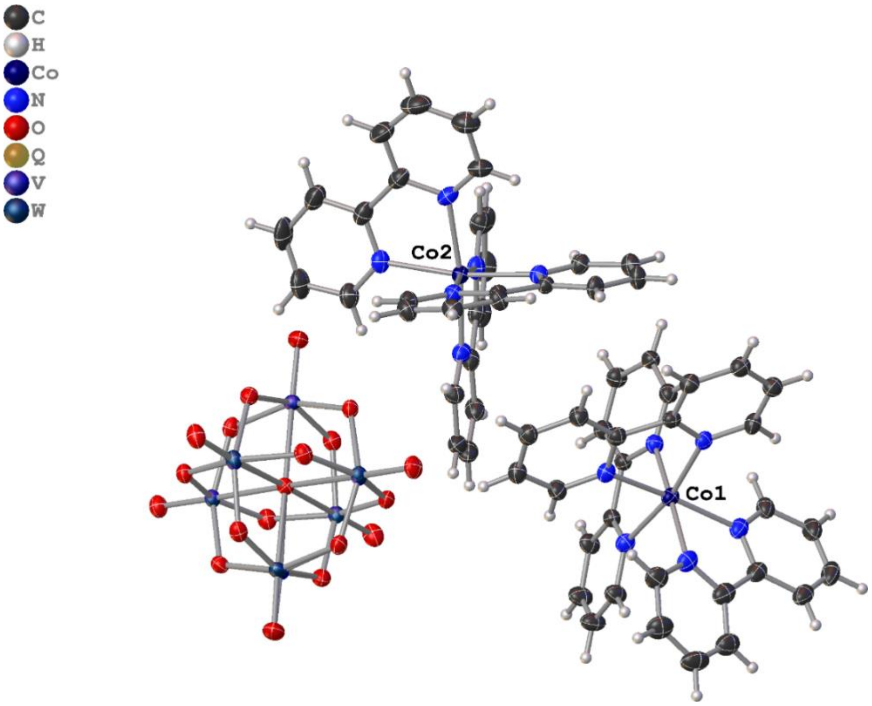

Figure 4.29. Structure of the major product of decomposition of $Co_4V_2W_{18}$ with 2,2'-bipyridine in borate buffer at pH 9.

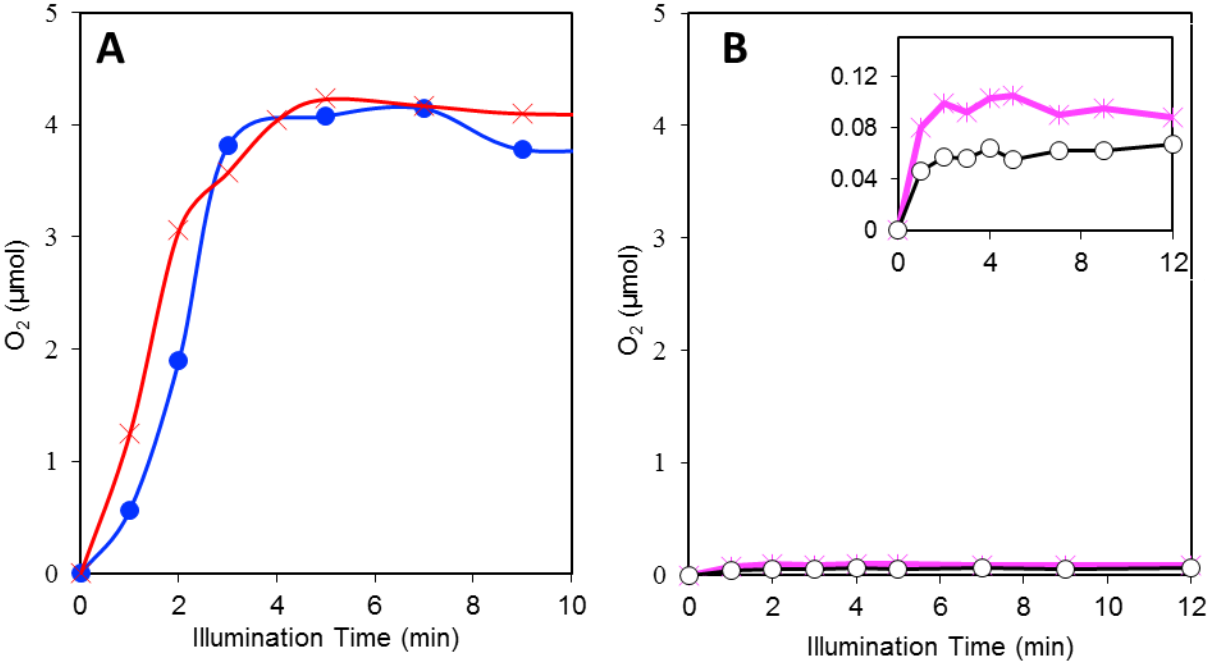

Figure 4.30. Light-driven oxygen measurements for (a) $Co_4V_2W_{18}$ (blue circles) and with aging for 2 hours (red x's) and (b) cis-$[V_2W_4O_{19}]^{4-}$ (magenta stars) and $[VW_5O_{19}]^{3-}$ (black open circles). Inset shows zoomed in oxygen measurements. Conditions: 8 µM POM, 1.0 mM $[Ru(bpy)_3]Cl_2$, 5.0 mM $Na_2S_2O_8$, 80 mM sodium borate buffer, pH 9.

The large formation constants of **VW_5** and **V_2W_4** are major contributors to this instability observed with **$Co_4V_2W_{18}$** in the presence of ligands that coordinate Co(II), such as bpy and DMG. In the conversion of Na salts of the POMs, bromide ion is introduced into the solution. UV-Vis and suggests the formation of $CoBr_4^{2-}$ anions even in organic solvents with preliminary XRD showing **V_2W_4** and **VW_5** (figure 4.28) with a contamination of Co(II) counterions. Therefore some of the data regarding bpy are inconclusive as to what the catalytically active species that forms with aging may be. In addition to being isolated in higher yields as its hydrophobic salt, **$Co_4P_2W_{18}$** does not shows similar signs of decomposition in the presence of coordinating ligands. Although **$Co_4P_2W_{18}$** was isolable as its methylamine and DMF adducts (shown in Figure

4.31) this is not true for **$Co_4V_2W_{18}$** which shows a different UV-Vis spectrum in DMF, shown in Figure 4.32, which resembles **$Co_4P_2W_{18}$** when titrated with OH^-, suggesting that even DMF (or possibly $MeNH_2$ that forms in DMF) lead to ligand dissociation.

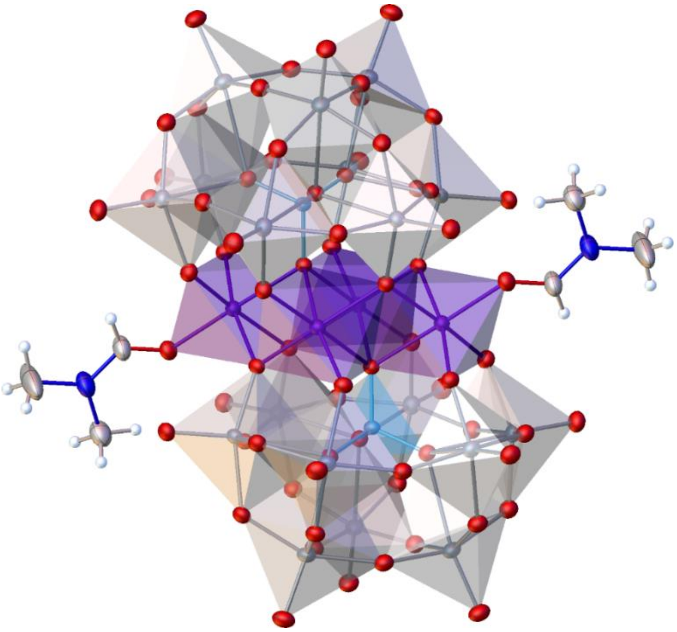

Figure 4.31 X-ray crystal structure of the $(DMF)_2Co_4P_2W_{18}$ derivative with N-coordination of DMF solvent molecules. DMF binding was not observed in the vanadium analogue.

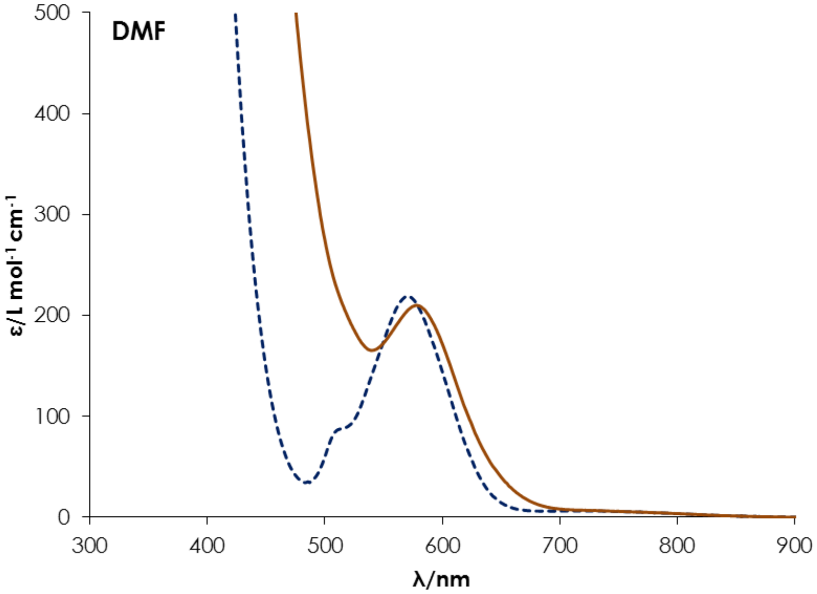

Figure 4.32. UV-Vis spectra of $Co_4V_2W_{18}$ (solid brown line) and $Co_4P_2W_{18}$ (blue dashed line) in DMF.

4.3.6 Electrochemical Stability of Co_4POMs in Anhydrous Media

Although the V analogue of the Co_4POM WOCs is reportedly much faster than the P analogue, its instability is problematic as clearly demonstrated by its susceptibility towards decomposition under various conditions that are often employed in WOC studies. Therefore, no clear explanation for the difference in reactivity has been established. Electrochemistry was shown to be effective in MeCN although the coordination of solvent appeared to significantly change the redox potentials and reactivity relative to H_2O coordination. Furthermore the difficulty in maintaining anhydrous conditions limited the extent of experiments in this solvent due to decomposition at the electrode surface. Therefore, electrochemistry was carried out in anhydrous non-coordinating DCE solvent with $TBAPF_6$ as supporting electrolyte. The cyclic voltammogram for **$Co_4P_2W_{18}$** is shown in Figure 4.33 and exhibits three events, one 2-electron event at +856 mV and two 1-electron events at +1188 and +1480 with a reduction wave appearing at +1320 mV on the reverse scan. This is in contrast to the cyclic voltammogram for **$Co_4V_2W_{18}$,** shown in Figure 4.34, which features four single-electron events. The first three are separated by ~300 mV while the final potential of +1426 mV approximately 200 mV beyond the third. The first event at +576 mV is nearly 300 mV lower than the first potential for and this may be related to a difference in protonation state, as similar splitting of multi-electron peaks was observed in MeCN in the presence of base.

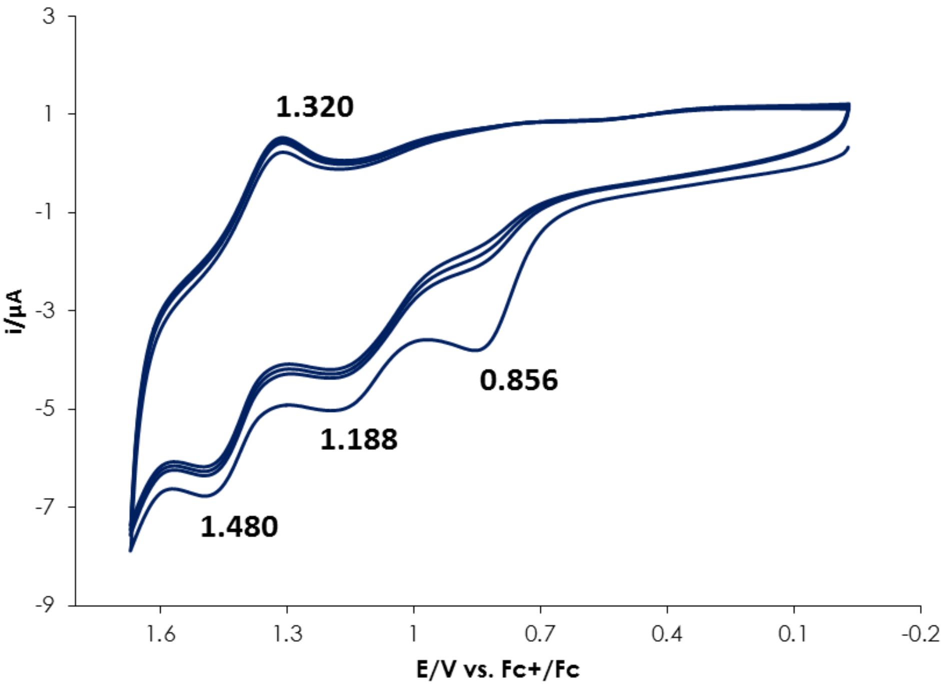

Figure 4.33 Cyclic voltammetry of $Co_4V_2W_{18}$ in anhydrous DCE. Conditions: 1 mM POM, 0.1 M $TBAPF_6$, scan rate = 50 mV/s

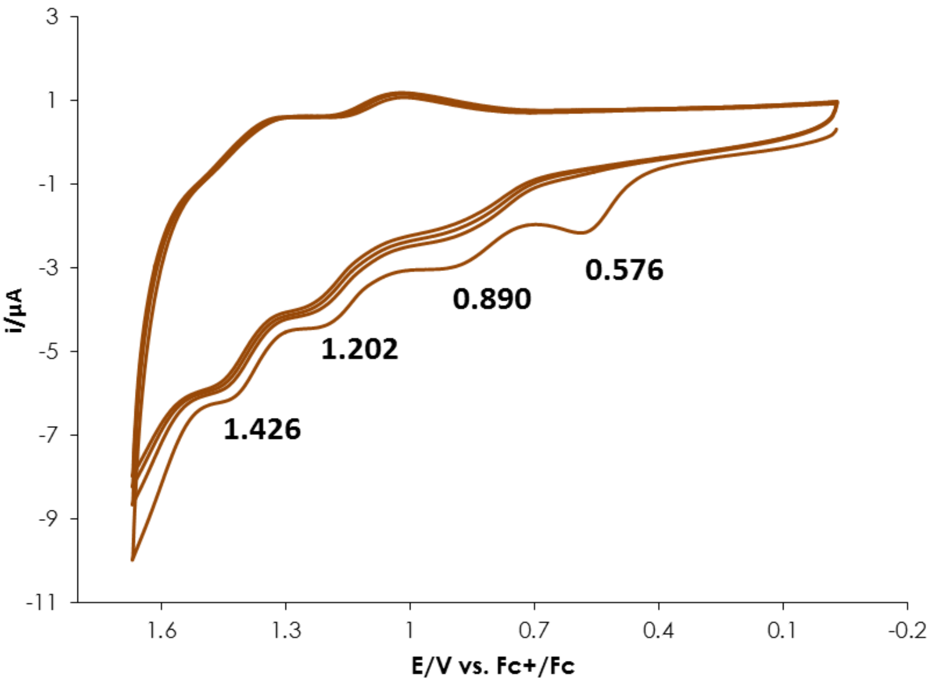

Figure 4.34 Cyclic voltammetry of $Co_4V_2W_{18}$ in anhydrous DCE. Conditions: 1 mM POM, 0.1 M $TBAPF_6$, scan rate = 50 mV/s

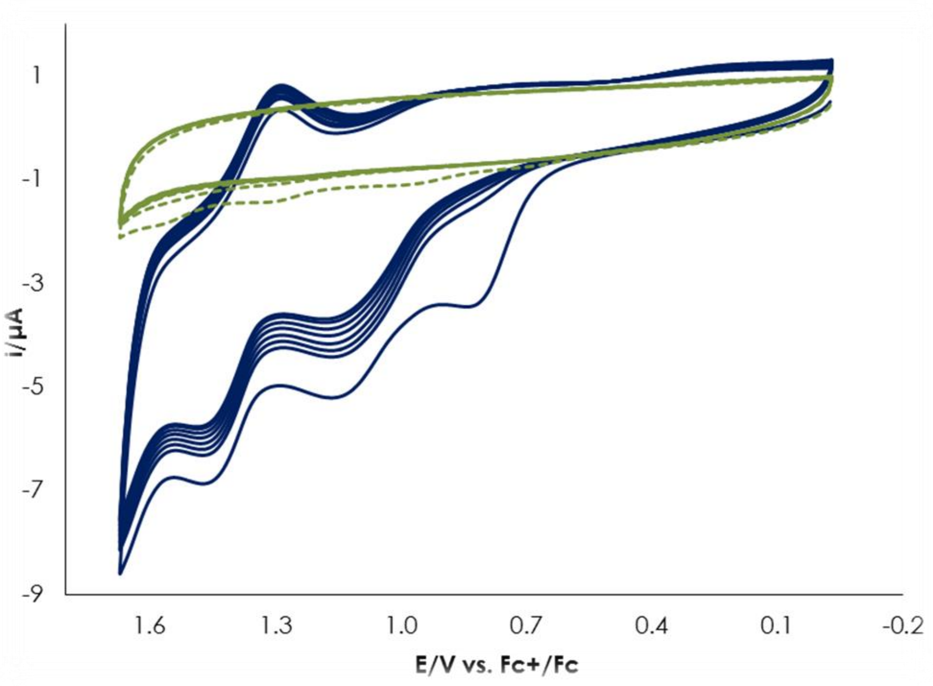

Figure 4.35 Electrochemical film formation on glassy carbon from $Co_4P_2W_{18}$ in anhydrous DCE.

Conditions: 1 mM POM, 0.1 M $TBAPF_6$, scan rate = 50 mV/s

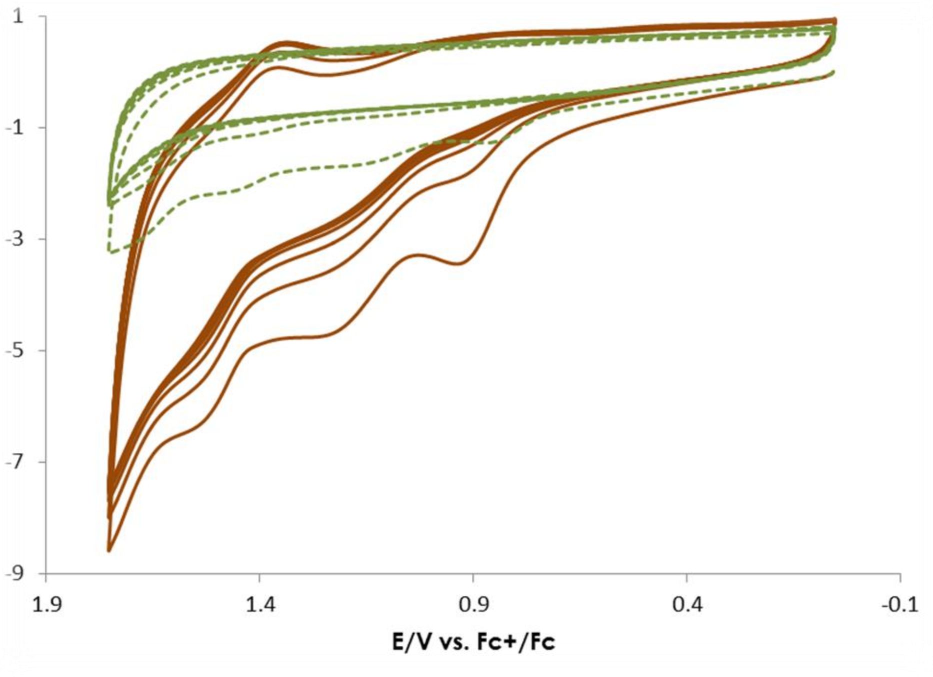

Figure 4.36 Electrochemical film formation on glassy carbon from $Co_4V_2W_{18}$ in anhydrous DCE. Conditions: 1 mM POM, 0.1 M $TBAPF_6$, scan rate = 50 mV/s

In previous cases where decomposition of CoPOMs to form CoO_x has been suspected, the use of SEM-EDX to analyze the surface composition has proven valuable. In the formation of CoO_x, SEM-EDX shows only Co signatures, with the complete lack of W indicating no POM was intact. SEM-EDX was employed here to establish whether the film formed on the glassy carbon electrode surfaces corresponds to the POM or if there is significant decomposition to the oxide. Examination of the images shows no particle formation and instead a smooth film is visible as shown in Figure 4.37. EDX analysis shows the overlapping W and Co signatures, as well as V for **$Co_4V_2W_{18}$** The observed W/V and W/Co atomic weight ratios of 30.98 and 14.00 correspond well to the expected values (32 and 14.03, respectively) for **$Co_4V_2W_{18}$**; the observed W/Co ratio of 15.00 for **$Co_4P_2W_{18}$,** is also in good agreement with the predicted value but W/P or Co/P measurements are obscured by the excess P from PF_6 electrolyte employed for cyclic voltammetry.

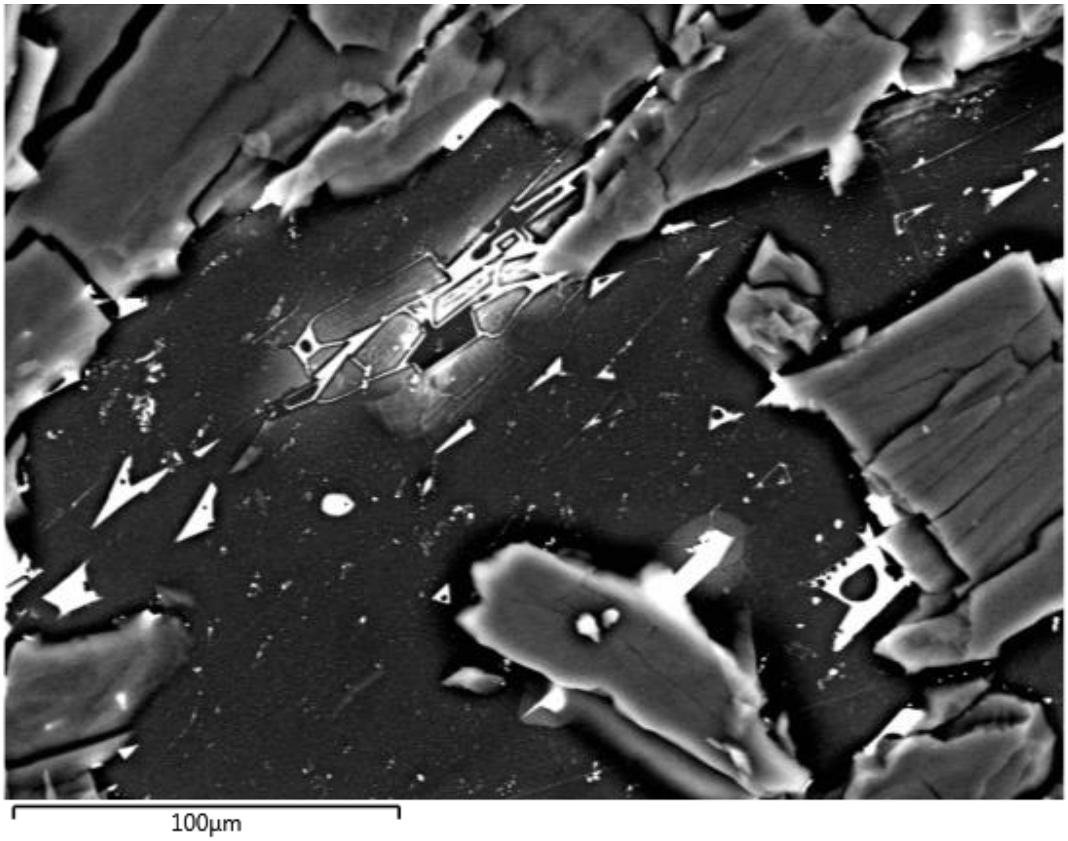

Figure 4.37 Scanning electron microscopy image of film formed on glassy carbon from $Co_4P_2W_{18}$ in anhydrous DCE.

This suggests the POM is largely intact as opposed to decomposition to CoO_x or other W or V oxide species. The ratios are in good agreement with the stoichiometry of the parent POM. Therefore, these studies show that under these electrochemical conditions, **$Co_4P_2W_{18}$** and **$Co_4V_2W_{18}$** are most likely remaining intact and adsorbing onto the glassy carbon surface. The disappearance of the first oxidation event on multiple cycles may indicate deprotonation upon oxidation, which results in adsorption and a decrease in the redox potential. Thus, upon reversal, the reduction is not observed which would be consistent in the absence of a proton source.

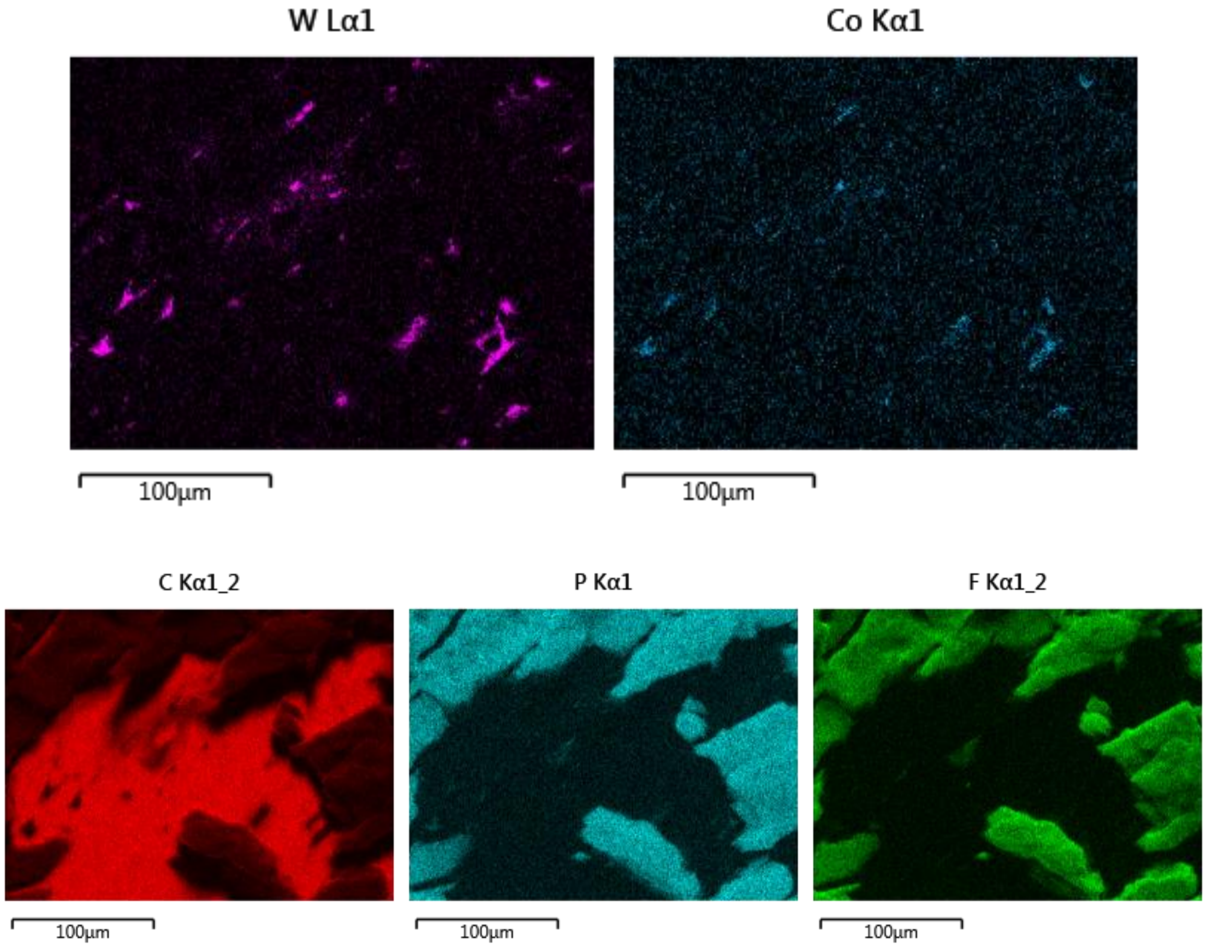

Figure 4.38 *Elemental mapping of glassy carbon electrode surface from scanning electron microscopy image of film formed on glassy carbon from* $\mathbf{Co_4P_2W_{18}}$.

The slower rate of desorption of $\mathbf{Co_4V_2W_{18}}$ may be related to protonation state. The change in the voltammogram for $\mathbf{Co_4V_2W_{18}}$ over time suggests that the POM undergoes a slow structural equilibration once dissolved into solution. However the strong resemblance to the $\mathbf{Co_4P_2W_{18}}$ suggests these structures are similar if not identical in solution. Similar dependencies on aging time have been observed in aqueous media and are currently the subject of intense studies.

4.4 Conclusions

Co-based POMs are promising as homogeneous, molecular WOCs, but suffer from hydrolytic instability that renders detailed studies under catalytic conditions difficult, and little is known about the water oxidation mechanism by CoPOM WOCs **$Co_4P_2W_{18}$** and **$Co_4V_2W_{18}$** in bulk water. In Nature, on the other hand, water oxidation occurs at the OEC in an isolated hydrophobic protein environment, and X-ray crystallographic studies of the OEC have led to significant advances in mechanistic understanding of this important reaction center by elucidating different protonation states of the active site. In these studies, solution state and solid state X-ray diffraction studies reveal significant insights into the stability and reactivity of the isostructural **$Co_4P_2W_{18}$** and **$Co_4V_2W_{18}$** POM WOCs. Differences between the stability of these compounds are evident in aqueous media, and significant differences in stability were also revealed in organic media.

(I) A fast, efficient and high-yielding method for the synthesis of and **$Co_4V_2W_{18}$** was developed and the purity established by ^{51}V NMR. Conversion of alkali metal salts of **$Co_4P_2W_{18}$** and **$Co_4V_2W_{18}$** polyoxoanions to their hydrophobic, TBA salts was employed to study these POM WOCs in conditions where their hydrolytic instability was significantly diminished and reactivity could be better controlled. In MeCN,

$Co_4V_2W_{18}$ is indefinitely stable and showed no signs of decomposition compared to ~30% decomposition in H_2O.

(II) In organic solvent MeCN **$Co_4P_2W_{18}$** shows reversible oxidation of Co(II) to generate Co(III) in one 2-electron step, which shifts to lower potential and splits into two 1-electron couples in the presence of base, indicating proton-coupled electron transfer. The presence of aqueous hydroxide in excess leads to a catalytic wave and decomposition on glassy carbon, indicating likely CoO_x deposition as in aqueous media. One additional 2-electron redox couple is observed for a total of 4-electron oxidation. However, no dioxygen is observed under electrochemical or chemical oxidation conditions in MeCN. The inhibition of oxygen evolution by 1-3% MeCN in H_2O indicates that binding to the external Co(II), which was confirmed in the solid and solution state, competitively inhibits O_2 formation. This provides two possible interpretations into the mechanism of water oxidation, either that binding at this position either blocks coordination of substrate water or that reaction with MeCN proceeds more quickly than reaction with water to form O_2.

(III) In anhydrous solvent like DCE, distinct and rich electrochemistry was discovered that had never before been explored. The data suggest that **$Co_4V_2W_{18}$** undergoes a slow equilibration or structural change in solution over time to resemble that **$Co_4P_2W_{18}$**. After this stage, the CVs are indistinguishable. Prior to this stage, the first 2-electron oxidation occurs at a potential that is ~300 mV lower and appears to be proton-dependent. The disappearance of the initial event in both cases suggests proton-coupled electron transfer following the fir two Co(II) to Co(III) events. This deprotonation appears to be the first step in adsorption to form a film on the glassy carbon surface. The film dissolves in the absence of applied potentials, and SEM-EDX shows atomic ratios in agreement with the POMs remaining intact. Therefore, these results show that electrochemical studies of these POMs are indeed possible and show extremely interesting potential for better understanding the properties, stability, and mechanism in the POM WOCs.

4.5 References

1. Crabtree, R. H., Deactivation in Homogeneous Transition Metal Catalysis: Causes, Avoidance, and Cure. *Chem. Rev.* **2015,** *115* (1), 127-150.

2. Shu, L.; Nesheim, J. C.; Kauffmann, K.; Münck, E.; Lipscomb, J. D.; Que, L., An Fe2IVO2 Diamond Core Structure for the Key Intermediate Q of Methane Monooxygenase. *Science* **1997,** *275* (5299), 515-518.

3. Denisov, I. G.; Makris, T. M.; Sligar, S. G.; Schlichting, I., Structure and Chemistry of Cytochrome P450. *Chem. Rev.* **2005,** *105* (6), 2253-2278.

4. Jerina, D. M.; Kaubisch, N.; Daly, J. W., Arene Oxides as Intermediates in the Metabolism of Aromatic Substrates: Alkyl and Oxygen Migrations during Isomerization of Alkylated Arene Oxides. *Proc. Natl. Acad. Sci. U. S. A.* **1971,** *68* (10), 2545-2548.

5. Winterbourn, C. C., Toxicity of iron and hydrogen peroxide: the Fenton reaction. *Toxicol. Lett.* **1995,** *82*, 969-974.

6. Rappaport, F.; Guergova-Kuras, M.; Nixon, P. J.; Diner, B. A.; Lavergne, J., Kinetics and Pathways of Charge Recombination in Photosystem II. *Biochemistry* **2002,** *41* (26), 8518-8527.

7. Yano, J.; Yachandra, V., Mn(4)Ca Cluster in Photosynthesis: Where and How Water is Oxidized to Dioxygen. *Chem. Rev.* **2014,** *114* (8), 4175-4205.

8. Suga, M.; Akita, F.; Hirata, K.; Ueno, G.; Murakami, H.; Nakajima, Y.; Shimizu, T.; Yamashita, K.; Yamamoto, M.; Ago, H.; Shen, J.-R., Native structure of photosystem II at 1.95 A resolution viewed by femtosecond X-ray pulses. *Nature* **2015,** *517* (7532), 99-103.

9. (a) Harriman, A.; Pickering, I. J.; Thomas, J. M.; Christensen, P. A., Metal Oxides as Heterogeneous Catalysts for Oxygen Evolution under Photochemical Conditions. *J. Chem. Soc., Faraday Trans. 1 F* **1988,** *84* (8), 2795-2806; (b) Harriman, A.; Richoux, M.-C.; Christensen, P. A.; Mosseri, S.; Neta, P., Redox Reactions with Colloidal Metal Oxides: Comparison of Radiation-generated and Chemically generated RuO_2•$2H_2O$ and MnO_2 Colloids. *J. Chem. Soc., Faraday Trans. 1 F* **1987,** *83* (9), 3001-3014.

10. Chen, X.; Chen, G.; Yue, P. L., Stable Ti/IrOx−Sb2O5−SnO2 Anode for O2 Evolution with Low Ir Content. *J. Phys. Chem. B* **2001,** *105* (20), 4623-4628.

11. (a) McCrory, C. C. L.; Jung, S.; Ferrer, I. M.; Chatman, S. M.; Peters, J. C.; Jaramillo, T. F., Benchmarking Hydrogen Evolving Reaction and Oxygen Evolving Reaction Electrocatalysts for Solar Water Splitting Devices. *J. Am. Chem. Soc* **2015,** *137*, 4347-4357; (b) Gerken, J. B.; McAlpin, J. G.; Chen, J. Y. C.; Rigsby, M. L.; Casey, W. H.; Britt, R. D.; Stahl, S. S., Electrochemical Water Oxidation with Cobalt-Based Electrocatalysts from pH 014: The Thermodynamic Basis for Catalyst Structure, Stability, and Activity. *J. Am. Chem. Soc.* **2011,** *133*, 14431-14442; (c) Blakemore, J. D.; Gray, H. B.; Winkler, J. R.; Müller, A. M., Co3O4 Nanoparticle Water-Oxidation

Catalysts Made by Pulsed-Laser Ablation in Liquids. *ACS Catal.* **2013,** *3* (11), 2497-2500; (d) Hunter, B. M.; Blakemore, J. D.; Deimund, M.; Gray, H. B.; Winkler, J. R.; Müller, A. M., Highly Active Mixed-Metal Nanosheet Water Oxidation Catalysts Made by Pulsed-Laser Ablation in Liquids. *J. Am. Chem. Soc.* **2014,** *136* (38), 13118-13121.

12. (a) Surendranath, Y.; Lutterman, D. A.; Liu, Y.; Nocera, D. G., Nucleation, Growth, and Repair of a Cobalt-Based Oxygen Evolving Catalyst. *J. Am. Chem. Soc.* **2012,** *134* (14), 6326-6336; (b) Nocera, D. G., The Artificial Leaf. *Acc. Chem. Res.* **2012,** *45* (5), 767-776; (c) Surendranath, Y.; Kanan, M. W.; Nocera, D. G., Mechanistic Studies of the Oxygen Evolution Reaction by a Cobalt-Phosphate Catalyst at Neutral pH. *J. Am. Chem. Soc.* **2010,** *132*, 16501-16509; (d) Surendranath, Y.; Dincă, M.; Nocera, D. G., Electrolyte-Dependent Electrosynthesis and Activity of Cobalt-Based Water Oxidation Catalysts

J. Am. Chem. Soc. **2009,** *131*, 2615-2620; (e) Lutterman, D. A.; Surendranath, Y.; Nocera, D. G., A Self-Healing Oxygen-Evolving Catalyst. *J. Am. Chem. Soc.* **2009,** *131*, 3838-3839; (f) Kanan, M. W.; Surendranath, Y.; Nocera, D. G., Cobalt–phosphate oxygen-evolving compound. *Chem. Soc. Rev.* **2009,** *38*, 109-114.

13. (a) Gersten, S. W.; Samuels, G. J.; Meyer, T. J., Catalytic Oxidation of Water by an Oxo-Bridged Ruthenium Dimer. *J. Am. Chem. Soc.* **1982,** *104*, 4029-4030; (b) Gilbert, J. A.; Eggleston, D. S.; Wyatt R. Murphy, J.; Geselowitz, D. A.; Gersten, S. W.; Hodgson, D. J.; Meyer, T. J., Structure and Redox Properties of the Water-Oxidation Catalyst $[(bpy)_2(OH_2)RuORu(OH_2)(bpy)_2]^{4+}$. *J. Am. Chem. Soc.* **1985,** *107* (13), 3855-3864; (c) Clark, A. E.; Hurst, J. K., Mechanisms of Water Oxidation Catalyzed by Ruthenium Coordination Complexes. In *Prog. Inorg. Chem.*, John Wiley & Sons, Inc.: 2011; pp 1-54.

14. Romain, S.; Bozoglian, F.; Sala, X.; Llobet, A., Oxygen—Oxygen Bond Formation by the Ru-Hbpp Water Oxidation Catalyst Occurs Solely via an Intramolecular Reaction Pathway. *J. Am. Chem. Soc.* **2009,** *131*, 2768-2769.

15. Limburg, B.; Bouwman, E.; Bonnet, S., Molecular water oxidation catalysts based on transition metals and their decomposition pathways. *Coord. Chem. Rev.* **2012,** *256* (15–16), 1451-1467.

16. Francàs, L.; Sala, X.; Escudero-Ad————————————án, E.; Benet-Buchholz, J.; Escriche, L.; Llobet, A., Synthesis, Structure, and Reactivity of New Tetranuclear Ru-Hbpp-Based Water-Oxidation Catalysts. *Chem. Commun.* **2011,** *50*, 2771-2781.

17. Kärkäs, M. D.; Åkermark, T.; Johnston, E. V.; Karim, S. R.; Laine, T. M.; Lee, B.-L.; Åkermark, T.; Privalov, T.; Åkermark, B., Water Oxidation by Single-Site Ruthenium Complexes: Using Ligands as Redox and Proton Transfer Mediators. *Angew. Chem. Int. Ed.* **2012,** *51* (46), 11589-11593.

18. Carrell, T. G.; Cohen, S.; Dismukes, G. C., Oxidative catalysis by $Mn_4O_{46}^+$ cubane complexes. *J. Mol. Catal. A: Chem.* **2002,** *187* (1), 3-15.

19. (a) McCool, N. S.; Robinson, D. M.; Sheats, J. E.; Dismukes, G. C., A Co_4O_4 “Cubane” Water Oxidation Catalyst Inspired by Photosynthesis. *J. Am. Chem. Soc.* **2011,** *133*, 11446-11449; (b) Berardi, S.; Ganga, G. L.; Natali, M.; Bazzan, I.; Puntoriero, F.; Sartorel, A.; Scandola, F.; Campagna, S.; Bonchio, M., Photocatalytic Water Oxidation: Tuning Light-Induced Electron Transfer by Molecular Co_4O_4 Cores. *J. Am. Chem. Soc.* **2012,** *134*, 11104-11107; (c) Genoni, A.; La Ganga, G.; Volpe, A.; Puntoriero, F.; Di Valentin, M.; Bonchio, M.; Natali, M.; Sartorel, A., FDPHOTOC15:

Water oxidation catalysis upon evolution of molecular Co(III) cubanes in aqueous media *Faraday Discuss.* **2015**, Published online 10 June 2015.

20. Ullman, A. M.; Liu, Y.; Huynh, M.; Bediako, D. K.; Wang, H.; Anderson, B. L.; Powers, D. C.; Breen, J. J.; Abruña, H. D.; Nocera, D. G., Water Oxidation Catalysis by Co(II) Impurities in $Co(III)_4O_4$ Cubanes. *J. Am. Chem. Soc.* **2014,** *136*, 17681-17688.

21. (a) Nakazono, T.; Parent, A. R.; Sakai, K., Cobalt porphyrins as homogeneous catalysts for water oxidation. *Chem. Commun.* **2013,** *49* (56), 6325-6327; (b) Wang, D.; Groves, J. T., Efficient water oxidation catalyzed by homogeneous cationic cobalt porphyrins with critical roles for the buffer base. *Proc. Natl. Acad. Sci.* **2013,** *110* (39), 15579-15584.

22. Pope, M. T., Polyoxo Anions: Synthesis and Structure. In *Comprehensive Coordination Chemistry II: From Biology to Nanotechnology*, Wedd, A. G., Ed. Elsevier Ltd.: Oxford, UK, 2004; Vol. 4, pp 635-678.

23. (a) Lv, H.; Hill, C. L., Polyoxometalate-Based Multi-Electron-Transfer Catalysts in Solar Fuel Chemistry. *Acc. Chem. Res.* **2015 Proposal to submit to Acc. Chem. Res.**, Proposal submitted Aug 18, 2015; (b) Lv, H.; Geletii, Y. V.; Zhao, C.; Vickers, J. W.; Zhu, G.; Luo, Z.; Song, J.; Lian, T.; Musaev, D. G.; Hill, C. L., Polyoxometalate water oxidation catalysts and the production of green fuel. *Chem. Soc. Rev.* **2012,** *41*, 7572-7589.

24. (a) Sartorel, A.; Carraro, M.; Scorrano, G.; Zorzi, R. D.; Geremia, S.; McDaniel, N. D.; Bernhard, S.; Bonchio, M., Polyoxometalate Embedding of a Tetraruthenium(IV)-oxo-core by Template-Directed Metalation of $[\gamma\text{-}SiW_{10}O_{36}]^{8-}$: A Totally Inorganic Oxygen-Evolving Catalyst. *J. Am. Chem. Soc.* **2008,** *130* (15), 5006-5007; (b) Geletii, Y. V.; Botar, B.; Kögerler, P.; Hillesheim, D. A.; Musaev, D. G.; Hill, C. L., An All-Inorganic, Stable, and Highly Active Tetraruthenium

Homogeneous Catalyst for Water Oxidation. Selected as the VIP Article by the reviewers and editor. *Angew. Chem. Int. Ed.* **2008,** *47*, 3896-3899.

25. Yin, Q.; Tan, J. M.; Besson, C.; Geletii, Y. V.; Musaev, D. G.; Kuznetsov, A. E.; Luo, Z.; Hardcastle, K. I.; Hill, C. L., A fast soluble carbon-free molecular water oxidation catalyst based on abundant metals. *Science* **2010,** *328*, 342-345.

26. Lv, H.; Song, J.; Geletii, Y. V.; Vickers, J. W.; Sumliner, J. M.; Musaev, D. G.; Kögerler, P.; Zhuk, P. F.; Bacsa, J.; Zhu, G.; Hill, C. L., An Exceptionally Fast Homogeneous Carbon-free Cobalt-based Water Oxidation Catalyst. *J. Am. Chem. Soc.* **2014,** *136* (26), 9268-9271.

27. (a) Folkman, S. J.; Finke, R. G., Electrochemical Water Oxidation Catalysis Beginning with Co(II) Polyoxometalates: The Case of the Precatalyst $Co_4V_2W_{18}O_{68}^{10-}$. *ACS Catal.* **ASAP November 23, 2016,** *7*, 7-17; (b) Folkman, S. J.; Kirner, J. T.; Finke, R. G., Cobalt Polyoxometalate $Co_4V_2W_{18}O_{68}^{10-}$: A Critical Investigation of Its Synthesis, Purity, and Observed ^{51}V Quadrupolar NMR. *Inorg. Chem.* **2016,** *55* (11), 5343-5355; (c) Stracke, J. J.; Finke, R. G., Water Oxidation Catalysis Beginning with $Co_4(H_2O)_2(PW_9O_{34})_2^{10-}$ When Driven by the Chemical Oxidant Ruthenium(III)tris(2,2′-bipyridine): Stoichiometry, Kinetic, and Mechanistic Studies en Route to Identifying the True Catalyst. *ACS Catal.* **2014,** *4*, 79-89; (d) Stracke, J. J.; Finke, R. G., Water Oxidation Catalysis Beginning with 2.5 µM [Co4(H2O)2(PW9O34)2]10–: Investigation of the True Electrochemically Driven Catalyst at ≥600 mV Overpotential at a Glassy Carbon Electrode. *ACS Catal.* **2013,** *3* (6), 1209-1219; (e) Stracke, J. J.; Finke, R. G., Electrocatalytic Water Oxidation Beginning with the Cobalt Polyoxometalate $[Co_4(H_2O)_2(PW_9O_{34})_2]^{10-}$: Identification of Heterogeneous CoO_x as the Dominant Catalyst. *J. Am. Chem. Soc.* **2011,** *133*, 14872-14875.

28. Liu, Y.; Ng, S.-M.; Yiu, S.-M.; Lam, W. W. Y.; Wei, X.-G.; Lau, K.-C.; Lau, T.-C., Catalytic Water Oxidation by Ruthenium(II) Quaterpyridine (qpy) Complexes: Evidence for Ruthenium(III) qpy-N,N'''-dioxide as the Real Catalysts. *Angew. Chem. Int. Ed.* **2014,** *53* (52), 14468-14471.

29. Chen, Z.; Concepcion, J. J.; Song, N.; Meyer, T. J., Chloride-assisted catalytic water oxidation. *Chem. Commun.* **2014,** *50*, 8053-8056.

30. Song, N.; Concepcion, J. J.; Binstead, R. A.; Rudd, J. A.; Vannucci, A. K.; Dares, C.; Coggins, M. K.; Meyer, T. J., Base Enhanced Catalytic Water Oxidation by a Carboxylate-Bipyridine Ru(II) Complex. *Proc. Natl. Acad. Sci.* **2015,** *112* (16), 4935-4940.

31. Connor, G. P.; Holland, P. L., Coordination chemistry insights into the role of alkali metal promoters in dinitrogen reduction. *Catal. Today* **2017,** *286*, 21-40.

32. Andersson, I., Catalysis and regulation in Rubisco. *J. Exp. Bot.* **2008,** *59* (7), 1555-1568.

33. Paul, S.; Neese, F.; Pantazis, D. A., Structural models of the biological oxygen-evolving complex: achievements, insights, and challenges for biomimicry. *Green Chem.* **2017**.

34. Matysik, J.; Alia; Nachtegaal, G.; van Gorkom, H. J.; Hoff, A. J.; de Groot, H. J. M., Exploring the Calcium-Binding Site in Photosystem II Membranes by Solid-State 113Cd NMR. *Biochemistry* **2000,** *39* (23), 6751-6755.

35. Yachandra, V. K.; Yano, J., Calcium in the Oxygen-Evolving Complex: Structural and Mechanistic Role Determined by X-ray Spectroscopy. *Journal of photochemistry and photobiology. B, Biology* **2011,** *104* (1-2), 51-59.

36. (a) Pushkar, Y.; Yano, J.; Sauer, K.; Boussac, A.; Yachandra, V. K., Structural changes in the Mn(4)Ca cluster and the mechanism of photosynthetic water splitting. *Proc. Natl. Acad. Sci. U. S. A.* **2008,** *105* (6), 1879-1884; (b) Cinco, R. M.; Holman, K. L. M.; Robblee, J. H.; Yano, J.; Pizarro, S.

A.; Bellacchio, E.; Sauer, K.; Yachandra, V. K., Calcium EXAFS Establishes the Mn-Ca Cluster in the Oxygen-Evolving Complex of Photosystem II(). *Biochemistry* **2002,** *41* (43), 12928-12933; (c) Cinco, R. M.; Robblee, J. H.; Rompel, A.; Fernandez, C.; Yachandra, V. K.; Sauer, K.; Klein, M. P., Strontium EXAFS Reveals the Proximity of Calcium to the Manganese Cluster of Oxygen-Evolving Photosystem II. *The journal of physical chemistry. B* **1998,** *102* (42), 8248-8256; (d) Kim, S. H.; Gregor, W.; Peloquin, J. M.; Brynda, M.; Britt, R. D., Investigation of the Calcium-Binding Site of the Oxygen Evolving Complex of Photosystem II Using 87Sr ESEEM Spectroscopy. *J. Am. Chem. Soc.* **2004,** *126* (23), 7228-7237.

37. Najafpour, M. M.; Ehrenberg, T.; Wiechen, M.; Kurz, P., Calcium Manganese(III) Oxides (CaMn2O4·x H2O) as Biomimetic Oxygen-Evolving Catalysts. *Angew. Chem. Int. Ed.* **2010,** *49* (12), 2233-2237.

38. Bang, S.; Lee, Y.-M.; Hong, S.; Cho, K.-B.; Nishida, Y.; Seo, M. S.; Sarangi, R.; Fukuzumi, S.; Nam, W., Redox-inactive metal ions modulate the reactivity and oxygen release of mononuclear non-haem iron(III)–peroxo complexes. *Nat Chem* **2014,** *6* (10), 934-940.

39. (a) Tsui, E. Y.; Agapie, T., Reduction potentials of heterometallic manganese–oxido cubane complexes modulated by redox-inactive metals. *Proc. Natl. Acad. Sci.* **2013,** *110* (25), 10084-10088; (b) Kanady, J. S.; Tsui, E. Y.; Day, M. W.; Agapie, T., A Synthetic Model of the Mn_3Ca Subsite of the Oxygen-Evolving Complex in Photosystem II. *Science* **2011,** *333*, 733-736; (c) Tsui, E. Y.; Agapie, T., Reduction potentials of heterometallic manganese–oxido cubane complexes modulated by redox-inactive metals. *Proc. Natl. Acad. Sci. U. S. A.* **2013,** *110* (25), 10084-10088.

40. Ortiz de Montellano, P. R., *Cytochrome P450: Structures, Mechanism and Biochemistry*. 2nd ed.; Plenum Press: New York, 1995.

41. Nam, W.; Kim, I.; Kim, Y.; Kim, C., Biomimetic alkane hydroxylation by cobalt() porphyrin complex and -chloroperbenzoic acid. *Chemical Communications* **2001,** (14), 1262-1263.

42. (a) Kanan, M. W.; Nocera, D. G., In Situ Formation of an Oxygen-Evolving Catalyst in Neutral Water Containing Phosphate and Co2+. *Science* **2008,** *321* (5892), 1072-1075; (b) Nocera, D. G., The Artificial Leaf. *Accounts of Chemical Research* **2012,** *45* (5), 767-776; (c) Betley, T. A.; Surendranath, Y.; Childress, M. V.; Alliger, G. E.; Fu, R.; Cummins, C. C.; Nocera, D. G., A ligand field chemistry of oxygen generation by the oxygen-evolving complex and synthetic active sites. *Philosophical Transactions of the Royal Society B: Biological Sciences* **2008,** *363* (1494), 1293-1303.

43. Yin, Q.; Tan, J. M.; Besson, C.; Geletii, Y. V.; Musaev, D. G.; Kuznetsov, A. E.; Luo, Z.; Hardcastle, K. I.; Hill, C. L., A Fast Soluble Carbon-Free Molecular Water Oxidation Catalyst Based on Abundant Metals. *Science* **2010,** *328* (5976), 342-345.

44. Saouma, C. T.; Peters, J. C., ME and ME complexes of iron and cobalt that emphasize three-fold symmetry (E = O, N, NR). *Coordination Chemistry Reviews* **2011,** *255* (7–8), 920-937.

45. Winkler, J. R.; Gray, H. B., Electronic structures of oxo-metal ions. *Struct. Bonding (Berlin, Ger.)* **2012,** *142* (Copyright (C) 2012 American Chemical Society (ACS). All Rights Reserved.), 17-28.

46. Egan, J. W.; Haggerty, B. S.; Rheingold, A. L.; Sendlinger, S. C.; Theopold, K. H., Crystal structure of a side-on superoxo complex of cobalt and hydrogen abstraction by a reactive terminal oxo ligand. *Journal of the American Chemical Society* **1990,** *112* (6), 2445-2446.

47. Hu, X.; Meyer, K., Terminal Cobalt(III) Imido Complexes Supported by Tris(Carbene) Ligands: Imido Insertion into the Cobalt−Carbene Bond. *Journal of the American Chemical Society* **2004,** *126* (50), 16322-16323.

48. Bigi, J. P.; Harman, W. H.; Lassalle-Kaiser, B.; Robles, D. M.; Stich, T. A.; Yano, J.; Britt, R. D.; Chang, C. J., A High-Spin Iron(IV)–Oxo Complex Supported by a Trigonal Nonheme Pyrrolide Platform. *Journal of the American Chemical Society* **2012,** *134* (3), 1536-1542.

49. Lacy, D. C.; Park, Y. J.; Ziller, J. W.; Yano, J.; Borovik, A. S., Assembly and Properties of Heterobimetallic Co(II/III)/Ca(II) Complexes with Aquo and Hydroxo Ligands. *J. Am. Chem. Soc.* **2012,** *134* (42), 17526-17535.

50. Park, Y. J.; Ziller, J. W.; Borovik, A. S., The effects of redox-inactive metal ions on the activation of dioxygen: isolation and characterization of a heterobimetallic complex containing a Mn(III)-(mu-OH)-Ca(II) core. *J. Am. Chem. Soc.* **2011,** *133* (24), 9258-61.

51. (a) Collins, T. J.; Gordon-Wylie, S. W., A manganese(V)-oxo complex. *Journal of the American Chemical Society* **1989,** *111* (12), 4511-4513; (b) Collins, T. J.; Powell, R. D.; Slebodnick, C.; Uffelman, E. S., A water-stable manganese(V)-oxo complex: definitive assignment of a .nu.Mnv.tplbond.O infrared vibration. *Journal of the American Chemical Society* **1990,** *112* (2), 899-901; (c) MacDonnell, F. M.; Fackler, N. L. P.; Stern, C.; O'Halloran, T. V., Air Oxidation of a Five-Coordinate Mn(III) Dimer to a High-Valent Oxomanganese(V) Complex. *Journal of the American Chemical Society* **1994,** *116* (16), 7431-7432; (d) Shirin, Z.; Hammes, B. S.; Young, V. G.; Borovik, A. S., Hydrogen Bonding in Metal Oxo Complexes: Synthesis and Structure of a Monomeric Manganese(III)−Oxo Complex and Its Hydroxo Analogue. *Journal of the American Chemical Society* **2000,** *122* (8), 1836-1837.

52. (a) McDonald, A. R.; Que Jr, L., High-valent nonheme iron-oxo complexes: Synthesis, structure, and spectroscopy. *Coordination Chemistry Reviews* (0); (b) Rohde, J.-U.; In, J.-H.; Lim, M. H.; Brennessel, W. W.; Bukowski, M. R.; Stubna, A.; Münck, E.; Nam, W.; Que, L., Crystallographic and Spectroscopic Characterization of a Nonheme Fe(IV)=O Complex. *Science* **2003,** *299* (5609), 1037-1039.

53. Pfaff, F. F.; Kundu, S.; Risch, M.; Pandian, S.; Heims, F.; Pryjomska-Ray, I.; Haack, P.; Metzinger, R.; Bill, E.; Dau, H.; Comba, P.; Ray, K., An Oxocobalt(IV) Complex Stabilized by Lewis Acid Interactions with Scandium(III) Ions. *Angew. Chem. Int. Ed.* **2011,** *50* (7), 1711-1715.

54. Hu, X.; Meyer, K., New tripodal N-heterocyclic carbene chelators for small molecule activation. *Journal of Organometallic Chemistry* **2005,** *690* (24–25), 5474-5484.

55. Chen, J.; Lee, Y. M.; Davis, K. M.; Wu, X.; Seo, M. S.; Cho, K. B.; Yoon, H.; Park, Y. J.; Fukuzumi, S.; Pushkar, Y. N.; Nam, W., A mononuclear non-heme manganese(IV)-oxo complex binding redox-inactive metal ions. *J. Am. Chem. Soc.* **2013,** *135* (17), 6388-91.

56. Prakash, J.; Rohde, G. T.; Meier, K. K.; Jasniewski, A. J.; Van Heuvelen, K. M.; Münck, E.; Que, L., Spectroscopic Identification of an Fe(III) Center, not Fe(IV), in the Crystalline Sc–O–Fe Adduct Derived from [Fe(IV)(O)(TMC)](2+). *J. Am. Chem. Soc.* **2015,** *137* (10), 3478-3481.

57. Saltzman, H.; Sharefkin, J. G., Iodosobenzene. In *Org. Synth.*, John Wiley & Sons, Inc.: 2003.

58. Scarborough, C. C.; WIELICZKO, M., Catalysis in the production of phenols from aromatics. Google Patents: 2015.

59. Wallen, C. M.; Wielizcko, M.; Bacsa, J.; Scarborough, C. C., Heterotrimetallic sandwich complexes supported by sulfonamido ligands. *Inorganic Chemistry Frontiers* **2016,** *3* (1), 142-149.

60. Dolomanov, O. V.; Bourhis, L. J.; Gildea, R. J.; Howard, J. A. K.; Puschmann, H., OLEX2: a complete structure solution, refinement and analysis program. *J. Appl. Crystallogr.* **2009,** *42*, 339-341.

61. Sheldrick, G., SHELXT - Integrated space-group and crystal-structure determination. *Acta Crystallographica Section A* **2015,** *71* (1), 3-8.

62. Sheldrick, G., A short history of SHELX. *Acta Cryst. A* **2008,** *64*, 112-122.

63. Desai, L. V.; Malik, H. A.; Sanford, M. S., Oxone as an Inexpensive, Safe, and Environmentally Benign Oxidant for C−H Bond Oxygenation. *Org. Lett.* **2006,** *8* (6), 1141-1144.

64. Lacy, D. C.; Park, Y. J.; Ziller, J. W.; Yano, J.; Borovik, A. S., Assembly and Properties of Heterobimetallic CoII/III/CaII Complexes with Aquo and Hydroxo Ligands. *J. Am. Chem. Soc.* **2012,** *134* (Copyright (C) 2012 American Chemical Society (ACS). All Rights Reserved.), 17526-17535.

65. Van Heuvelen, K. M.; Fiedler, A. T.; Shan, X.; De Hont, R. F.; Meier, K. K.; Bominaar, E. L.; Münck, E.; Que, L., One-electron oxidation of an oxoiron(IV) complex to form an [O═FeV═NR]+ center. *Proc. Natl. Acad. Sci.* **2012,** *109* (30), 11933-11938.

66. Ferreira, K. N.; Iverson, T. M.; Maghlaoui, K.; Barber, J.; Iwata, S., Architecture of the Photosynthetic Oxygen-Evolving Center. *Science* **2004,** *303* (5665), 1831-1838.

67. Umena, Y.; Kawakami, K.; Shen, J.-R.; Kamiya, N., Crystal structure of oxygen-evolving photosystem II at a resolution of 1.9 Å. *Nature* **2011,** *473*, 55-60.

68. Lee, C.-Y.; Guo, S.-X.; Murphy, A. F.; McCormac, T.; Zhang, J.; Bond, A. M.; Zhu, G.; Hill, C. L.; Geletii, Y. V., Detailed Electrochemical Studies of the Tetraruthenium Polyoxometalate Water Oxidation Catalyst in Acidic Media: Identification of an Extended Oxidation Series using Fourier Transformed Alternating Current Voltammetry. *Inorg. Chem.* **2012,** *51* (21), 11521-11532.

69. Grigoriev, V. A.; Cheng, D.; Hill, C. L.; Weinstock, I. A., Role of Alkali Metal Cation Size in the Energy and Rate of Electron Transfer to Solvent-Separated 1:1 [(M+)(Acceptor)] (M^+) Li^+, Na^+, K^+) Ion Pairs. *J. Am. Chem. Soc.* **2001,** *123*, 5292-5307.

70. Li, J.; Bond, A. M.; Zhang, J., Probing Electrolyte Cation Effect on the Electron Transfer Kinetics of the [α-$SiW_{12}O_{40}$]4−/5− and [α-$SiW_{12}O_{40}$]5−/6− Processes using a Boron-Doped Diamond Electrode. *Electrochim. Acta* **2015**, Published online 14 August 2015.

71. Pope, M. T.; Müller, A., Polyoxometalate Chemistry: An Old Field with New Dimensions in Several Disciplines. *Angewandte Chemie International Edition in English* **1991,** *30* (1), 34-48.

72. (a) Boyd, T.; Mitchell, S. G.; Gabb, D.; Long, D.-L.; Cronin, L., Investigating Cation Binding in the Polyoxometalate-Super-Crown [P8W48O184]40−. *Chemistry – A European Journal* **2011,** *17* (43), 12010-12014; (b) Müller, A.; Sousa, F. L.; Merca, A.; Bögge, H.; Miró, P.; Fernández, J. A.; Poblet, J. M.; Bo, C., Supramolecular Chemistry on a Cluster Surface: Fixation/Complexation of Potassium and Ammonium Ions with Crown-Ether-Like Rings. *Angewandte Chemie* **2009,** *121* (32), 6048-6051.

73. Zhang, Z.-M.; Yao, S.; Li, Y.-G.; Han, X.-B.; Su, Z.-M.; Wang, Z.-S.; Wang, E.-B., Inorganic Crown Ethers: Sulfate-Based Preyssler Polyoxometalates. *Chemistry – A European Journal* **2012,** *18* (30), 9184-9188.

74. Swaddle, T. W., Homogeneous versus Heterogeneous Self-Exchange Electron Transfer Reactions of Metal Complexes: Insights from Pressure Effects. *Chem. Rev.* **2005,** *105*, 2573-2608.

75. Czap, A.; Neuman, N. I.; Swaddle, T. W., Electrochemistry and Homogeneous Self-Exchange Kinetics of the Aqueous 12-Tungstoaluminate(5−/6−) Couple. *Inorg. Chem.* **2006,** *45*, 9518-9530.

76. Dogonadze, R. R.; Ulstrup, J.; Kharkats, Y. I., A theory of electrode reactions through bridge transition states; bridges with a discrete electronic spectrum. *J.Electroanal. Chem. Interfacial Electrochem.* **1972,** *39* (1), 47-61.

77. (a) Natali, M.; Orlandi, M.; Berardi, S.; Campagna, S.; Bonchio, M.; Sartorel, A.; Scandola, F., Photoinduced Water Oxidation by a Tetraruthenium Polyoxometalate Catalyst: Ion-pairing and Primary Processes with $Ru(bpy)_3^{2+}$ Photosensitizer. *Inorg. Chem.* **2012,** *51*, 7324-7331; (b) Ballardini, R.; Gandolfi, M. T.; Balzani, V., Dynamic and static quenching of the luminescence of ruthenium(II) polypyridine complexes by heteropolytungstate anions. Direct measurements of intramolecular electron - transfer rate constants. *Inorg. Chem.* **1987,** *26* (6), 862-867; (c) Vickers, J. W.; Sumliner, J. M.; Lv, H.; Morris, M.; Geletii, Y. V.; Hill, C. L., Collecting meaningful early-time kinetic data in homogeneous catalytic water oxidation with a sacrificial oxidant. *Phys. Chem. Chem. Phys.* **2014,** *16* (24), 11942-11949.

78. Guo, S.-X.; Lee, C.-Y.; Zhang, J.; Bond, A. M.; Geletii, Y. V.; Hill, C. L., Mediator enhanced water oxidation using $Rb_4[Ru^{II}(bpy)_3]_5[\{Ru^{III}{}_4O_4(OH)_2(H_2O)_4\}(\gamma\text{-}SiW_{10}O_{36})_2]$ film modified electrodes. *Inorg. Chem.* **2014,** *53* (14), 7561-7570.

79. Liu, Y.; Guo, S.-X.; Bond, A. M.; Zhang, J.; Geletii, Y. V.; Hill, C. L., Voltammetric Determination of the Reversible Potentials for $[\{Ru_4O_4(OH)_2(H_2O)_4\}(\gamma\text{-}SiW_{10}O_{36})_2]^{10-}$ over the pH

Range of 2−12: Electrolyte Dependence and Implications for Water Oxidation Catalysis. *Inorg. Chem.* **2013,** *52* (20), 11986-11996.

80. Tézé, A.; Hervé, G., α-, β-, and γ-Dodecatungstosilicic Acids: Isomers and related Lacunary Compounds. In *Inorg. Synth.*, Ginsberg, A. P., Ed. John Wiley and Sons: New York, 1990; Vol. 27, pp 85-96.

81. Liu, Y. P.; Zhao, S. F.; Guo, S. X.; M., B. A.; Zhang, J.; Zhu, G.; Geletii, Y. V.; Hill, C. L., Electrooxidation of Ethanol and Methanol Using the Molecular Catalyst $[\{Ru_4O_4(OH)_2(H_2O)_4\}(\gamma\text{-}SiW_{10}O_{36})_2]^{10-}$. *J. Am. Chem. Soc* **2016,** *138* (8), 2617-2628.

82. Junk, P. C., Crown ethers as stabilising ligands for oxonium ions. *New J. Chem.* **2008,** *32* (5), 762-773.

83. Duan, Y.; Clemente-Juan, J. M.; Giménez-Saiz, C.; Coronado, E., Cobalt Clusters with Cubane-Type Topologies Based on Trivacant Polyoxometalate Ligands. *Inorg. Chem.* **2016,** *55* (2), 925-938.

84. Weakley, T. J. R.; Evans, H. T., Jr.; Showell, J. S.; Tourné, G. F.; Tourné, C. M., 18-Tungstotetracobalto(II)diphosphate and related Anions: a Novel Structural Class of Heteropolyanions. *J. Chem. Soc., Chem. Commun.* **1973,** *4*, 139-140.

85. (a) Balula, Maria S.; Gamelas, José A.; Carapuça, Helena M.; Cavaleiro, Ana M. V.; Schlindwein, W., Electrochemical Behaviour of First Row Transition Metal Substituted Polyoxotungstates: A Comparative Study in Acetonitrile. *Eur. J. Inorg. Chem.* **2004,** *2004* (3), 619-628; (b) Katsoulis, D. E.; Pope, M. T., New Chemistry for Heteropolyanions in Anhydrous Nonpolar Solvents. Coordinative Unsaturation of Surface Atoms. Polyanion Oxygen Carriers. *J. Am. Chem. Soc.* **1984,** *106* (9), 2737-2738.

86. Finke, R. G.; Droege, M. W.; Domaille, P. J., Trivacant Heteropolytungstate Derivatives. 3.[1] Rational Syntheses, Characterization, Two-Dimensional ^{183}W NMR, and properties of $P_2W_{18}M_4(H_2O)_2O_{68}^{10-}$ and $P_4W_{30}M_4(H_2O)_2O_{112}^{16-}$ (M=Co, Cu, Zn). *Inorg. Chem.* **1987,** *26* (23), 3886-3896.

87. Li, B.; Yan, Y.; Li, F.; Xu, L.; Bi, L.; Wu, L., Synthesis, crystal structure, and properties of two sandwich-type tungstovanadates. *Inorg. Chim. Acta* **2009,** (362), 2796-2801.

88. Wieliczko, M.; Geletii, Y. V.; Bacsa, J.; Musaev, D. G.; Hill, C. L., Effects of Competitive Active-Site Ligand Binding on Proton- and Electron-Transfer Properties of the [Co4(H2O)2(PW9O34)2]10− Polyoxometalate Water Oxidation Catalyst. *J. Cluster Sci.* **2017,** *28* (2), 839-852.

89. Sheldrick, G. M., Crystal structure refinement with SHELXL. *Acta Crystallographica. Section C, Structural Chemistry* **2015,** *71* (Pt 1), 3-8.

90. Müller, A.; Rehder, D.; Haupt, E. T. K.; Merca, A.; Bögge, H.; Schmidtmann, M.; Heinze-Brückner, G., Artificial Cells: Temperature-Dependent, Reversible Li+-Ion Uptake/Release Equilibrium at Metal Oxide Nanocontainer Pores. *Angew. Chem. Int. Ed.* **2004,** *43*, 4466-4470.

91. Schiwon, R.; Klingan, K.; Dau, H.; Limberg, C., Shining light on integrity of a tetracobalt-polyoxometalate water oxidation catalyst by X-ray spectroscopy before and after catalysis. *Chem. Commun.* **2014,** *50*, 100-102.

92. Goberna-Ferrón, S.; Soriano-López, J.; Galán-Mascarós, J. R.; Nyman, M., Solution Speciation and Stability of Cobalt-Polyoxometalate Water Oxidation Catalysts by X-ray Scattering. *Eur. J. Inorg. Chem.* **2015**, 2833-2840.